

# THÈSE DE DOCTORAT

Soutenue à AMU — Aix-Marseille Université  
le ... décembre 2024 par

**Raffael DÜLL**

**SIMULATING EDGE PLASMA TURBULENCE FOR ITER:**  
Improving the numerical resolution of a very anisotropic, poorly  
conditioned diffusion problem

**Discipline**

Sciences pour l'Ingénieur

**Spécialité**

Fusion magnétique

**École doctorale**

ED 353 SCIENCES POUR L'INGÉNIER:  
MECANIQUE, PHYSIQUE, MICRO ET NA-  
NOELECTRONIQUE

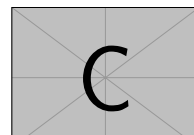
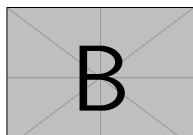
**Laboratoire/Partenaires de recherche**

Laboratoire de Mécanique, Modélisation &  
Procédés Propres (M2P2), AMU  
Institut de Recherche sur la Fusion par  
Confinement Magnétique (IRFM), CEA  
Cadarache

Consignes de présentation détaillées  
des pages liminaires en [annexe B](#)

**Composition du jury**

Prénom NOM	Rapporteur·e
Titre et affiliation	
Prénom NOM	Rapporteur·e
Titre et affiliation	
Prénom NOM	Examinateur·rice
Titre et affiliation	
Prénom NOM	Président·e du jury
Titre et affiliation	
Prénom NOM	Directeur·rice de thèse
Titre et affiliation	
Prénom NOM	Membre invité·e
Titre et affiliation	



# Affidavit

Je soussigné-e, [Prénom Nom], déclare par la présente que le travail présenté dans ce manuscrit est mon propre travail, réalisé sous la direction scientifique de [Prénom Nom], dans le respect des principes d'honnêteté, d'intégrité et de responsabilité inhérents à la mission de recherche. Les travaux de recherche et la rédaction de ce manuscrit ont été réalisés dans le respect à la fois de la charte nationale de déontologie des métiers de la recherche et de la charte AMU relative à la lutte contre le plagiat.

Ce travail n'a pas été précédemment soumis en France ou à l'étranger dans une version identique ou similaire à un organisme examinateur.

Fait à [ville] le [date]



Cette œuvre est mise à disposition selon les termes de la [Licence Creative Commons Attribution - Pas d'Utilisation Commerciale - Pas de Modification 4.0 International](#).

# **Liste de publications et participation aux conférences**

**Liste des publications et/ou brevets réalisées dans le cadre du projet de thèse:**

- 1.
- 2.
- 3.

**Participation aux conférences et écoles d'été au cours de la période de thèse:**

1. PlasmaSurf Summer School, Lisbon Portugal
2. EPS, July 2023, Bordeaux France
3. PET-19, September 2023, Hefei China
4. PSI-26, May 2024, Marseille France
5. ECCOMAS, June 2024, Lisbon Portugal

# Résumé et mots clés

Lorem ipsum dolor sit amet, consectetuer adipiscing elit. Ut purus elit, vestibulum ut, placerat ac, adipiscing vitae, felis. Curabitur dictum gravida mauris. Nam arcu libero, nonummy eget, consectetuer id, vulputate a, magna. Donec vehicula augue eu neque. Pellentesque habitant morbi tristique senectus et netus et malesuada fames ac turpis egestas. Mauris ut leo. Cras viverra metus rhoncus sem. Nulla et lectus vestibulum urna fringilla ultrices. Phasellus eu tellus sit amet tortor gravida placerat. Integer sapien est, iaculis in, pretium quis, viverra ac, nunc. Praesent eget sem vel leo ultrices bibendum. Aenean faucibus. Morbi dolor nulla, malesuada eu, pulvinar at, mollis ac, nulla. Curabitur auctor semper nulla. Donec varius orci eget risus. Duis nibh mi, congue eu, accumsan eleifend, sagittis quis, diam. Duis eget orci sit amet orci dignissim rutrum.

Mots clés: géométrie algorithmique, complexe planaire et rectangulaire, géodésique, courbure globale non-positive

# **Abstract and keywords**

Lorem ipsum dolor sit amet, consectetuer adipiscing elit. Ut purus elit, vestibulum ut, placerat ac, adipiscing vitae, felis. Curabitur dictum gravida mauris. Nam arcu libero, nonummy eget, consectetuer id, vulputate a, magna. Donec vehicula augue eu neque. Pellentesque habitant morbi tristique senectus et netus et malesuada fames ac turpis egestas. Mauris ut leo. Cras viverra metus rhoncus sem. Nulla et lectus vestibulum urna fringilla ultrices. Phasellus eu tellus sit amet tortor gravida placerat. Integer sapien est, iaculis in, pretium quis, viverra ac, nunc. Praesent eget sem vel leo ultrices bibendum. Aenean faucibus. Morbi dolor nulla, malesuada eu, pulvinar at, mollis ac, nulla. Curabitur auctor semper nulla. Donec varius orci eget risus. Duis nibh mi, congue eu, accumsan eleifend, sagittis quis, diam. Duis eget orci sit amet orci dignissim rutrum.

Keywords: computational geometry, planar and rectangular complex, geodesic, global nonpositive curvature

# Remerciements

Le modèle de thèse AMU n'existerait pas sans la contribution des doctorants. Nous souhaitons remercier tout particulièrement [Mickaël Bojados](#), [Flora Cordoleani](#) et [Florian Caullery](#) pour leur aide précieuse et la qualité de leurs fichiers sources LaTeX. La mise à jour effectuée en 2018 doit beaucoup à l'excellent travail de [Dorian Depriester](#).

Lorem ipsum dolor sit amet, consectetur adipiscing elit. Ut purus elit, vestibulum ut, placerat ac, adipiscing vitae, felis. Curabitur dictum gravida mauris. Nam arcu libero, nonummy eget, consectetur id, vulputate a, magna. Donec vehicula augue eu neque. Pellentesque habitant morbi tristique senectus et netus et malesuada fames ac turpis egestas. Mauris ut leo. Cras viverra metus rhoncus sem. Nulla et lectus vestibulum urna fringilla ultrices. Phasellus eu tellus sit amet tortor gravida placerat. Integer sapien est, iaculis in, pretium quis, viverra ac, nunc. Praesent eget sem vel leo ultrices bibendum. Aenean faucibus. Morbi dolor nulla, malesuada eu, pulvinar at, mollis ac, nulla. Curabitur auctor semper nulla. Donec varius orci eget risus. Duis nibh mi, congue eu, accumsan eleifend, sagittis quis, diam. Duis eget orci sit amet orci dignissim rutrum.

Nam dui ligula, fringilla a, euismod sodales, sollicitudin vel, wisi. Morbi auctor lorem non justo. Nam lacus libero, pretium at, lobortis vitae, ultricies et, tellus. Donec aliquet, tortor sed accumsan bibendum, erat ligula aliquet magna, vitae ornare odio metus a mi. Morbi ac orci et nisl hendrerit mollis. Suspendisse ut massa. Cras nec ante. Pellentesque a nulla. Cum sociis natoque penatibus et magnis dis parturient montes, nascetur ridiculus mus. Aliquam tincidunt urna. Nulla ullamcorper vestibulum turpis. Pellentesque cursus luctus mauris.

# Contents

<b>Affidavit</b>	<b>2</b>
<b>Liste de publications et participation aux conférences</b>	<b>3</b>
<b>Résumé et mots clés</b>	<b>4</b>
<b>Abstract and keywords</b>	<b>5</b>
<b>Remerciements</b>	<b>6</b>
<b>Contents</b>	<b>7</b>
<b>List of Figures</b>	<b>11</b>
<b>List of Tables</b>	<b>14</b>
<b>I. Introduction</b>	<b>15</b>
<b>II. Fundamental Concepts of Fluid Models for Magnetized Plasmas</b>	<b>18</b>
<b>1. Tokamak Concept</b>	<b>19</b>
1.1. Particles in a magnetized plasma . . . . .	19
1.1.1. Magnetic confinement . . . . .	19
1.1.2. Tokamak configuration . . . . .	20
1.1.3. Grad-Shafranov equilibrium . . . . .	21
1.1.4. Realisation of magnetic configurations . . . . .	23
1.2. Interaction between particles . . . . .	26
1.2.1. Debye shielding . . . . .	26
1.2.2. Particle collisions . . . . .	26
1.3. Scrape-Off-Layer . . . . .	29
1.3.1. Fundamental sheath physics . . . . .	29
1.3.2. Confinement characteristics . . . . .	30
1.3.3. Problematic of heat exhaust . . . . .	31

<b>2. Description of Plasmas</b>	<b>32</b>
2.1. Direct description of Plasma Particles . . . . .	32
2.1.1. Particle Tracking . . . . .	32
2.1.2. Kinetic Models . . . . .	33
2.2. Three Fluid Moments of the Kinetic Equation . . . . .	33
2.2.1. Mass Balance ( $k = 0$ ) . . . . .	34
2.2.2. Momentum Balance ( $k = 1$ ) . . . . .	35
2.2.3. Energy Balance ( $k = 2$ ) . . . . .	35
2.3. MHD description of plasmas . . . . .	36
2.3.1. Extended MHD Model . . . . .	36
2.3.2. Reduced MHD model . . . . .	37
2.4. Fluid closures . . . . .	38
2.4.1. Spizer-Härm model . . . . .	38
2.4.2. Braginskii and Zhdanov closures . . . . .	38
2.4.3. Reduced Ohm's law . . . . .	38
<b>3. Drift-reduced models for plasma turbulence</b>	<b>39</b>
3.1. Drift wave turbulence . . . . .	40
3.1.1. Plasma drifts . . . . .	40
3.1.2. Drift-ordering approximation . . . . .	41
3.1.3. Linear plasma instabilities . . . . .	43
3.2. Electromagnetic effects in edge plasma . . . . .	46
3.2.1. Magnetic induction . . . . .	46
3.2.2. Electron inertia . . . . .	47
3.2.3. Electromagnetic flutter . . . . .	47
3.3. Drift-Alfvén waves . . . . .	48
3.3.1. Linear analysis . . . . .	48
3.3.2. Non-linear effects . . . . .	48
<b>III. An Electromagnetic Model for SOLEDGE3X</b>	<b>49</b>
<b>4. Electromagnetic effects coupled to the SOLEDGE3X framework</b>	<b>50</b>
4.1. Transport equations . . . . .	50
4.1.1. Mass balance . . . . .	50
4.1.2. Momentum balance . . . . .	50
4.1.3. Charge balance . . . . .	52
4.2. Electromagnetic Model in SOLEDGE3X . . . . .	54
4.2.1. Electron Inertia . . . . .	54
4.2.2. Electromagnetic Induction . . . . .	56
4.2.3. Electromagnetic Flutter . . . . .	57
4.3. Boundary conditions . . . . .	58
4.4. Dimensionless fields . . . . .	59

4.5. Expressing the electromagnetic vorticity equation in matrix form . . . . .	61
4.5.1. Vorticity system with electron inertia . . . . .	61
4.5.2. Electromagnetic vorticity system . . . . .	62
4.5.3. Dimensionless electromagnetic vorticity system with electron inertia . . . . .	62
<b>5. Numerical Implementation</b>	<b>64</b>
5.1. Geometrical consideration . . . . .	64
5.1.1. Domain decomposition and mesh design . . . . .	64
5.1.2. Curvilinear coordinates . . . . .	65
5.1.3. Finite volume approach . . . . .	68
5.2. The staggered mesh . . . . .	68
5.2.1. Description and notation of the staggered grid . . . . .	69
5.2.2. Boundary cells . . . . .	70
5.2.3. Staggered discrete operators . . . . .	71
5.2.4. Discretization around the X-point . . . . .	74
5.3. Time discretization . . . . .	74
5.3.1. Explicit Runge-Kutta solver . . . . .	75
5.3.2. Implicit-explicit VSIMEX solver . . . . .	75
5.4. Initialization at Restart . . . . .	75
5.4.1. Electron Inertia . . . . .	75
5.4.2. Parallel Magnetic Vector Potential . . . . .	75
5.5. Implicit Numerical Treatment . . . . .	75
5.5.1. Parallel diffusion operator with flutter . . . . .	75
5.5.2. Electromagnetic vorticity system . . . . .	76
<b>6. Verification and Validation</b>	<b>80</b>
6.1. Verification by the Method of manufactured solutions . . . . .	80
6.1.1. Test system . . . . .	80
6.1.2. Analytic solution . . . . .	82
6.1.3. Order of convergence . . . . .	82
6.2. Linear Analysis . . . . .	83
6.2.1. Pure advection . . . . .	83
6.2.2. Electrostatic case . . . . .	85
6.2.3. Electromagnetic case . . . . .	86
<b>IV. Impact of Electromagnetic Effects on Plasma Simulations</b>	<b>92</b>
<b>7. Electromagnetic simulations on analytic geometries</b>	<b>93</b>
7.1. Slab configurations . . . . .	93
7.1.1. Analysis of a plasma blob . . . . .	93
7.1.2. Generation of drift waves . . . . .	94
7.2. Circular geometry . . . . .	96

<b>8. Electromagnetic simulations on a realistic diverted geometry</b>	<b>97</b>
8.1. Simulation set-up . . . . .	97
8.2. Comparison between the scenarios . . . . .	99
8.3. Numerical performances . . . . .	100
<b>V. Further Applications: Ripple Simulations</b>	<b>103</b>
<b>9. Simulations of Magnetic ripple</b>	<b>104</b>
9.1. Motivation for simulating magnetic ripple . . . . .	104
9.2. Generation of a non-axisymmetric magnetic configuration . . . . .	105
9.3. Application to a WEST scenario . . . . .	109
9.4. Conclusion . . . . .	110
<b>Conclusion</b>	<b>112</b>
<b>Bibliography</b>	<b>113</b>
<b>Index</b>	<b>120</b>
<b>APPENDICES</b>	<b>121</b>
<b>A. New software modules</b>	<b>122</b>
A.1. Grad-Shafranov solver . . . . .	122
A.2. Poincaré plots . . . . .	122
A.3. Generation of a modulated magnetic configuration . . . . .	122
A.4. Toroidal plots in pySOLEDGE3X . . . . .	122
<b>B. Intitulés des doctorats AMU</b>	<b>123</b>
<b>C. Consignes de présentation</b>	<b>128</b>
<b>D. Presentation guidelines</b>	<b>130</b>

# List of Figures

1.	Fusion reaction cross-sections for the most promising pairs of light elements over plasma temperature. . . . .	16
1.1.	Trajectory of a positively and a negatively charged particle along a homogeneous magnetic field line. . . . .	20
1.2.	Simplified scheme of the magnetic field components on a flux surface (a) and the total magnetic field (b). . . . .	21
1.3.	Solution of the Grad-Shafranov equation on a circular cross-section with minor radius $a = 0.3$ m. A Cartesian mesh with $N = 200$ equidistant discretization points is used for the $R$ and $Z$ coordinates. The flux $\Psi$ is forced to 0 at the boundary. The toroidal magnetic field is given by $B_\varphi = B_0 R_0 / R$ with $B_0 = 1$ T. The pressure follows an exponential distribution $p(\Psi) = p_0(e^{-\Psi} - 1)$ with $p_0 = 1$ MPa. . . . .	23
1.4.	Cutaway of the ITER tokamak (source: ITER Organization) . . . . .	24
1.5.	Comparison of the limited and diverted configuration on a WEST geometry. . . . .	25
1.6.	Trajectory of the projectile particle (red) colliding with the target particle (green). The vector $\mathbf{b}$ denotes the impact factor and $\chi$ is the deflection angle caused by the collision. . . . .	27
1.7.	Volume for given $db$ and $dx$ in which collisions on the projectile are considered. . . . .	28
5.1.	Example of typical mesh and domain decomposition mapping the real domain (a) to a Cartesian multiple zones domain (b). Each colored zone is isomorphic to a cube, the lines connecting the edges indicate the neighbours mapping. . . . .	64
5.2.	General view of the staggered grid points marked as crosses on top of the collocated cells. The red cross at the position $[i_\psi, i_\theta - \frac{1}{2}, i_\varphi - \frac{1}{2}]$ corresponds to the central cell with index $[i_\psi, i_\theta, i_\varphi]$ . . . . .	69
5.3.	General view of the staggered grid points in the $\theta - \varphi$ plane that are solved in the vorticity equation. Note that at the lower boundaries, collocated fields are included in the system but not their staggered counterparts. . . . .	70
5.4.	Depiction of the relevant cell faces to calculate fluxes of a staggered field at coordinate index $[i_\psi, i_\theta - \frac{1}{2}, i_\varphi - \frac{1}{2}]$ . . . . .	73

5.5. Sketches of the mesh around the X-point. For centered cells (a), 8 cells touch the X-point at a corner. For staggered cells (b), the X-point is located at the radial face of 4 cells, effectively modifying the shape of the cells to pentagons. Fluxes across the involved faces are hence ill-defined.	74
5.6. Sketches showing the calculation of gradients for the parallel diffusion scheme. It shows the position where the different gradients are calculated that are relevant for a flux across the cell face with a solid line. Green and red arrows symbolize gradients in the equilibrium and in the radial direction, respectively. . . . .	76
6.1. Distorted MMS mesh geometry with $N = 20$ cells per dimension on a 3rd of a torus . . . . .	80
6.2. Relative error between the initial plasma and the solution after one timestep. The $x$ -axis indicates the number of points per zone in each direction, the total number of points is thus $N_{tot}^{3D} = 8 \cdot X^3$ (resp. $N_{tot}^{2D} = 4 \cdot X^2$ ). The dashed lines indicate the slope of the ideal 2nd order convergence . . . . .	83
6.3. Evolution of the 1D SLAB system with 64 cells in poloidal direction over 10000 timesteps with the RK4 scheme. For a better readability only parts of the graphs are represented . . . . .	85
6.4. Evolution of the 2D electrostatic SLAB system with 64 cells in radial and poloidal direction over 10000 timesteps with the implicit Euler scheme. The system is grounded at the center of the domain to $\Phi^G = 0V$ . . . . .	86
6.5. Snapshot of an electromagnetic SLAB simulation on a domain with $N_\psi = 32$ and $N_\theta = 64$ grid points. All point at the radial center with $i_\psi^G$ are grounded. . . . .	89
6.6. Relative error for the fits of the frequency $\omega_0$ and the decay rate $\lambda$ on the evolution of $A_\parallel$ with respect to the expected values in a grounded electromagnetic SLAB simulation on a domain with $N_\psi = 32$ and $N_\theta = 64$ grid points. . . . .	90
7.1. Density profiles [part/m <sup>3</sup> ] after 9.6 $\mu$ s simulated plasma time for the electrostatic (ES), magnetic inductive (EM) and full electromagnetic scenarios (EM-flutter). The first row shows a view of the $R - \varphi$ plane with the maximum density taken along the $Z$ coordinate. The second and third rows show the density on poloidal planes ( $R - Z$ ) at the center of the field lines (1) and in proximity to the sheath (2). . . . .	94
7.2. Density profiles [part/m <sup>3</sup> ] at the toroidal center of the slab, at about 32m from both limiters. The snapshots compare the electrostatic (ES), magnetic inductive (EM) and full electromagnetic scenarios (EM-flutter) scenarios after 8, 16 and 24 $\mu$ s simulated plasma time. . . . .	96

8.1. Simulation snapshots of the full electromagnetic scenario with flutter. The first poloidal plane is shown after 6 ms simulated plasma time on the TCV case. From left to right, the first row shows the ion density $n_i$ , the electron temperature $T_e$ , the electric potential $\Phi$ , and the radial "ExB" drift velocity $v_E^\psi$ . The second row shows the parallel magnetic potential $A_\parallel$ , the parallel current density $j_\parallel$ , the amplitude of the flutter field $\ \tilde{\mathbf{B}}\ $ , and the radial flutter advection velocity $v_{\tilde{b}\psi}$ . . . . .	98
8.2. Evolution of the kinetic energy and heat exhaust over time iterations on the turbulent TCV scenario. It indicates the turbulence level and its consequence on the total heat transport. . . . .	100
8.3. Radial profiles at the outer mid-plane after 6 ms simulated plasma time. These profiles were obtained by averaging simulation data across all 32 toroidal planes and over the last 20 available plasma saves. . . . .	100
9.1. Infrared camera view of the divertor target, taken from [3]. Red zones correspond to hot regions with high heat deposition. One can see the "snake skin" pattern, where the maximal intensity alternates between the inner and outer strike points. . . . .	105
9.2. Exemplary SOLEDGE3X mesh for a WEST single-null geometry . . . . .	106
9.3. Top views of the perturbated field $\mathbf{B}_{pert}$ on the WEST tokamak at the mid plane. The black dots indicate the position of the toroidal field coils. The amplitude of the perturbated field remains much smaller than the axisymmetric component, whose amplitude ranges around 1T. . . . .	107
9.4. Map of the poloidal field $B_{pol}$ [T] at several poloidal planes within a rip- ple peridod around the lower X-point and the divertor targets. Stream- lines are supperposed to the fields to better visualize the position of the X-point and the separatrix at the divertor. The phase shifts 0 and 1/2 with respect to the coil positions are identical to the axisymmetric con- figuration as $B_{pert}^\psi$ vanishes while the planes at 1/4 and 3/4 correspond to the respective maximum and minimum of $B_{pert}^\psi$ . . . . .	108
9.5. Poincaré plot at coil-aligned poloidal planes. Seed points are uniformly distributed on the mid-plane along the radial and toroidal directions. Because of the periodicity of the perturbated field, each point corre- sponds to a field line crossing any of the $N_c$ planes aligned with a coil. The total length of a field line from wall to wall translates in its color, black standing for an infinite closed field line. . . . .	109
9.6. Calculated electron wall heat flux in the divertor region from the SOLEDGE3X simulation. View on the target from the top for one ripple period. . . . .	110

# List of Tables

8.1. Numerical metrics on the four TCV scenarios for one timestep. All quantities are averaged over the last 20000 timesteps of the simulation. The execution time refers to the wall-clock time and must be multiplied by the number of used processors (768) to get the actual used CPU time. .	101
9.1. Technical parameters of the toroidal field coils used to generate the ripple field for the WEST tokamak . . . . .	107

# **Part I.**

## **Introduction**

The sun is the primary source of energy for Earth, essential for photosynthesis in plants, which forms the basis of most food chains, and for driving the weather and climate systems that shape our environment. Its consistent radiation supports all life forms, regulates global temperatures, and influences fundamental ecological and biological processes that are vital for the Earth's diverse ecosystems. From the very outset of human life, the sun has been a subject of profound admiration, occupying a central role in various religious beliefs and was often synonym of an incomparably vast and potent source of energy. It was not until the beginning of the twentieth century that progress in particle physics allowed to unravel the secret of solar energy: nuclear fusion. It is the physical process where two light atomic nuclei merge to form a heavier nucleus, releasing significant energy as a result of mass-to-energy conversion. The dream of achieving nuclear fusion in a laboratory to produce energy emerged shortly thereafter. In today's climate crisis, nuclear fusion is even more appealing because it does not emit carbon emissions, does not present the risk of a catastrophic meltdown and its fuel, hydrogen, is readily available. Since replicating the sun's core conditions on Earth, particularly the immense pressure, is not feasible, alternative approaches were searched. A look at the reaction cross-section of various pairs of light atoms shows that deuterium-tritium (D-T) fusion has the highest likelihood at the lowest temperature. These two hydrogen isotopes are hence the most favorable candidates for fusion; deuterium is naturally abundant, but tritium, which is radioactive and has a relatively short half-life, must be artificially produced.

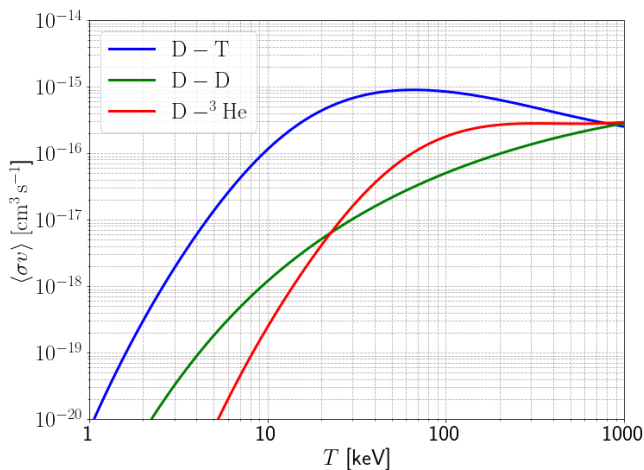


Figure 1.: Fusion reaction cross-sections for the most promising pairs of light elements over plasma temperature.

At such elevated temperatures, the binding energy is insufficient to maintain the cohesion of electrons and atomic nuclei, resulting in the formation of a state of matter known as plasma. Fundamentally, plasma is an ionized gas composed of positively charged nuclei and negatively charged electrons, which interact electromagnetically.

Lawson's criterion[37] estimates the necessary plasma conditions to reach the break-even point, when fusion power exceeds heating and conduction losses. For D-T fusion, the triple product of density  $n$ , temperature  $T$  and confinement time  $\tau_E$  must exceed:

$$n T \tau_E > 10^{-21} \text{ keV m}^{-3} \text{s} \quad (0.1)$$

The reaction cross-section determines an optimal temperature of approximately 15-40 keV ( 150 millions °C) for fusion reactions, leading fusion reactor designs to focus on maximizing either of the two remaining parameters: density or confinement time. Inertial Confinement Fusion (ICF) seeks to compress dense fuel pellets for an extremely brief duration using high-powered lasers. Conversely, Magnetic Confinement Fusion (MCF) utilizes strong magnetic fields to sustain stable plasmas at relatively low densities. Both approaches have conducted promising experiments close to the break-even point. Within MCF there are two primary designs: tokamaks, which use a toroidal chamber with an axisymmetric magnetic field, and stellarators, which use a twisted magnetic configuration to improve plasma confinement.

For MCF Plasma heating - Ohmic heating - ICRH, ECRH, NBI  
fusion gain Q as essential metric.

show diagram with all machines, scaling laws for fusion performance

The largest fusion experiment ITER, employing tokamak technology, is currently under construction in southern France by an international collaboration of seven member parties. At its full operation it is expected to achieve ignition, a state where the fusion reaction emits sufficiently radiation to maintain the plasma conditions. It requires a heat exhausts ten times higher than the break-even point and is a critical milestone for the development of future commercial fusion reactors.

Introduce necessity for (electromagnetic) turbulent simulations (estimate cross-field transport, power exhaust, ELMs...)

## **Part II.**

# **Fundamental Concepts of Fluid Models for Magnetized Plasmas**

# 1. Tokamak Concept

Fusion reactions require extreme temperatures at about 15keV to happen. At such high temperatures, any matter transforms into an ionized state, called plasma, where electrons are dissociated from their atomic core. Charged particles are particularly responsive to magnetic fields, a property that will be used by tokamaks to confine the hot plasma and protect the physical walls of the device.

A deuterium plasma is an ionized gas comprising positively charged ions ( $D^+$ ) and negatively charged electrons ( $e^-$ ). Initially, both species exhibit independent dynamics. Despite having exactly opposite charges, ions are significantly heavier than electrons, with a mass ratio of  $m_i/m_e \approx 3.7 \cdot 10^3$ . Both ions and electrons can be described by their respective momenta and temperatures. In Sec. 1.1, we first describe their independent behavior in a magnetized environment, then how species interact in Sec. 1.2 and we finish with Sec. 1.3 about the importance of the Scrape-Off-Layer.

## 1.1. Particles in a magnetized plasma

This first section is dedicated to elucidate the fundamental working principle of tokamaks. Before all, we must understand how charged particles behave when exposed to strong magnetic fields (in Sec. 1.1.1) and how this knowledge allows us to design a magnetic "cage", in which particles are trapped, or confined (in Sec. 1.1.2). The governing equations of this magnetic configuration are given in Sec. 1.1.3 and Sec. 1.1.4 introduces and compares limited and diverted configurations.

### 1.1.1. Magnetic confinement

To understand how charged plasma particles can be confined on a magnetic field line, we consider the simplest example of a single particle with charge  $q$  in a homogeneous, unidirectional magnetic field  $\mathbf{B}$  with directional unit vector  $\mathbf{b}$ . The amplitude of the magnetic field is then  $B$  such that  $\mathbf{B} = B\mathbf{b}$ . Solely the magnetic component of Lorentz's force acts on a particle with mass  $m$  and charge  $q$ , leading to the following equation for its velocity  $\mathbf{v}$ :

$$m \frac{d\mathbf{v}}{dt} = q\mathbf{v} \times \mathbf{B} \quad (1.1)$$

To solve this differential equation, it is convenient to decompose the velocity vector into a parallel component  $v_{\parallel} = \mathbf{v} \cdot \mathbf{b}$  and a perpendicular component  $\mathbf{v}_{\perp} = \mathbf{v} - v_{\parallel}\mathbf{b}$ . For a given initial velocity  $\mathbf{v}_0$ , the general solution of this system is:

$$\mathbf{v}(t) = v_{\parallel,0} \mathbf{b} + \mathbf{v}_{\perp,0} \cos(\omega_B t) + \mathbf{b} \times \mathbf{v}_{\perp,0} \sin(\omega_B t) \quad (1.2)$$

with  $\omega_B = \frac{qB}{m}$  being the cyclotron frequency. This implies that a charged particle circles around a magnetic field line while following it with its initial velocity. The opposite charges of ions and electrons result in them circling in different directions. The trajectory is qualitatively shown in Fig. 1.1. The radius of this gyromotion is called the Larmor radius  $\rho_L$ :

$$\rho_L = \frac{m \|\mathbf{v}_{\perp,0}\|}{qB} \quad (1.3)$$

Because of the high mass ratio, ions have a much larger Larmor radius than electrons. This gyromotion is the fundamental mechanism behind magnetic confinement.

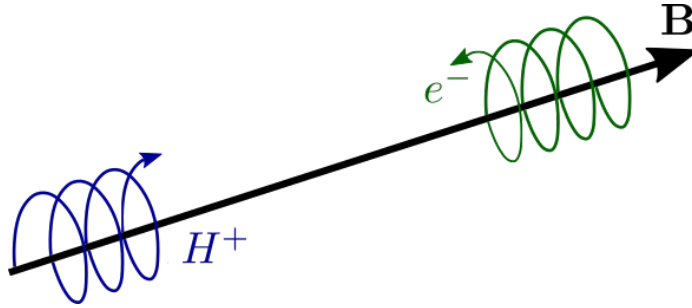


Figure 1.1.: Trajectory of a positively and a negatively charged particle along a homogeneous magnetic field line.

For a non-homogeneous field, Eq. 1.1 does not necessarily have a straightforward solution. To assume gyromotion as the fundamental dynamic for particles, the magnetic field must remain relatively constant along the helical path traced by the field lines. This requirement imposes a criterion on the Larmor radius, known as adiabatic theory:

$$\rho_L \ll \frac{B}{\|\nabla B\|} \quad (1.4)$$

### 1.1.2. Tokamak configuration

Maxwell's law stipulates that the magnetic field must be divergence-free,  $\nabla \cdot \mathbf{B} = 0$ . Since constructing an infinitely long machine is impractical, particle confinement requires that a given field line be closed, meaning that following its path would return one to the initial position. This necessitates some bending of the magnetic field lines. The fundamental principle of a tokamak lies in its magnetic configuration, which is designed to confine hot plasma within a toroidal chamber. This configuration comprises two primary magnetic field components: the toroidal field  $B_\phi$  and the poloidal field  $B_p$ . Coils encircling the torus generate the toroidal field, which runs

## 1. Tokamak Concept – 1.1. Particles in a magnetized plasma

parallel to the circular path of the tokamak and serves to confine the plasma. A strong current passing through the plasma itself induces the poloidal field. The combination of these fields creates a twisted, helical magnetic field structure, as shown in Fig. 1.2, that stabilizes the plasma and helps maintain its shape and position within the tokamak.

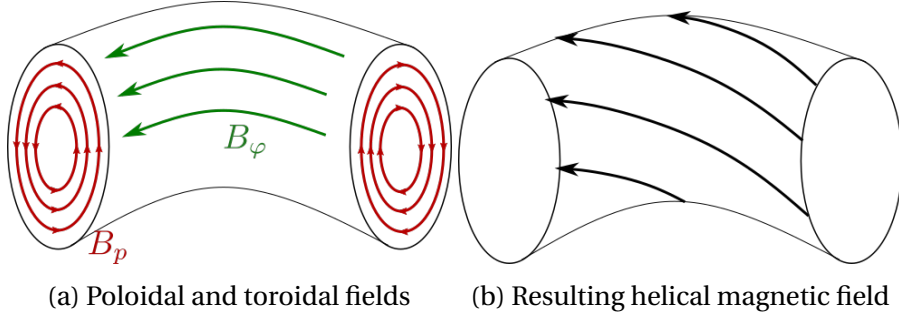


Figure 1.2.: Simplified scheme of the magnetic field components on a flux surface (a) and the total magnetic field (b).

The helical configuration of a magnetic field line in a tokamak ensures that tracing its path remains within the same toroidal surface, ultimately returning to the initial point and forming a closed field line. The ensemble of all such field lines constitutes what is termed a "closed magnetic flux surface." These flux surfaces are radially concentric, and the principle of magnetic confinement is to trap plasma particles within these flux surfaces.

At first glance, the toroidal field appears sufficient to close magnetic field lines. However, internal and external perturbations can cause twisting of the magnetic field lines, potentially leading to disruptions and total loss of plasma confinement. This phenomenon is known as kink instabilities. To suppress them, the poloidal field introduces magnetic shear to the configuration, with field lines circling around the minor radius of the torus. The ratio of toroidal to poloidal rotations of the field lines is known as the safety factor  $q = \frac{aB_\varphi}{RB_p}$ . In a cylindrical approximation, the Kruskal-Shafranov limit [36, 57] states that kink instabilities are suppressed for  $q > 1$ . However, the safety factor cannot be too large either, as other instabilities such as tearing [20] or resistive wall [19] modes might appear and deteriorate plasma confinement.

### 1.1.3. Grad-Shafranov equilibrium

How can the magnetic configuration be described in a more mathematical way? The magnetic configuration of a tokamak can be described mathematically in cylindrical coordinates  $(R, Z, \varphi)$  with the corresponding basis vectors  $[\mathbf{e}_R, \mathbf{e}_Z, \mathbf{e}_\varphi]$ . The magnetic field consists of two main components: the poloidal field  $\mathbf{B}_p$ , which lies in the  $(R, Z)$

## 1. Tokamak Concept – 1.1. Particles in a magnetized plasma

plane (referred to as the "poloidal plane"), and the toroidal field  $\mathbf{B}_\varphi$ , which is aligned along the  $\varphi$ -direction.

Each magnetic field  $\mathbf{B}$  is associated with a vector potential  $\mathbf{A}$  such that:

$$\nabla \times \mathbf{A} = \mathbf{B} \quad (1.5)$$

Assuming axisymmetry, gradients along the  $\varphi$ -direction vanish. Let  $\mathbf{A} = A_R \mathbf{e}_R + A_Z \mathbf{e}_Z + A_\varphi \mathbf{e}_\varphi$  represent the components of the vector potential. The magnetic field can then be expressed as:

$$\mathbf{B} = \left( \frac{1}{R} \frac{\partial(RA_\varphi)}{\partial Z} \right) \mathbf{e}_R - \left( \frac{1}{R} \frac{\partial(RA_\varphi)}{\partial R} \right) \mathbf{e}_Z + \left( \frac{\partial A_Z}{\partial R} - \frac{\partial A_R}{\partial Z} \right) \mathbf{e}_\varphi \quad (1.6)$$

Introducing the poloidal flux function  $\Psi = -RA_\varphi$ , which shapes  $\mathbf{B}_p$ , and the toroidal field function  $F = RB_\varphi$ , the magnetic field components can be written as:

$$\mathbf{B} = \underbrace{\nabla\Psi \times \nabla\varphi}_{\mathbf{B}_p} + \underbrace{F\nabla\varphi}_{\mathbf{B}_\varphi} \quad (1.7)$$

In a tokamak, the plasma is not uniform, leading to a pressure gradient from the colder edge to the hotter core. In a stationary plasma that has reached magnetohydrodynamic (MHD) equilibrium, the magnetic and pressure forces must balance, which is described by the force balance equation:

$$\nabla p = \mathbf{j} \times \mathbf{B} \quad (1.8)$$

Because of the cross-product,  $\nabla p$  is always perpendicular to  $\mathbf{B}$ , implying that  $p$  must be constant along a field line. Under the assumption of axisymmetry,  $\partial_\varphi p = 0$ , meaning that the toroidal component of the magnetic force must be zero. Consequently, only the poloidal field  $\mathbf{B}_p$  responds to a pressure gradient. Since the pressure  $p(\Psi)$  is both axisymmetric and field-aligned, it can only be a function of the poloidal flux  $\Psi$ . The toroidal component of the current density can be expressed as:

$$j_\varphi = R \frac{dp}{d\Psi} + \frac{F}{\mu_0 R} \frac{dF}{d\Psi} \quad (1.9)$$

Ampère's law relates the current density  $\mathbf{j}$  to the magnetic field  $\mathbf{B}$ , with the vacuum permeability  $\mu_0$ :

$$\mu_0 \mathbf{j} = \nabla \times \mathbf{B} \quad (1.10)$$

This gives an alternative expression for the toroidal current:

$$j_\varphi = \frac{1}{\mu_0} \left[ \partial_R \left( \frac{1}{R} \partial_R \Psi \right) + \frac{1}{R} \partial_Z^2 \Psi \right] \quad (1.11)$$

By equating both expressions for  $j_\varphi$ , we arrive at the Grad-Shafranov equation [22, 58] for the poloidal flux:

## 1. Tokamak Concept – 1.1. Particles in a magnetized plasma

$$\Delta^* \Psi = R \partial_R \left( \frac{1}{R} \partial_R \Psi \right) + \partial_Z^2 \Psi = -\mu_0 R^2 \frac{dp}{d\Psi} - \mu_0 F \frac{dF}{d\Psi} \quad (1.12)$$

Here we introduced the Shafranov operator  $\Delta^*$ . This equation is a second-order non-linear partial differential equation. The procedure outlined in Appendix A.1 solves Eq. 1.12 iteratively using a Newton-Krylov method. A typical solution for  $\Psi$  is illustrated in Fig. 1.3.

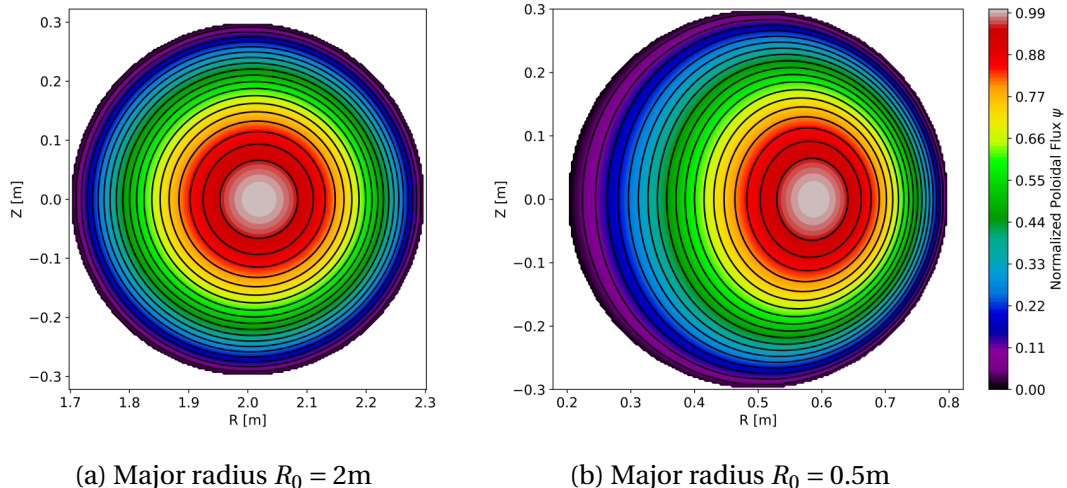


Figure 1.3.: Solution of the Grad-Shafranov equation on a circular cross-section with minor radius  $a = 0.3$  m. A Cartesian mesh with  $N = 200$  equidistant discretization points is used for the  $R$  and  $Z$  coordinates. The flux  $\Psi$  is forced to 0 at the boundary. The toroidal magnetic field is given by  $B_\varphi = B_0 R_0 / R$  with  $B_0 = 1\text{T}$ . The pressure follows an exponential distribution  $p(\Psi) = p_0(e^{-\Psi} - 1)$  with  $p_0 = 1\text{ MPa}$ .

The plasma pressure causes the magnetic axis to shift outward in a phenomenon known as the Grad-Shafranov shift. The radial displacement from the centerline of the torus can be approximated by:

$$\Delta \approx \frac{2\mu_0 p}{B_p} \frac{a^2}{R_0} \quad (1.13)$$

The two scenarios presented in Fig. 1.3 differ by their major radius. As the Grad-Shafranov shift is inversely proportional to  $R_0$ , we expect that the larger curvature in the case 1.3b  $R_0 = 0.5\text{m}$  induces a larger shift, which is precisely what is observed.

### 1.1.4. Realisation of magnetic configurations

The magnetic tokamak configuration in a tokamak is controlled by a set of coils. An example of the technical realisation in the ITER tokamak is shown in Fig. ???. The fundamental configuration discussed before, is created by the toroidal field coils

## 1. Tokamak Concept – 1.1. Particles in a magnetized plasma

encircling the plasma chamber, appear in orange on the scheme. As it from the name, they drive the toroidal magnetic field  $B_\varphi$ . The poloidal field, necessary for the helical path of confined plasma particles, is driven by a strong toroidal current, itself induced by the central solenoid (central column with yellow ends).

They are completed by poloidal field coils (light purple), placed outside the main plasma chamber and distributed along the height of the tokamak. They generate a poloidal magnetic field that wraps around the plasma with the minor radius, perpendicular to the toroidal field. By adjusting the current, it is possible to control the vertical position, elongation, and triangularity of the plasma. For example, increasing the current in certain poloidal coils can elongate the plasma, giving it an oval cross-section, or induce triangularity by pulling the plasma boundary inward at the top and bottom.

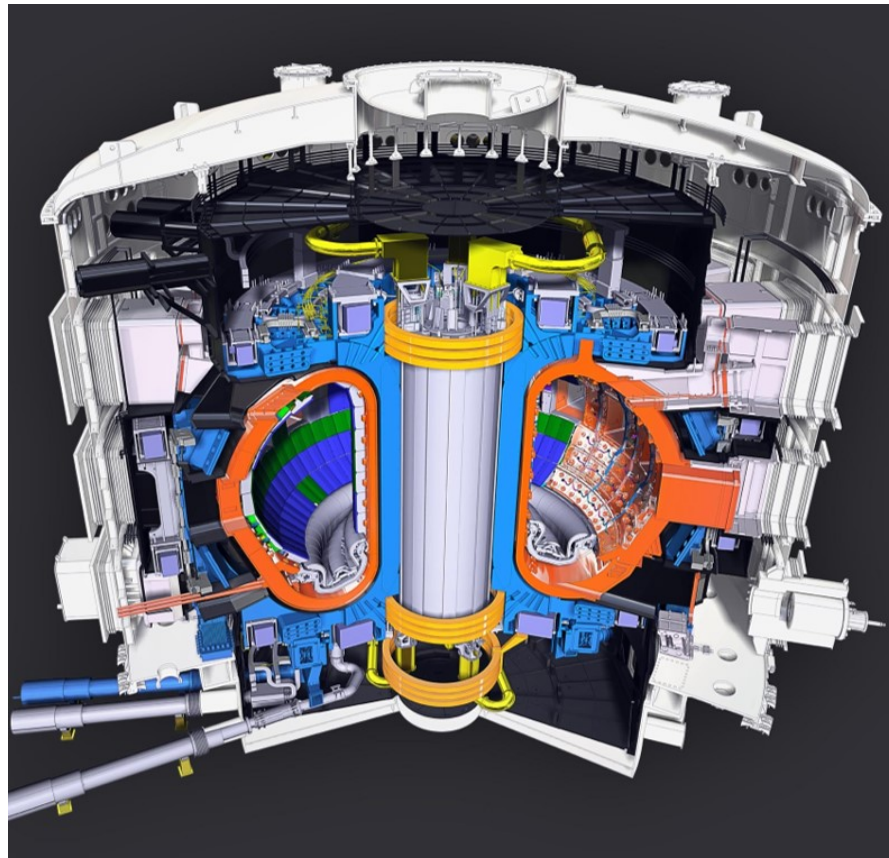


Figure 1.4.: Cutaway of the ITER tokamak (source: ITER Organization)

The limited configuration is one of the simpler magnetic configurations in a tokamak. In this setup, the plasma is in direct contact with material components which act as a limiter (see Fig. 1.5a). The confined plasma boundary is given by the last closed flux surface, tangential to the wall in one point. Such a configuration suffers from significant power loads on the limiters, resulting in high erosion rates and potential contamination of the plasma with impurities. The confinement is generally lower in

## 1. Tokamak Concept – 1.1. Particles in a magnetized plasma

this configuration.

A diverted configuration, as depicted in Fig. 1.5b, improves the situation by a lot. The poloidal field coils shape the magnetic field lines in a fashion that they do not intersect with solid surfaces within the main plasma chamber but are instead directed to a separate region called the divertor. The last closed flux surface is then called "separatrix" and never touches the tokamak wall. It effectively splits the domain in a confined core region with closed field lines and the Scrape-Off-Layer (SOL), that extends to the wall and where field lines are open, e.g. they cross the wall. The poloidal magnetic field contains now a singularity, the "X-point", and the area where the divertor plate intercepts the continuation of the separatrix is called the "target line". The divertor handles the exhaust of heat and particles from the plasma and this configuration tends to improve overall plasma confinement and reduce impurity levels.

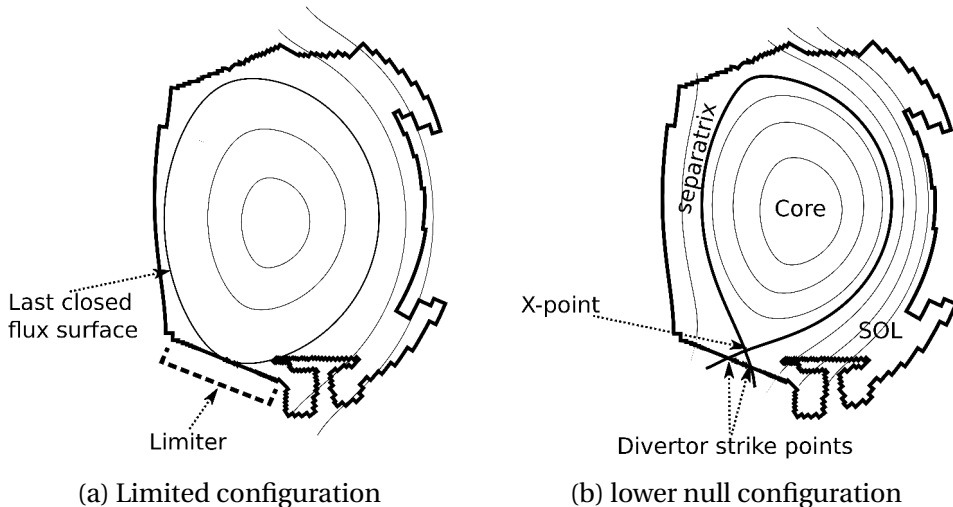


Figure 1.5.: Comparison of the limited and diverted configuration on a WEST geometry.

More exotic configurations are also feasible. In the double-null configuration, there are two divertor regions, typically located above and below the main plasma body. It splits heat loads on both divertor targets and can improve symmetry in power and particle exhaust. This symmetry helps in balancing the plasma dynamics and stabilizing the plasma, particularly with respect to vertical displacement events (VDEs), which are large-scale instabilities that can occur in tokamaks. Similarly, the X-point can be a higher-order singularity and split in more than four branches, spreading the heat load in several branches[54]. Such "snowflake" divertors can be achieved with an additional set of poloidal field coils in proximity to the divertor.

Another important parameter of the magnetic configuration is its triangularity. It refers to the shaping of the plasma cross-section, where the plasma boundary is not circular but has an elongated shape with triangular indentations. The degree of triangularity  $\delta$  measures the extent of the indentation relative to the plasma's minor radius.

## 1. Tokamak Concept – 1.2. Interaction between particles

High triangularity configurations can enhance plasma stability and confinement, in particular in the edge region, by allowing for higher pressure gradients.

## 1.2. Interaction between particles

So far we have seen how particles are confined in magnetic field lines. It gives only a partial picture of the physical processes that occur in a tokamak. A plasma contains positively and negatively charged particles at high energetic levels and they will inevitably interact between themselves. In Sec. 1.2.1 we look at how electrons and ions organize to form a state of quasi-neutrality, in Sec. 1.2.2 we dive into the mechanisms that drive particle collisions and in Sec. ?? we conclude how collisions translate into resistive effects.

### 1.2.1. Debye shielding

Debye shielding refers to the macroscopic phenomenon that electric fields naturally dissipate in a plasma at rest. When a charged particle is introduced into a plasma, electrons, being lighter and more responsive than ions, quickly redistribute themselves around the introduced charge. There is then a localized region of increased electron density that counteracts the introduced electric field. The characteristic length over which this electric field is significantly attenuated is known as the Debye length  $\lambda_D$ :

$$\lambda_D = \sqrt{\frac{\epsilon_0 T_e}{n_e e^2}} \quad (1.14)$$

The Coulomb potential around a point charge  $Q$  exponentially decreases for distances beyond the Debye length:

$$\Phi(r) = \frac{Q}{4\pi\epsilon_0 r} e^{-r/\lambda_D} \quad (1.15)$$

It effectively means that at scales larger than  $\lambda_D$ , the plasma can be considered quasi-neutral, where the electron density compensates the charge of all present ions.

$$n_e = \sum_i q_i n_i \quad (1.16)$$

### 1.2.2. Particle collisions

At scales below the Debye length, the Coulomb force

$$\mathbf{F}_C = \frac{q_1 q_2}{4\pi\epsilon_0} \frac{\mathbf{r}}{\|\mathbf{r}\|^3} \quad (1.17)$$

drives collisions between two particles with charges  $q_1$  and  $q_2$  at a distance  $\mathbf{r} = \mathbf{r}_2 - \mathbf{r}_1$ , where  $\epsilon_0$  is the vacuum permittivity. By Newton's first and third laws of motion, this

## 1. Tokamak Concept – 1.2. Interaction between particles

force defines the acceleration of each particle  $m_{1/2} \frac{d^2 \mathbf{r}_{1,2}}{dt^2} = \mathbf{F}_{12/21}$  and acts in opposite directions  $\mathbf{F}_{12} = -\mathbf{F}_{21}$  for the respective particles.

Following the derivation in Chapter 3 of Hutchinson et al. [32], we can combine the two equations of motion to express the dynamics of a single particle (projectile) with position  $\mathbf{r}$  and reduced mass  $m_r = \frac{m_1 m_2}{m_1 + m_2}$ , that collides with a stationary second particle (target) at the origin. This description corresponds to a reference frame attached to the common center of mass. For an initial velocity  $\mathbf{v}_r$ , the projectile will be deviated by the collision as represented in Fig. 1.6.

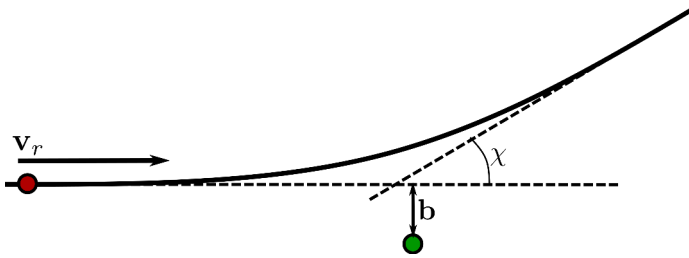


Figure 1.6.: Trajectory of the projectile particle (red) colliding with the target particle (green). The vector  $\mathbf{b}$  denotes the impact factor and  $\chi$  is the deflection angle caused by the collision.

To conserve angular momentum, the deflection of the projectile depends on the impact factor or the distance  $b = \|\mathbf{b}\|$  of the initial trajectory to the target. Let

$$b_{90} = \frac{q_1 q_2}{4\pi\epsilon_0} \frac{1}{m_r \|\mathbf{v}_r\|^2} \quad (1.18)$$

be the impact factor at which the projectile is deflected by a  $90^\circ$  angle. We can then express the deflection angle  $\chi$  at a given  $b$ :

$$\chi = \tan^{-1} \frac{b_{90}}{b} \quad (1.19)$$

This angle represents the deflection of the particle relative to the common center of mass. If we now consider two individual particles with finite mass, where the projectile approaches a stationary target with velocity  $\mathbf{v}_1 = (v_1, 0)^T$ , the deflection observed in an external frame is approximately  $\chi_1 \approx \frac{m_2}{m_1 + m_2} \chi$  (using the small angle approximation). To conserve momentum in the initial direction, the target also starts moving. The projectile exits the collision with:

$$\mathbf{v}'_1 = \left( \frac{\frac{m_1 v_1}{m_1 + m_2} + \frac{m_2 v_1}{m_1 + m_2} \cos \chi}{\frac{m_2 v_1}{m_1 + m_2} \sin \chi} \right) \quad (1.20)$$

## 1. Tokamak Concept – 1.2. Interaction between particles

At each collision, kinetic energy is transferred, and the projectile loses:

$$\begin{aligned}\Delta K = K - K' &= \frac{1}{2} m_1 \|\mathbf{v}_1\|^2 - \frac{1}{2} m_1 \|\mathbf{v}'_1\|^2 \\ &= \frac{2m_1^2 m_2}{(m_1 + m_2)^2} v_1^2 \sin^2 \frac{\chi}{2} \\ &\approx \frac{2m_1^2 m_2}{(m_1 + m_2)^2} v_1^2 \left( \frac{b_{90}}{b} \right)^2\end{aligned}\quad (1.21)$$

where the last line uses the small angle approximation  $\chi \ll 1$ .

In practice, we do not want to study every collision but are interested in the total number of collisions a particle experiences over a given length when traversing a medium with density  $n$ . For that, we consider all collisions with particles at an impact factor between  $b$  and  $b + db$  over a distance  $dx$  (see Fig. 1.7). This means we look at the volume  $V = 2\pi bdbdx$  in which we count a total of  $nV$  collisions.

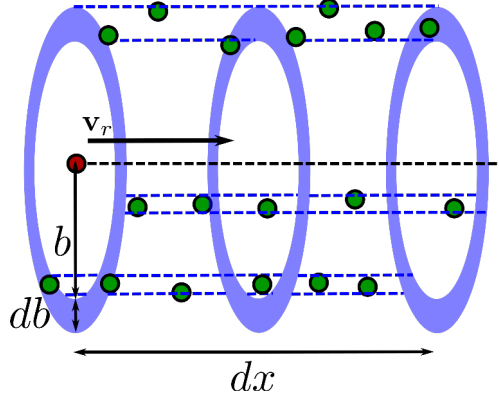


Figure 1.7.: Volume for given  $db$  and  $dx$  in which collisions on the projectile are considered.

Using Eq. 1.21 for the energy loss at each collision, we can estimate the energy our projectile loses after all collisions with the targets in the volume:

$$\Delta_V K = \frac{2m_1^2 m_2}{(m_1 + m_2)^2} v_1^2 \left( \frac{b_{90}}{b} \right)^2 n 2\pi bdbdx \quad (1.22)$$

The stopping power  $\frac{dK}{dx}$  describes the rate of energy loss per unit path length. It requires integrating over all possible impact factors  $b$ :

$$\frac{dK}{dx} = \frac{2m_1^2 m_2}{(m_1 + m_2)^2} v_1^2 n 2\pi b_{90}^2 \int_{b_{min}}^{b_{max}} \frac{1}{b} db \quad (1.23)$$

This integral diverges in both limits  $b_{min} \rightarrow 0$  and  $b_{max} \rightarrow \infty$ . We need to define cut-off values:

- $b_{min} = b_{90}$  because the small angle approximation in Eq. 1.21 implies that

$$b > b_{90}$$

- $b_{max} = \lambda_D$  because the Coulomb potential from Eq. 1.15 vanishes quickly at distances beyond the Debye length and so does the effective Coulomb force  $\mathbf{F}_C$

With these bounds, we evaluate the integral and define the Coulomb logarithm:

$$\ln \Lambda = \int_{b_{90}}^{\lambda_D} \frac{1}{b} db = \ln \left( \sqrt{\frac{\epsilon_0 T_e}{n_e e^2}} \right) - \ln \left( \frac{q_1 q_2}{4\pi \epsilon_0} \frac{1}{m_r \|\mathbf{v}_r\|^2} \right) \quad (1.24)$$

For ion-ion collisions, masses  $m_1 = m_2$  and charges  $q_1 = q_2$  are equal. The collision frequency  $\omega_c$  describes at which rate a particle loses energy through collisions relative to its total energy. The power loss is proportional to the stopping power with the particle velocity  $\frac{dK}{dt} = v \frac{dK}{dx}$ . We can then relate  $\omega_c$  to the stopping power:

$$\omega_c = \frac{v}{K} \frac{dK}{dx} \quad (1.25)$$

If we now inject Eqs. 1.19, 1.23 and 1.24 we obtain following expression for  $\omega_c$ :

$$\omega_c = \frac{q^4 n}{16\pi \epsilon_0^2 \sqrt{2m} K^{3/2}} \ln \Lambda \quad (1.26)$$

Assuming that the kinetic energy follows directly the plasma temperature with the relation  $K = 3/2T$ , we can express the characteristic collision time  $\tau_c$  and mean free path  $\lambda_c$ :

$$\tau_c = \frac{1}{\omega_c} = \frac{52\sqrt{3}\pi \epsilon_0^2 \sqrt{m}}{q^4 \ln \Lambda} \frac{T^{3/2}}{n} \quad (1.27)$$

$$\lambda_c = \frac{v}{\omega_c} = \frac{32\sqrt{3/2}\pi \epsilon_0^2}{q^4 \ln \Lambda} \frac{T^2}{n} \quad (1.28)$$

It is worth noting that  $\tau_c$  is proportional to  $T^{3/2}/n$  and  $\lambda_c$  to  $T^2/n$  as all other terms are near-constant for a given ion in a tokamak.

## 1.3. Scrape-Off-Layer

### 1.3.1. Fundamental sheath physics

The SOL is characterized by open flux surfaces and where magnetic field lines cross the wall, the quasi-neutrality assumption from Sec. 1.2.1 does not hold anymore. The much lighter electrons travel much faster towards the wall (about  $\sqrt{m_i/m_e}$  faster than ions), creating a net negative charge in the direct proximity to the wall. It is not until a

few Debye lengths  $\lambda_D$  before shielding restores known plasma conditions forming a region known as "electrostatic sheath". The negative charge attracts ions and repulses electrons, and we can assume that the electron density decreases exponentially approaching the wall. This eventually leads to the Bohm criterion[50], which states that at the sheath entrance the ion speed must be equal or larger than the sound speed of the plasma.

$$v_{se} \geq c_s = \sqrt{\frac{T_i + T_e}{m_i}} \quad (1.29)$$

From there, it is possible to calculate a sheath particle flux:

$$\gamma_{se} = n v_{se} \quad (1.30)$$

and a heat flux:

$$q_{se} = \gamma n T \gamma_{se} \quad (1.31)$$

with the sheath transmission coefficient  $\gamma$ . As the sheath is not collisional, these coefficients have to be determined from kinetic theory[61]. For hydrogen plasma, it is common to take the values  $\gamma_i = 2.5$  for ions and  $\gamma_e = 4.5$  for electrons.

### 1.3.2. Confinement characteristics

An important metric for the confinement quality is the ratio  $\beta$  of plasma pressure over magnetic pressure.

$$\beta = \frac{p}{p_{mag}} = \frac{n e T}{B^2 / 2\mu_0} \quad (1.32)$$

There is a concurrent dynamic between thermodynamic and magnetic pressures: the former exerts an expansive force on the plasma, while the latter seeks to confine the plasma particles within their magnetic flux surfaces. A lower value of  $\beta$  is generally desired for a more effective plasma confinement, but requires strong magnetic fields. However, generating such intense magnetic fields entails considerable costs and technical challenges.  $\beta$  typically takes values between 1% and 5% in present large tokamaks.

It is possible to distinguish between two operational regimes: L-mode and H-mode. The (L)ow-confinement mode is the standard operational mode. The plasma loses much of its energy to the wall with a consequent short confinement time. In 1982, the (H)igh-confinement mode was first observed on ASDEX in Germany and subsequently thoroughly investigated[66]. Its key feature is a strong reduction of turbulence around the separatrix, which reduces particle transport from the core to the SOL. As a consequence, temperature and density gradients steepen, forming a "pedestal" and creating a transport barrier.

### 1.3.3. Problematic of heat exhaust

An important part of the heat produced in a tokamak, whether it originates from external heating or from the fusion reaction, is evacuated by hot plasma particles. Cross-field transport allows confined particles from the hot core to cross the separatrix. As they enter the SOL, they follow the magnetic field lines until they impact the divertor on the thin target band. This region is extremely critical as large amounts of power are directed on a fairly small area. It is projected for ITER that heat loads at the targets are very close to material limits[23]. The peak heat flux  $q_{peak}$  could reach values over  $10\text{MW/m}^2$ . For a safe tokamak operation, it is essential to well understand and predict heat fluxes on the strike points. An important metric to take into the consideration is the heat flux o power fall-off width  $\lambda_q$ . It describes the spread of the heat flux on the divertor targets, and a larger value allows to spread the power exhaust on a larger area. It allows to describe the heat flux at a distance  $r$  from the target:

$$q(r) = q_{peak} e^{-\frac{r}{\lambda_q}} \quad (1.33)$$

Eich et al.[18] developed a scaling law to estimate  $\lambda_q$  for H-mode operation based on machine parameters. It states that the width is inversely proportional to the toroidal magnetic field  $\lambda_q \propto B_\varphi^{-0.8}$ , meaning that larger machines with stronger coils will also have a thinner target line.

## 2. Description of Plasmas

Plasmas can be modeled using various sets of equations that trade off between accuracy and computational feasibility. Generally, more accurate models are prohibitively expensive and are beyond the capabilities of current high-performance computing (HPC) infrastructure when applied to large systems. In this chapter, we introduce the major approaches that are used nowadays, with a special care to highlight how they are connected and where they differ. The most comprehensive approach in Sec. 2.1 rely on plasma particles themselves or their statistical distribution. From there, the Chapman-Enskog expansion in Sec. 2.2 allows to express conservation equations on averaged plasma quantities and lay the foundations for fluid models. Finally, MHD models in Sec. 2.3 offer a framework to combine those conservation equations with the evolution of electromagnetic properties of the plasma.

### 2.1. Direct description of Plasma Particles

Particles are the foundation of the first set of models. They can either be solved individually as in Sec. 2.1.1 or represented by their distribution functions in the so-called kinetic models (Sec. 2.1.2).

#### 2.1.1. Particle Tracking

In the most general description, each particle in a tokamak—whether neutron, ion, atom, or electron—is represented individually with three degrees of freedom for both position  $\mathbf{x}$  and velocity  $\mathbf{v}$ . The system’s dynamics are governed by the Lorentz force:

$$\frac{\partial \mathbf{v}}{\partial t} = \mathbf{F} = q\mathbf{E} + q\mathbf{v} \times \mathbf{B} \quad (2.1)$$

$$\frac{\partial \mathbf{x}}{\partial t} = \mathbf{v} \quad (2.2)$$

where  $\mathbf{E}$  is the electric field,  $\mathbf{B}$  the magnetic field, and  $q$  the charge of the particle. Given that a medium-sized tokamak like WEST contains approximately  $N_p \approx 10^{20}$  particles, each with six degrees of freedom, direct numerical simulation is infeasible. Computational effort can be reduced by using macro-particles, which represent many real particles. A prominent approach utilizing this concept is the particle-in-cell (PIC) method [67], where macro-particles evolve in pre-calculated fields on a mesh or interact directly with one another. PIC methods are employed to study phenomena such

as collisions with neutral particles [2], plasma-wall interactions [35], or instabilities induced by fusion products [9].

### 2.1.2. Kinetic Models

As a further abstraction, an ensemble of particles can be described statistically through a distribution function  $f(\mathbf{x}, \mathbf{v}, t)$ . This kinetic description replaces individual particles with a probability distribution, avoiding the need to calculate exact positions and velocities at each moment in time. The behavior of the distribution function is governed by the Boltzmann equation:

$$\frac{\partial f}{\partial t} + \mathbf{v} \cdot \nabla_{\mathbf{x}} f + \frac{\mathbf{F}}{m} \cdot \nabla_{\mathbf{v}} f = C_{\text{coll}} + C_{\text{other}} \quad (2.3)$$

where  $C_{\text{coll}}$  represents the collision operator, handling Coulomb collisions as introduced in Sec. 1.2.2, and  $C_{\text{other}}$  includes additional source terms. Substituting the force vector  $\mathbf{F}$  with the Lorentz force (Eq. 2.1) yields the Vlasov equation.

To achieve sufficient accuracy, approximately  $N_x = 10^9$  spatial discretization points and  $N_\sigma = 10^6$  points for the distribution function are required. Considering that both position and velocity have three components each, this results in  $6 \cdot 10^{15}$  degrees of freedom—significantly fewer than in the particle description.

Further simplification is achieved through the gyrokinetic approach. While particles in a plasma predominantly follow magnetic field lines, their motion forms a helical trajectory characterized by the Larmor frequency and radius:

$$\omega_L = \frac{qB}{m} \quad l_L = \frac{mv_\perp}{qB} \quad (2.4)$$

This allows the elimination of one degree of freedom in the distribution function, as the velocity can be described by its parallel component  $v_\parallel$  along the magnetic field line and its perpendicular component  $v_\perp$ . This simplification is valid only when the Larmor frequency and radius are much smaller than any characteristic frequency or length in the system, which is typically true in the core of the tokamak but not in the scrape-off layer (SOL), where the gyrokinetic approach is less suitable.

## 2.2. Three Fluid Moments of the Kinetic Equation

Deriving transport equations for plasma quantities analogous to the Navier-Stokes equations in classical fluid dynamics is highly desirable. Such an approach would enable the use of established computational fluid dynamics (CFD) methods for turbulence modeling, significantly reducing the number of degrees of freedom. Starting with the distribution function  $f$ , the  $k$ -th moment of the transport equation is obtained by applying the tensor product  $\mathbf{v} \otimes \dots$   $k$  times and then integrating over the velocity:

## 2. Description of Plasmas – 2.2. Three Fluid Moments of the Kinetic Equation

$$\mathcal{M}^k = \int_{\mathbf{v}} f \mathbf{v}^k d\mathbf{v}^3 \quad (2.5)$$

Substituting the kinetic equation 2.3 into this expression yields the following equation for the  $k$ -th moment:

$$\begin{aligned} \partial_t \int_{\mathbf{v}} f \mathbf{v}^k d\mathbf{v}^3 + \int_{\mathbf{v}} \mathbf{v}^k \nabla_{\mathbf{x}} f d\mathbf{v}^3 + \int_{\mathbf{v}} \mathbf{v}^k \frac{\mathbf{F}}{m} \cdot \nabla_{\mathbf{v}} f d\mathbf{v}^3 &= \int_{\mathbf{v}} \mathbf{v}^k C d\mathbf{v}^3 \\ \partial_t \mathcal{M}^k + \nabla_{\mathbf{x}} \cdot \mathcal{M}^{k+1} - \frac{k}{m} \mathbf{F} \otimes \mathcal{M}^{k-1} &= \int_{\mathbf{v}} \mathbf{v}^k C d\mathbf{v}^3 \end{aligned} \quad (2.6)$$

Expressing the  $k$ -th moment requires knowledge of the  $k-1$ -th and  $k+1$ -th moments. Consequently, a fully consistent plasma description would require infinitely many equations, which is impractical. Therefore, we typically consider only the first three moments, using fluid closures to compensate for the missing higher-order equations. These moments effectively allow us to replace a particle-based description with averaged quantities:

$$\text{Particle density: } \mathcal{M}^0 = n = \int_{\mathbf{v}} f d\mathbf{v}^3 \quad [\text{m}^{-3}] \quad (2.7)$$

$$\text{Momentum density: } \mathcal{M}^1 = \boldsymbol{\gamma} = n \mathbf{u} = \int_{\mathbf{v}} f \mathbf{v} d\mathbf{v}^3 \quad [\text{m}^{-2} \cdot \text{s}^{-1}] \quad (2.8)$$

$$\text{Pressure tensor: } m \mathcal{M}^2 = \boldsymbol{\Pi} = m \int_{\mathbf{v}} f \mathbf{v} \otimes \mathbf{v} d\mathbf{v}^3 \quad [\text{kg} \cdot \text{m}^{-1} \cdot \text{s}^{-2}] \quad (2.9)$$

where  $\mathbf{u}$  is the fluid velocity and  $m$  the particle mass. This framework sets the stage for deriving the three fundamental conservation equations for fluid models of plasmas.

### 2.2.1. Mass Balance ( $k = 0$ )

Starting from Eq. 2.3, the mass balance equation for the unknowns  $n$  and  $\mathbf{u}$  is derived as follows:

$$\partial_t n + \nabla \cdot (n \mathbf{u}) = S_n \quad (2.10)$$

This equation provides one relation but involves four unknowns, necessitating additional equations to fully describe the system. The term  $S_n$  accounts for particle sources arising from non-elastic collisions in  $C_{\text{other}}$ , such as ionization or recombination processes.

### 2.2.2. Momentum Balance ( $k = 1$ )

For the first moment equation, we multiply the Boltzmann equation 2.3 by  $\mathbf{v}$  and integrate over the velocity space, yielding:

$$\partial_t \left( \int_{\mathbf{v}} \mathbf{v} f d\mathbf{v} \right) + \int_{\mathbf{v}} \mathbf{v} \otimes \mathbf{v} \cdot \nabla_{\mathbf{x}} f d\mathbf{v} + \int_{\mathbf{v}} \mathbf{v} \frac{\mathbf{F}}{m} \cdot \nabla_{\mathbf{v}} f d\mathbf{v} = \int_{\mathbf{v}} C v d\mathbf{v} \quad (2.11)$$

To simplify the tensor product, we decompose the velocity  $\mathbf{v}$  into the fluid velocity  $\mathbf{u}$  and a new quantity  $\mathbf{w}$ , such that  $\mathbf{v} = \mathbf{u} + \mathbf{w}$ . We introduce the static pressure tensor:

$$\mathbf{P} = m \int_{\mathbf{w}} f \mathbf{w} \otimes \mathbf{w} d\mathbf{w} \quad (2.12)$$

The pressure tensor  $\mathbf{\Pi}$  can then be expressed as:

$$\mathbf{\Pi} = m \int_{\mathbf{w}} f \mathbf{u} \otimes \mathbf{u} d\mathbf{w} + m \int_{\mathbf{w}} f \mathbf{w} \otimes \mathbf{w} d\mathbf{w} = mn \mathbf{u} \otimes \mathbf{u} + \mathbf{P} \quad (2.13)$$

Substituting this into the first moment equation, we obtain the conservation equation for momentum:

$$m \partial_t (n \mathbf{u}) + m \nabla \cdot (n \mathbf{u} \otimes \mathbf{u} + \mathbf{P}) = q n \mathbf{E} + q n \mathbf{u} \times \mathbf{B} + S_u + R \quad (2.14)$$

Here,  $S_u$  represents the momentum source term, and  $R$  accounts for friction, both arising from  $C_{\text{coll}}$  and  $C_{\text{other}}$ .

### 2.2.3. Energy Balance ( $k = 2$ )

Finally, to solve for the static pressure tensor  $\mathbf{P}$ , we assume isotropic pressure in the plasma, simplifying the pressure tensor to a scalar pressure  $p$  such that  $\mathbf{P} = p \mathbf{I}$ . This reduces the nine unknowns in  $\mathbf{P}$  to a single scalar  $p$ . Given that  $p = nT$ , the second moment can be expressed as an energy conservation equation. The total energy density  $\epsilon$  is the sum of kinetic and thermal energy in the plasma:

$$\epsilon = \frac{3}{2} n T + \frac{1}{2} m n \|\mathbf{u}\|^2 \quad (2.15)$$

To derive a conservation equation for  $\epsilon$ , we multiply Vlasov's equation 2.3 by the kinetic energy per unit mass:

$$\partial_t \left( \int_{\mathbf{v}} \frac{1}{2} u^2 f d\mathbf{v} \right) + \int_{\mathbf{v}} \frac{1}{2} u^2 \mathbf{v} \cdot \nabla_{\mathbf{x}} f d\mathbf{v} + \int_{\mathbf{v}} \frac{1}{2} u^2 \frac{\mathbf{F}}{m} \cdot \nabla_{\mathbf{v}} f d\mathbf{v} = \int_{\mathbf{v}} \frac{1}{2} u^2 C d\mathbf{v} \quad (2.16)$$

This simplifies to:

$$\partial_t \epsilon + m \nabla \cdot (\epsilon \mathbf{u} + [n \mathbf{u} \otimes \mathbf{u} + \mathbf{P}] \cdot \mathbf{u} + \mathbf{q}) = q n \mathbf{E} \cdot \mathbf{u} + Q + R_{\epsilon} \quad (2.17)$$

## 2. Description of Plasmas – 2.3. MHD description of plasmas

The collisional heat flux  $\mathbf{q}$  arises from the fluid closure, replacing all higher-order moments. The term  $Q$  represents a collisional heat source, while  $R_\epsilon$  accounts for sources associated with non-Coulombian collisions in  $C_{\text{other}}$ . Notably, the magnetic field term  $\mathbf{u} \times \mathbf{B}$  does not appear in the energy equation, as the torque  $\frac{1}{2} u^2 \mathbf{u} \times \mathbf{B} \cdot \nabla_{\mathbf{v}} f$  does not perform work and therefore does not contribute to energy changes.

The three conservation equations for density  $n$ , momentum  $\gamma$ , and energy  $\epsilon$  form the foundation of the SOLEDGE3X model. These terms will be further developed in Chapter 4.1.

## 2.3. MHD description of plasmas

In the magnetohydrodynamics (MHD) approach, the conservation equations are coupled to Maxwell's and Ohm's laws, introducing electromagnetic behavior into the system. Unlike earlier models, the magnetic equilibrium is not static; the electric and magnetic fields evolve over time. MHD models typically differentiate between ideal MHD and extended models that include resistive and two-fluid effects, which are essential for accurately describing tokamak plasmas. The ideal MHD model and its extension with tokamak-specific terms in Sec. 2.3.1 is the most accurate approach to simulate the electromagnetic intrications in plasmas. Fast wave dynamics represent a major restriction and reduced models in Sec. 2.3.2 are therefore much more widespread.

### 2.3.1. Extended MHD Model

Many of the explanations in this section are based on the lecture notes by E. Franck[41]. The complete set of MHD equations is as follows:

$$m\partial_t n + \nabla \cdot (n\mathbf{u}) = 0 \quad (2.18)$$

$$mn\partial_t \mathbf{u} + mn\mathbf{u} \cdot \nabla \mathbf{u} + \nabla p = \mathbf{j} \times \mathbf{B} \boxed{-\nabla \cdot \boldsymbol{\Pi}} \quad (2.19)$$

$$\frac{3}{2}\partial_t p_i + \frac{3}{2}\mathbf{u} \cdot \nabla p_i + \frac{5}{2}p_i \nabla \cdot \mathbf{u} = \boxed{-\nabla \cdot \mathbf{q}_i - \nabla \cdot (\boldsymbol{\Pi}_i : \nabla \mathbf{u})} \quad (2.20)$$

$$\frac{3}{2}\partial_t p_e + \frac{3}{2}\mathbf{u} \cdot \nabla p_e + \frac{5}{2}p_e \nabla \cdot \mathbf{u} = \boxed{-\nabla \cdot \mathbf{q}_e - \nabla \cdot (\boldsymbol{\Pi}_e : \nabla \mathbf{u}) + \eta \|\mathbf{j}\|^2 + \frac{3}{2}\mathbf{j} \cdot \mathcal{P}} \quad (2.21)$$

$$\partial_t \mathbf{B} = -\nabla \times \left( -\mathbf{u} \times \mathbf{B} \boxed{+ \eta \mathbf{j} - \mathcal{P} + \mathcal{H}} \right) \quad (2.22)$$

$$\nabla \cdot \mathbf{B} = 0 \quad (2.23)$$

$$\nabla \times \mathbf{B} = \mu_0 \mathbf{j} \quad (2.24)$$

Equations 2.18 through 2.24 are derived directly from the fluid moments described in Sec. 2.2, where the pressure replaces the energy and is solved for both ions and electrons. These equations are coupled with Ohm's law (Eq. 2.22) under the magnetostatic assumption, Gauss's law for magnetism (Eq. 2.23), and Ampère's law (Eq.

## 2. Description of Plasmas – 2.3. MHD description of plasmas

[2.24](#)). In ideal steady-state, we see that the momentum balance is dominated by the equilibrium between thermodynamic and magnetic forces  $\nabla p = \mathbf{j} \times \mathbf{B}$ . In combination with Ampère's law, all components are available to derive the Grad-Shafranov equation [1.12](#) as it has been done in Sec. [1.1.3](#).

The terms enclosed in boxes represent the additional terms required for extending the model from ideal MHD. These include viscous-resistive effects, as well as a pressure term  $\mathcal{P}$  and a Hall term  $\mathcal{H}$ . Without these boxed terms, the system describes the ideal MHD model. Linearizing the ideal MHD equations results in three types of waves:

- **Alfvén waves:** These incompressible waves cause the magnetic field lines to bend and propagate only in the parallel direction. In the low-beta limit, their propagation speed,  $v_A^2 = \frac{B^2}{mn\mu_0}$ , is much greater than the speed of sound in the plasma,  $c_s^2 = \frac{eT}{m}$ .
- **Slow magnetoacoustic waves:** These waves propagate only in the parallel direction, causing compression in the plasma without perturbing the magnetic field lines. Their propagation speed  $v_s$  is similar to the speed of sound.
- **Fast magnetoacoustic waves:** These waves can propagate in any direction and compress magnetic field lines. They have a propagation speed approximately given by  $v_f^2 = v_A^2 + c_s^2$ .

Fast waves, in particular, pose challenges for numerical modeling as they require very small timesteps and implicit methods to be accurately resolved. The full MHD model introduces two additional dispersive waves into the system.

### 2.3.2. Reduced MHD model

To eliminate the fast magnetoacoustic waves and to reduce the size of the system, physicists often resort to reduced MHD models. Instead of solving for all components of  $\mathbf{B}$ , we decompose the magnetic field into the poloidal flux  $\Psi$  and the toroidal field function  $F$  as in Eq. [1.7](#). The toroidal field  $B_\phi$  and  $F$  are imposed, so we only remain with the unknown scalar  $\Psi$  to replace the three unknowns of  $\mathbf{B}$ . As a reminder from Sec. [1.1.3](#),  $\Psi$  is equivalent to the toroidal component  $A_\phi$  of the magnetic vector potential and uniquely defines the poloidal field  $B_p$ . Consequently, Ampère's law [2.24](#) reduces to:

$$\mu_0 j_\phi = \Delta^* \Psi = R^2 \nabla \cdot \left( \frac{1}{R^2} \nabla_p \Psi \right) \quad (2.25)$$

with the poloidal gradient  $\nabla_p$ .

In the second simplification for the reduced MHD model, the velocity vector is decomposed into a parallel and a perpendicular component. The projected fields are:

$$u_{\perp} = \mathbf{e}_{\varphi} \cdot \nabla \times (R^2 \mathbf{u}) \quad (2.26)$$

$$u_{\parallel} = \mathbf{B} \cdot \mathbf{u} \quad (2.27)$$

$$(2.28)$$

This projection is consequently applied to all terms in the momentum conservation equation 2.19, that can then be solved independently for both velocities. In addition to reducing the number of equations from three to two, it permits to split the slow magnetoacoustic waves, that propagate at sound speed in the parallel directions, from the much slower dynamics in the poloidal plane that consist of electric and diamagnetic drifts (A proper introduction to the various plasma drifts will be given in the next chapter).

## 2.4. Fluid closures

We only considered MHD models up to the second moment. To maintain the validity of the model, we need additional closure terms in the momentum and energy equations. They rely on the fact that plasma collisions dominate higher-order moments.

### 2.4.1. Spizer-Härm model

,

### 2.4.2. Braginskii and Zhdanov closures

### 2.4.3. Reduced Ohm's law

### 3. Drift-reduced models for plasma turbulence

The mechanisms at play at the plasma boundary result from the complex interplay of transport processes in the plasma, losses at the wall, and complex atomic and molecular interactions. In this region, particles experience very fast transport along the magnetic field lines and slower, often turbulence-driven, anomalous cross-field transport [42]. The ratio between these phenomena characterizes the decay length of density and temperature profiles, which further determine the confinement quality of the core plasma and the total heat exhaust on the divertor target.

The difficulty in obtaining global experimental measurements in tokamaks requires complementary numerical simulations. Currently, these numerical data are essential to complement experimental measurements and support their interpretation. In the longer term, they will be used to make predictions and support the design of ITER experiments. Self-consistent simulations of the plasma edge are challenged by a complex geometry and the variety of involved scales. The magnetic equilibrium exhibits both open and closed magnetic field lines, breaking the toroidal symmetry. Turbulent fluctuations typically have sizes on the order of the ion gyroradius  $\rho_\alpha$  ( $\geq 0.4$  mm) [30] in the perpendicular direction to the magnetic field lines, and compete with phenomena occurring along them on the order of the parallel connection length  $\propto q_s R_0$  (where  $q_s$  is the safety factor, and  $R_0$  the tokamak major radius), which can extend up to 100 meters.

In this context, kinetic models based on the particle distribution function [14, 34] are still limited to fundamental studies because of their very high numerical cost in a (5) 6-dimensional phase space. Thus, when realistic configurations are considered, reduced-dimension (2D/3D) fluid models remain the only feasible option for studying transport and turbulence at the edge of the plasma, although they are only rigorously valid in collisional regimes. A wide range of models have been derived in the literature and implemented in state-of-the-art codes [16, 21, 62] (see also an exhaustive presentation in the recent review by Schwander et al. [55]). The basic assumption they share is that the turbulence is characteristically low frequency and long wavelength in nature, leading to a strong scale separation between the parallel and perpendicular directions to the magnetic field. Therefore, the plasma fluid motion perpendicular to the magnetic field can be described explicitly by the so-called velocity drifts given by the quasi-static balance between Lorentz force, pressure gradient, and electromotive force due to magnetic and electric field inhomogeneities.

Sec. 3.1 introduces the origin of drift waves, main driver for plasma turbulence, and the drift-ordering approximation that typically applied in edge plasma.

## 3.1. Drift wave turbulence

### 3.1.1. Plasma drifts

Plasma drifts refer to the movement of charged particles under the influence of electric and magnetic fields. These drifts do not account for the primary motion along the guiding center, as described in Section 1.1.1. To study drift velocities, it is convenient to decompose every vector quantity into an average parallel component and a fluctuating perpendicular component, such that  $\mathbf{X} = X_{\parallel}\mathbf{b} + \mathbf{X}_{\perp}$ . We then express the Lorentz force equation as:

$$m\partial_t(v_{\parallel}\mathbf{b} + \mathbf{v}_{\perp}) = q [E_{\parallel}\mathbf{b} + \mathbf{E}_{\perp} + (v_{\parallel}\mathbf{b} + \mathbf{v}_{\perp}) \times \mathbf{B}] \quad (3.1)$$

Focusing on the particle's acceleration in the perpendicular direction, we derive the equation of motion:

$$m\partial_t\mathbf{v}_{\perp} = q [\mathbf{E} + (\mathbf{v}_{\perp} \times \mathbf{B})] \quad (3.2)$$

In steady-state conditions, the electric force compensates the Lorentz force, leading to the electric drift  $\mathbf{v}_E$ , commonly referred to as the "E cross B" or simply "ExB" drift:

$$\mathbf{v}_E = \frac{\mathbf{E}_{\perp} \times \mathbf{B}}{B^2} \quad (3.3)$$

This velocity applies uniformly to all particles at all times, as it depends only on the electric and magnetic fields in place. Since neither the mass nor the charge contributes to  $\mathbf{v}_E$ , both electrons and ions move in the same direction at the same speed, and under the quasi-neutrality assumption, no current is generated.

For the next drift, we consider the gyromotion of a particle in a non-uniform magnetic field. Under the adiabatic condition from Eq. 1.4, the magnetic moment  $\mu$  of the gyrating particle is conserved along its trajectory:

$$\mu = \frac{m\|\mathbf{v}_{\perp}\|^2}{2B} \quad (3.4)$$

This moment leads to a potential  $U = -\mu B$ , which exerts a force on the particle:

$$F_{\nabla B} = -\nabla U = \frac{mv_{\perp}^2}{2B} \nabla B \quad (3.5)$$

This force acts in the direction of the gradient  $\nabla B$ , where the magnetic field strength is lower, allowing the particle to reduce its potential energy. This results in the "grad B" drift:

$$\mathbf{v}_{\nabla B} = \frac{mv_{\perp}^2}{2q} \frac{\mathbf{B} \times \nabla B}{B^3} \quad (3.6)$$

— TALK ABOUT DIAMAGNETIC DRIFT ——

The helical configuration of a tokamak causes magnetic field lines to bend. To follow the direction of  $\mathbf{B}$ , the particle's trajectory is curved, and a centripetal force is exerted on the particle. With the curvature radius  $\mathbf{R}_c = \mathbf{b} \cdot \nabla \mathbf{b}$ , the force is given by:

$$\mathbf{F}_c = \frac{mv_{\parallel}^2}{R_c} \mathbf{R}_c = -mv_{\parallel}^2 \frac{\mathbf{B} \cdot \nabla \mathbf{B}}{B^2} \quad (3.7)$$

This force induces the "curvature" drift  $\mathbf{v}_c$ :

$$\mathbf{v}_c = \frac{mv_{\parallel}^2}{q} \frac{\mathbf{B} \times (\mathbf{B} \cdot \nabla \mathbf{B})}{B^4} \quad (3.8)$$

— STILL NEED THE POLARIZATION DRIFT —— The polarization drift occurs if the electric field in the plasma varies with time.

$$\mathbf{v}_p = \frac{m}{qB^2} \frac{d\mathbf{E}}{dt} \quad (3.9)$$

Note that the directions of "grad B", curvature or polarization drifts depend on the particle's charge, causing electrons and ions to move in opposite directions and generating an effective current. The total perpendicular velocity acting on a confined particle is the sum of all these drifts:

$$\mathbf{v}_d = \mathbf{v}_E + \mathbf{v}_{\nabla B} + \mathbf{v}_c + \mathbf{v}_p \quad (3.10)$$

In fact, any force perpendicular to the magnetic field will cause a drift:

$$\mathbf{v}_F = \frac{\mathbf{B} \times \mathbf{F}_{\perp}}{qB^2} \quad (3.11)$$

All other eventual forces, such as magnetic or gravitational forces, play a subordinate role in the plasma edge and are usually not considered in fluid models. Drift velocities are always orientated in perpendicular direction to then magnetic fields. They do not interfere with (the averaged) parallel fluxes, at a magnitude of  $v_{th}$ , and are primarily responsible for cross-field fluxes.

### 3.1.2. Drift-ordering approximation

We focus on low- $\beta$  collisional plasmas, typically found in the edge region of a tokamak. In such plasmas, we can define a characteristic length scale  $L_{\parallel}$  for parallel phenomena, which is on the order of the machine size (e.g., the major radius  $R$ ), where gradients in plasma fields such as density, temperature, or magnetic field strength are established. The perpendicular scale  $L_{\perp}$  is characteristic of cross-field structures. These scales

### 3. Drift-reduced models for plasma turbulence – 3.1. Drift wave turbulence

define the parallel and perpendicular wave numbers  $k_{\parallel}$  and  $k_{\perp}$ . In the drift ordering, the following relationships hold[59]:

$$\beta = \frac{2\mu_0(p_e + p_i)}{B^2} \ll 1 \quad \frac{\rho_L}{L_{\perp}} \sim \frac{\lambda_c}{L_{\parallel}} \ll 1 \quad (3.12)$$

where  $\rho_L$  is the ion Larmor radius, and  $\lambda_c$  is the mean free path between collisions. The electric force is much weaker than the magnetic force. Similarly, characteristic plasma frequencies should be much lower than the ion cyclotron frequency, giving rise to the following ordering parameters:

$$\epsilon_E = \frac{mE}{qB^2} \ll 1 \quad \epsilon_l = \frac{L_{\perp}}{L_{\parallel}} \ll 1 \quad \epsilon_t = \frac{\omega_{\perp}}{\omega_L} \ll 1 \quad (3.13)$$

The averaged gyromotion of particles is parallel to the magnetic field lines, with parallel velocities  $v_{\parallel} \approx \sqrt{2T/m}$  consistent with the kinetic energy in the plasma. Drift velocities, on the other hand, are typically much slower. Since  $\nabla B$  and the curvature radius  $R_c$  occur at machine scales  $L_{\parallel}$ , we can provide orders of magnitude for the three drifts introduced earlier:

$$v_E \sim \epsilon_E v_{\parallel} \quad v_{\nabla B} \sim \epsilon_l v_{\parallel} \quad v_c \sim \epsilon_l v_{\parallel} \quad v_p \sim \epsilon_t v_{\parallel} \quad (3.14)$$

This leads to the assumption in the Lorentz equation ?? that the perpendicular acceleration is negligible compared to parallel dynamics, such that  $m\partial_t v_{\perp} \approx 0$ . The perpendicular direction is assumed to always be in force equilibrium, allowing us to equate the terms  $\mathbf{v} \times \mathbf{B}$  and  $\mathbf{E}_{\perp}$ . Consequently, the polarization drift can be rewritten as:

$$\mathbf{v}_p = \frac{m}{qB^2} \mathbf{B} \times \frac{d\mathbf{v}}{dt} \quad (3.15)$$

Unlike other drifts, the polarization drift depends on the variation of the total velocity. To still obtain an expression for  $\mathbf{v}_{\perp}$ , we compute it in two steps, first considering the zeroth-order and then the first-order drifts:

$$\mathbf{v}_{\perp}^{(0)} = \mathbf{v}_E + \mathbf{v} \nabla B + \mathbf{v}_c \quad (3.16)$$

$$\mathbf{v}_{\perp}^{(1)} = \mathbf{v}_{\perp}^{(0)} + \frac{m}{qB^2} \mathbf{B} \times \left( \partial_t + \left( v_{\parallel} \mathbf{b} + \mathbf{v}_{\perp}^{(1)} \right) \cdot \nabla \right) \mathbf{v}_{\perp}^{(0)} \quad (3.17)$$

In the first order, the evolution of the perpendicular electric field derives from the evolution of the potential gradient  $d\mathbf{E}_{\perp}/dt = -d\nabla_{\perp}\Phi/dt$ . The full electric field is then given by:

$$\mathbf{E}_\perp = -\nabla_\perp \Phi \quad E_\parallel = -\nabla_\parallel \Phi - \partial_t A_\parallel \quad (3.18)$$

where the time variation  $\partial_t A_\parallel$  accounts for magnetic induction effects.

The separation of scales allows for fluid-drift models, where the parallel and perpendicular momentum equations are treated independently. Mikhailovskii and Tsypin[45] first described slow drift dynamics from a theoretical viewpoint in 1971 with  $\rho_L = 0$ . Hazeltine et al.[29] extended the framework to include a finite ion Larmor radius. To understand their approach, it is useful to introduce the vorticity  $\boldsymbol{\Omega} = \nabla \times \mathbf{v}$ , which measures the local rotation of a fluid element. It is a vector quantity, where the direction indicates the axis of rotation and its magnitude indicates the strength of the rotational motion. As perpendicular phenomena are essentially described by the parallel component of  $\boldsymbol{\Omega}$ , we only solve for the conservation of  $\Omega_\parallel$ . Furthermore, assuming that the electric drift dominates the perpendicular direction, we can express:

$$\Omega_\parallel = \mathbf{b} \cdot \nabla \times \mathbf{v}_E = \nabla_\perp^2 \Phi \quad (3.19)$$

Taking the curl of the perpendicular (drift) momentum balance, we obtain a conservation equation for the ion vorticity:

$$\frac{n_i m_i}{q_i B^2} (\partial_t \Omega_\parallel + (\nu_{i,\parallel} \mathbf{b} + \mathbf{v}_{i,\perp}) \cdot \nabla \Omega_\parallel) = \nabla \cdot (j_\parallel \mathbf{b} + \mathbf{j}_\perp - e n \mathbf{v}_E) \quad (3.20)$$

where the perpendicular current arises from drifts in opposite directions for electrons and ions,  $\mathbf{j}_\perp = q_i n_i \mathbf{v}_{i,\perp} - q_e n_e \mathbf{v}_{e,\perp}$ . There is a "grad B," curvature, and polarization current, but no "ExB" current, as the electric drift is independent of the species' mass and charge. The parallel current density is given by Ohm's law:

$$\eta_\parallel j_\parallel + \frac{m_e}{e} \frac{d j_\parallel}{dt} = E_\parallel + \frac{\nabla_\parallel p_e}{n_e e} + \frac{0.71}{e} \nabla_\parallel T_e \quad (3.21)$$

A full derivation of the drift-reduced equations, including all possible terms, was provided by Simakov and Catto[59]. Notably, they derived a self-consistent expression for the ion parallel and gyroviscous stress tensors, ensuring full energy conservation in the fluid model.

### 3.1.3. Linear plasma instabilities

To understand how turbulent structures appear and travel in the plasma, it is essential to understand the physical mechanisms covered by the drift-reduced equations. In this section, we delve into the different linear phenomena that appear plasma in the SOL.

### 3.1.3.1. Non-adiabatic drift waves

One key mechanism within this framework is the non-adiabatic density response to potential perturbations. In this context, resistivity induces a phase shift between density and potential perturbations, which can either amplify or dampen these perturbations. The Hasegawa-Wakatani model [27] provides a foundational understanding of this process. This model considers an isothermal plasma with an unsheared magnetic field, where particles are advected solely by the electric drift, and parallel ion motion is neglected. Perturbations on any quantity are expressed as  $X = X_0(\psi) + \tilde{X}$ , with  $\tilde{X} = e e^{-\omega t - \mathbf{k} \cdot \mathbf{x}}$ . The equilibrium fields  $X_0$  vary across flux surfaces, with an imposed gradient in the radial direction. The governing equations are:

$$\partial_t n + \mathbf{v}_E \cdot \nabla n = -\frac{1}{e} \nabla \cdot (j_{\parallel} \mathbf{b}) \quad (3.22)$$

$$\eta_{\parallel} j_{\parallel} = -\frac{T_e}{en} \nabla_{\parallel} n + \nabla \Phi \quad (3.23)$$

$$\frac{n m_i}{B^2} (\partial_t \nabla_{\perp}^2 \Phi + \mathbf{v}_E \cdot \nabla \nabla_{\perp}^2 \Phi) = -\nabla \cdot (j_{\parallel} \mathbf{b}) \quad (3.24)$$

The wavenumber vector  $\mathbf{k}$  contains both parallel and perpendicular components, such that in the Fourier space  $k_{\parallel}^2 \sim \nabla_{\parallel}^2$  and  $k_{\perp}^2 \sim \nabla_{\perp}^2$ . The dispersion relation for the system is then:

$$\omega^2 + i \frac{1 + k_{\perp}^2 \rho_L^2}{k_{\perp}^2 \rho_L^2} \frac{k_{\parallel}^2 T_e}{e^2 n_0 \eta_{\parallel}} \omega + i \frac{k_{\parallel}^2 T_e}{e^2 n_0 \eta_{\parallel} k_{\perp}^2 \rho_L^2} \frac{m_i T_e}{e n_0 a B} \partial_{\psi} n_0 = 0 \quad (3.25)$$

The solution to this system can be decomposed into a real component  $\omega_*$  that corresponds to the natural frequency of the system and an imaginary component  $\gamma$  that describes the growth or damping rate. From the drift-ordering parameters, we know that  $k_{\perp} \rho_L$  must be small, simplifying the system. The first solution is purely real, and the second is purely imaginary, with:

$$\omega_* = \frac{1}{k_{\perp}^2 \rho_L^2} \frac{m_i T_e}{e a B} \frac{\partial_{\psi} n_0}{n_0} k_{\parallel}^2 \quad \gamma = \frac{1}{k_{\perp}^2 \rho_L^2} \frac{T_e}{e^2 n_0 \eta_{\parallel}} k_{\parallel}^2 \quad (3.26)$$

The system frequency  $\omega_*$  is called the diamagnetic frequency and is driven by the density gradient. We observe that the growth rate  $\gamma$  is positive, indicating that under certain conditions, perturbations may grow indefinitely. In an ideal plasma with zero resistivity, the dispersion relation has only real solutions, and the system remains stable. In this case, the interaction is adiabatic, and density and potential oscillate in phase.

### 3.1.3.2. Sound waves

Parallel ion motion produces sound waves. If we consider only the parallel velocity, the conservation equation can be expressed in a reduced form:

$$\partial_t n + \nabla \cdot (v_{\parallel} n \mathbf{b}) = 0 \quad (3.27)$$

$$m_i n \left( \partial_t v_{\parallel} + \nabla \cdot (v_{\parallel}^2 \mathbf{b}) \right) = -\nabla_{\parallel} (p_i + p_e) \quad (3.28)$$

Density and velocity perturbations then travel in the parallel direction at the sound speed  $c_s = \sqrt{(T_e + T_i)/m_i}$ . Sound waves do not lead to instabilities nor do they grow or damp, but they naturally arise with perturbations and interact with other wave dynamics.

### 3.1.3.3. Shear Alfvén waves

Density perturbations provoke an electromagnetic response. To this effect, we consider a standard four-field model that couples the electron density  $n_e$  with the parallel current density  $j_{\parallel}$  and both potentials  $\Phi$  and  $A_{\parallel}$ . The governing equations now are:

$$\nabla \cdot \left[ \frac{m_i n_i}{B^2} \partial_t \nabla_{\perp}^2 \Phi \right] = \nabla \cdot (j_{\parallel} \mathbf{b}) \quad (3.29)$$

$$\nabla_{\perp}^2 A_{\parallel} = -\mu_0 j_{\parallel} \quad (3.30)$$

$$\eta_{\parallel} j_{\parallel} + \frac{m_e}{n_e e^2} \partial_t j_{\parallel} = \left( -\nabla_{\parallel} \Phi - \partial_t A_{\parallel} + \frac{T_e}{e} \nabla_{\parallel} \log(n_e) \right) \quad (3.31)$$

$$\partial_t n_e = \frac{1}{e} \nabla \cdot j_{\parallel} \quad (3.32)$$

Its complex dispersion relation has a real and an imaginary part indicating the appearance of a decaying wave.

$$\omega_A^2 = \left( \frac{v_A^2}{1 + \frac{m_e}{e^2 \mu_0 n_e} k_{\perp}^2} + \frac{1}{\frac{n_e \mu_0}{T_0 k_{\perp}^2} + \frac{1}{v_{th,e}^2}} \right) k_{\parallel}^2 - \frac{\eta_{\parallel}^2 k_{\perp}^4}{4 \left( \mu_0 + \frac{m_e}{e^2 n_i} k_{\perp}^2 \right)^2} \quad (3.33)$$

The dispersion relation describes "shear Alfvén waves", according to which perturbations travel along magnetic field lines. In cases with high parallel conductivity, the first term dominates the dispersion relation. We then observe that the relation describes a wave in parallel direction whose velocity is bound by the Alfvén wave speed  $v_A = \frac{B}{\sqrt{m_i n_i \mu_0}}$  for small  $k_{\perp}$  and by the thermal electron wave speed  $v_{th,e} = \sqrt{\frac{T_e}{m_e}}$  for large  $k_{\perp}$ . This is in line with the findings by Dudson et al [15] and reflects the need for electron inertia to avoid unphysically large speeds in the upper  $k_{\perp}$  limit.

### 3.1.3.4. Resistive ballooning modes

Magnetic curvature also plays an important role in the formation of drift waves. The effective gravity force opposes the pressure gradient, leading to inherent plasma instability and the development of resistive ballooning modes [28]. In the vorticity conservation equation, as given in Eq. 3.20, the term  $\nabla \cdot \mathbf{v}_\perp$  appears. Both the electric and diamagnetic drifts take the form  $(\mathbf{B} \times \nabla X)/B^2$ . In a homogeneous magnetic field, as assumed above, the divergence of the drifts vanishes. However, in a curved magnetic field, this term introduces additional coupling between the vorticity and the density and potential gradients. In a realistic tokamak configuration with both poloidal and toroidal field components and a high aspect ratio  $R/a$ , poloidal perturbations can be expressed as  $\tilde{X} = \sum_m \tilde{X}_m e^{im\theta}$ . A perturbation mode  $m$  in the density or potential is then coupled to the modes  $m - 1$  and  $m + 1$  of the other fields.

So far we have considered several wave dynamics in the plasma individually, with each their own characteristic frequency. ————— WRITE DOWN CHARACTERISTIC VALUES ————— In reality, all these modes impact the plasma simultaneously. The actual linear behavior is far more complex and combines all frequencies.

Leddy et al. [38] compared the linear behavior of drift-reduced and full-velocity descriptions of plasmas. They found that while the drift reduction suppresses fast wave dynamics, easing timestep constraints and motivating the use of reduced MHD models as introduced in Sec. 2.3.2, the linear behavior of the two approaches only agrees within a limited parameter space, generally including tokamak conditions. However, the agreement is only robust in the edge region, with significant discrepancies appearing in the core, limiting the validity of drift-reduced models in simulation that consider both sides of the separatrix.

## 3.2. Electromagnetic effects in edge plasma

One particular interaction we want to study is the impact of electromagnetic effects on edge plasma turbulence. Shear Alfvén waves have already been introduced above, however they travel at much higher speeds than drift waves. In this section, we focus more on drift-Alfvén waves, which appear with the presence of a magnetic induction term in the non-adiabatic response. We then discuss the nonlinear impact of fluctuations of the magnetic equilibrium on the plasma.

### 3.2.1. Magnetic induction

As early as 1997, Scott[56] questioned the importance of magnetic induction for the evolution of drift waves. In the electrostatic model, whose existing implementation in Soledge3X was described in the previous chapter, the parallel current density in Ohm's law balances the plasma pressure with electric forces and resistive friction. As soon as we consider a finite  $\beta$ , the variation of the electromagnetic vector potential  $\mathbf{A}$  adds to the electric potential gradient in the definition of the electric field  $\mathbf{E} = -\partial_t \mathbf{A} - \nabla \Phi$ . At

drift scales,  $k_{\parallel} \ll k_{\perp}$  and only the parallel component  $A_{\parallel} = \mathbf{A} \cdot \mathbf{b}$  of the electromagnetic potential effectively impacts electric forces. It is directly linked to the current density via Ampère's law:

$$\nabla \cdot \nabla A_{\parallel} = -\mu_0 j_{\parallel} \quad (3.34)$$

If we then include  $A_{\parallel}$  in the parallel electric field, magnetic induction leads to an extended, electromagnetic Ohm's law:

$$\partial_t A_{\parallel} + \eta_{\parallel} j_{\parallel} = -\nabla \Phi + \frac{1}{n_e e} \nabla p_{\parallel} + \frac{1}{n_e e} R_{\parallel} \quad (3.35)$$

Magnetic induction introduces drift Alfvén waves to the system with a velocity  $v_A^2 = B^2 / (m_i \mu_0 n_i)$ . Because of the interplay between Ampère's (3.34) and Ohm's (3.35) laws, the magnetic induction term quickly dominates over the parallel resistivity. This occurs as soon as the perpendicular scale exceeds the collisionless skin depth, or if  $\beta > (k_{\perp} \rho_s)^2 (m_e / m_u)$  [44]. In drift-wave turbulence the characteristic scales may be much larger than the Larmor radius, in which case electromagnetic effects are dominant even at plasmas with low  $\beta$  values of  $10^{-6}$  [56]. It is apparent that magnetic induction strongly impacts the response of the parallel current to the force balance and as such wave speeds in the plasma. For higher  $\beta$ , it essentially replaces the electric resistivity as the driver of the current response.

### 3.2.2. Electron inertia

Electron inertia effects are then needed to complete the resistive dissipation in Ohm's law. We introduce a transport term to Ohm's law on the parallel current:

$$\partial_t A_{\parallel} + \eta_{\parallel} j_{\parallel} + \frac{m_e}{e} (\partial_t + \mathbf{v}_E \cdot \nabla) j_{\parallel} = -\nabla \Phi + \frac{1}{n_e e} \nabla p_{\parallel} + \frac{1}{n_e e} R_{\parallel} \quad (3.36)$$

Dudson et al. [15] further pointed out that a uniquely resistive current response does not prevent the Alfvén velocity to exceed the speed of light. It may particularly occur in the upper  $k_{\perp}$  limit. With electron inertia the parallel transport is limited by the thermal electron speed and hence within physically realistic values.

The introduction of electromagnetic effects in Soledge3X in form of magnetic induction driven by the parallel electromagnetic potential  $A_{\parallel}$ , also requires a finite electron mass in Ohm's law to avoid unphysical speeds in the plasma and .

It was found on HSX that electron inertia effect might dominate resistivity for the generation of resistive ballooning modes [49].

### 3.2.3. Electromagnetic flutter

follow scott's derivation

### 3.3. Drift-Alfvén waves

look at Kaiyu zhang on mode shifts

#### 3.3.1. Linear analysis

#### 3.3.2. Non-linear effects

## **Part III.**

# **An Electromagnetic Model for SOLEDGE3X**

# 4. Electromagnetic effects coupled to the SOLEDGE3X framework

## 4.1. Transport equations

For simulations of the SOL in SOLEDGE3X, the mass balance in [2.10](#) and the momentum balance in [2.14](#) are used. To calculate the different drifts that compound the velocity  $\vec{u}$ , it is convenient to decompose it into a parallel component  $u_{\parallel}$  along the magnetic field lines  $\vec{b}$  and orthogonal  $\vec{u}_{\perp}$  components. We here have the relationship:

$$\vec{u} = u_{\parallel} \vec{b} + \vec{u}_{\perp} \quad \text{with} \quad u_{\parallel} = \vec{u} \cdot \vec{b} \quad \text{and} \quad \vec{u}_{\perp} = \vec{b} \times \vec{u} \quad (4.1)$$

### 4.1.1. Mass balance

The source term  $S_n$  in the mass balance [2.10](#) comes from particle collisions.

It is sufficient to solve the mass balance for ions, as the fluid density of electrons can be easily retrieved with the quasi-neutrality assumption:

$$n_e = \sum_{\alpha} Z_{\alpha} n_{\alpha} \quad (4.2)$$

### 4.1.2. Momentum balance

For the momentum balance [2.14](#), the equations splits into its parallel and perpendicular components. In parallel direction, we have a scalar equation on  $u_{\parallel}$ :

$$\partial_t (mnu_{\parallel}) + \vec{\nabla} \cdot (mnu_{\parallel} \vec{u}) = -\vec{\nabla}_{\parallel} p_{\parallel} - \pi_{\parallel} \vec{\nabla} \cdot \vec{b} + nqE_{\parallel} + S_{u_{\parallel}} \quad (4.3)$$

$$E = -\nabla\Phi$$

The stress tensor  $\tilde{\Pi}$  can be reduced to a collisional viscous term  $\tilde{\Pi}^{vis}$  and a collisionless gyroviscous term  $\tilde{\Pi}^{FLR}$ . The divergence term in [Equation 2.14](#) is:

$$\nabla \cdot \tilde{\Pi} = \nabla \cdot \tilde{\Pi}^{vis} + \nabla \cdot \tilde{\Pi}^{FLR} \quad (4.4)$$

#### 4. Electromagnetic effects coupled to the SOLEDGE3X framework – 4.1. Transport equations

with:  $\nabla \cdot \bar{\bar{\Pi}}^{vis} = \nabla \cdot \bar{\bar{\Pi}}_{\parallel} = -\frac{1}{3} \nabla \pi_{\parallel} (\nabla \cdot \pi_{\parallel} \mathbf{b}) \mathbf{b} + \pi_{\parallel} \mathbf{b} \cdot \nabla \mathbf{b}$

and:  $\nabla \cdot \bar{\bar{\Pi}}^{FLR} = -nm \mathbf{u}^* \cdot \nabla \mathbf{u} - \underbrace{[\nabla_{\perp} + 2\mathbf{b}\nabla_{\parallel}] \frac{p_{\perp}}{\omega_c} \mathbf{b} \cdot (\nabla_{\perp} \times \mathbf{u}) + \frac{p_{\perp}}{\omega_c} [\mathbf{b} \times \nabla] \nabla_{\parallel} u_{\parallel}}_{= -\mathbf{F}^{FLR}}$

In this expression, the term  $\pi_{\parallel} = p_{\parallel} - p_{\perp}$  can be calculated with the Braginski closure:

$$\pi_{\parallel} = -3\eta_0 \left( \nabla_{\parallel} \mathbf{u}_{\parallel} - \kappa \cdot \mathbf{u} - \frac{1}{3} \nabla \cdot \mathbf{u} \right) \quad (4.5)$$

with the curvature of the magnetic field  $\kappa$ :

$$\kappa = \mathbf{b} \cdot \nabla \mathbf{b}$$

For the perpendicular velocity, the equation is not straightforward anymore and requires several algebraic transformations:

$$\begin{aligned} \vec{b} \times [\partial_t (mn\vec{u}) + \vec{\nabla} \cdot (mn\vec{u} \otimes \vec{u})] &= -\vec{b} \times \vec{\nabla} p_{\perp} - \vec{b} \times \vec{\nabla} \cdot \bar{\bar{\Pi}} + nq\vec{b} \times \vec{E} \\ &\quad + nq(\vec{b} \times \vec{u} \times \vec{B}) + \vec{b} \times \vec{R} + \vec{b} \times \vec{S}_u \\ \Leftrightarrow \quad \vec{u}_{\perp} &= \frac{\vec{b} \times \vec{\nabla} p}{qnB} + \frac{\vec{b} \times \vec{\nabla} \cdot \bar{\bar{\Pi}}}{qnB} + \frac{\vec{E} \times \vec{b}}{B} - \frac{\vec{b} \times (R + S)}{qnB} \\ &\quad + \frac{\vec{b}}{qnB} \times (\partial_t (mn\vec{u}) + \vec{\nabla} \cdot (mn\vec{u} \otimes \vec{u})) \end{aligned} \quad (4.6)$$

The expression for the perpendicular velocity  $\vec{u}_{\perp}$  is not explicit as the right-hand side depends on the full velocity vector. However, we can fairly well approximate it with two calculation steps. All terms that do not depend on  $u$  are first evaluated to get  $\vec{u}_{\perp}^{(0)}$  (and with equation 4.1 we can also calculate  $\vec{u}^{(0)}$ ), and then  $\vec{u}_{\perp}^{(1)}$  is calculated by replacing every occurrence of  $\vec{u}$  by  $\vec{u}^{(0)}$ . The terms  $\vec{u}^*$ ,  $\vec{u}_E$ ,  $\vec{u}_{\perp,\Pi}$ ,  $\vec{u}_{\perp,S}$  and  $\vec{u}_p$  are respectively called diamagnetic, "E cross B", parallel viscous stress, friction force and polarization drifts.

$$\vec{u}_{\perp}^{(0)} = \frac{\vec{b} \times \vec{\nabla} p}{qnB} + \frac{\vec{E} \times \vec{b}}{B} = \vec{u}^* + \vec{u}_E \quad (4.7)$$

$$\begin{aligned} \vec{u}_{\perp}^{(1)} &= \frac{\vec{b} \times \vec{\nabla} \cdot \bar{\bar{\Pi}}(\vec{u}^{(0)})}{qnB} - \frac{\vec{b} \times (R(\vec{u}^{(0)}) + S(\vec{u}^{(0)}))}{qnB} \\ &\quad + \frac{\vec{b}}{n\omega_c} \times (\partial_t (n\vec{u}^{(0)}) + \vec{\nabla} \cdot (n\vec{u}^{(0)} \otimes \vec{u}^{(0)})) \\ &= \vec{u}_{\perp,\Pi} + \vec{u}_{\perp,S} + \vec{u}_p \end{aligned} \quad (4.8)$$

$$\vec{u}_{\perp} \approx \vec{u}_{\perp}^{(0)} + \vec{u}_{\perp}^{(1)} \quad (4.9)$$

This simplification holds because the contribution of  $\vec{u}_\perp^{(1)}$  is small, of the order of  $\tau_c/\tau_{ad}$  or  $\tau_c/\tau_{coll}$ . Next, let us extract the divergence free contribution from the diamagnetic flux  $n\tilde{\vec{u}}^*$ .

$$n\tilde{\vec{u}}^* = -\nabla \times \frac{p_\perp \vec{B}}{qB^2} + n\tilde{\vec{u}}^*$$

with:  $\tilde{\vec{u}}^* = \frac{2T_\perp \vec{B} \times \vec{\nabla}B}{qB^3} + \frac{T_\perp}{qB^2} \nabla \times \vec{B}$

(4.10)

The second term in  $\tilde{\vec{u}}^*$  is usually very small and can be neglected if magnetic fields do not fluctuate.

The last term  $u_p$  in [Equation 4.8](#) is called the polarization drift. A simple expression for the associated flux can be found through algebraic manipulations and neglecting some small curvature terms.

$$n\vec{u}_p = \partial_t \vec{\omega} - \vec{\nabla} \cdot (\tilde{\vec{u}}^{(0)} \otimes \vec{\omega})$$

with:  $\vec{\omega} = \frac{m}{qB^2} \left( n\vec{\nabla}_\perp \Phi + \frac{1}{q} \nabla_\perp \left( p - \frac{\pi_\parallel}{3} \right) \right) - \frac{m}{q^2 B^2} S_{u_\perp}$

(4.11)

The electric potential in the plasma appears here in the variable  $\Phi$  and is a new unknown that needs to be solved for.

### 4.1.3. Charge balance

To complete the system, a last equation on the charge balance is needed. Because of the quasineutrality assumption the volume charge is assumed to be 0 and the governing equation is:

$$\vec{\nabla} \cdot \vec{j} = 0$$

The total current is due to charge transport by plasma species. It is hence calculated as:

$$\vec{j} = \sum_{\alpha \in \{i, e\}} q_\alpha n_\alpha \vec{u}_\alpha$$
(4.12)

As the current is directly linked to the plasma species transport, it is decomposed into the same terms as the velocities in equations [4.7](#) and [4.8](#). The "E cross B" drift is the same for all species therefore its contribution to the current vanishes with the quasineutrality assumption. The current from the friction force drift is mostly due to collision with neutral species and denoted by  $\vec{j}_c$ . Neglecting curvature terms, we can derive an expression for the perpendicular polarization current from [Equation 4.11](#).

$$\vec{j}_p = -\partial_t \vec{\omega}_s - \sum_{\alpha \neq e} q_\alpha \vec{\nabla} \cdot (\tilde{\vec{u}}_\alpha^{(0)} \otimes \vec{\omega}_\alpha)$$

with:  $\vec{\omega}_s = \sum_{\alpha \neq e} q_\alpha \vec{\omega}_\alpha$

(4.13)

#### 4. Electromagnetic effects coupled to the SOLEDGE3X framework – 4.1. Transport equations

The problem is not solved on  $\vec{j}$  itself but on the vorticity defined as  $\Omega = \vec{\nabla} \cdot \vec{\omega}_s$  which gives the expression on  $\vec{j}_p$ :

$$\vec{\nabla} \cdot \vec{j}_p = -\partial_t \Omega + \vec{\nabla} \cdot \sum_{\alpha \neq e} q_\alpha \vec{\nabla} \cdot (\tilde{u}_\alpha^{(0)} \otimes \vec{\omega}_\alpha) = -\partial_t \Omega + \vec{\nabla} \cdot \vec{j}_\Omega$$

The divergence of the total current can then be transformed into a transport equation on the vorticity:

$$\begin{aligned} & \vec{\nabla} \cdot \vec{j} = 0 \\ \Leftrightarrow & -\vec{\nabla} \cdot \vec{j}_p = \vec{\nabla} \cdot (j_{\parallel} \vec{b} + \vec{j}^* + \vec{j}_{\perp,\Pi} + \vec{j}_c) \\ \Leftrightarrow & \partial_t \Omega = \vec{\nabla} \cdot \sum_{\alpha \neq e} q_\alpha \vec{\nabla} \cdot (\tilde{u}_\alpha^{(0)} \otimes \vec{\omega}_\alpha) + \vec{\nabla} \cdot (j_{\parallel} \vec{b} + \vec{j}^* + \vec{j}_{\perp,\Pi} + \vec{j}_c) \end{aligned} \quad (4.14)$$

If this equation is combined with [Equation 4.11](#) we get :

$$\begin{aligned} \vec{\omega} &= \frac{m}{qB^2} \left( n \vec{\nabla}_\perp \Phi + \frac{1}{q} \nabla_\perp \left( p - \frac{\pi_{\parallel}}{3} \right) \right) - \frac{m}{q^2 B^2} \vec{S}_{u_\perp} \\ \Leftrightarrow \sum_{\alpha \neq e} q_\alpha \vec{\omega}_\alpha &= \sum_{\alpha \neq e} q_\alpha \left[ \frac{m_\alpha}{q_\alpha B^2} \left( n_\alpha \vec{\nabla}_\perp \Phi + \frac{1}{q_\alpha} \nabla_\perp \left( p - \frac{\pi_{\parallel}}{3} \right) \right) - \frac{m_\alpha}{q_\alpha^2 B^2} \vec{S}_{u_{\alpha\perp}} \right] \\ \Leftrightarrow \Omega &= \vec{\nabla} \cdot \sum_{\alpha \neq e} \left[ \frac{m_\alpha}{B^2} \left( n_\alpha \vec{\nabla}_\perp \Phi + \nabla_\perp \left( p - \frac{\pi_{\parallel}}{3} \right) \right) - \frac{m_\alpha}{q_\alpha B^2} \vec{S}_{u_{\alpha\perp}} \right] \\ \Leftrightarrow \partial_t \vec{\Omega} &= \vec{\nabla} \cdot \left[ \frac{m_\alpha n_\alpha}{B^2} \partial_t \vec{\nabla}_\perp \Phi \right] + \partial_t \Omega_\pi \\ \Leftrightarrow \vec{\nabla} \cdot \left[ \frac{m_\alpha n_\alpha}{B^2} \partial_t \vec{\nabla}_\perp \Phi \right] &= \vec{\nabla} \cdot (j_{\parallel} \vec{b} + \vec{j}^* + \vec{j}_{\perp,\Pi} + \vec{j}_c + \vec{j}_\Omega) - \partial_t \Omega_\pi \end{aligned} \quad (4.15)$$

In this calculation we used the Boussinesq approximation and the Einstein summation over the ion index  $\alpha$  allows for a more compact expression. The vorticity source term  $\Omega_\pi$  is given by a perpendicular diffusion on the product of ion density and temperature:

$$\Omega_\pi = \vec{\nabla} \cdot \sum_{\alpha \neq e} \left( \frac{m_\alpha}{q_\alpha B^2} \vec{\nabla}_\perp [n_\alpha T_\alpha] \right)$$

The parallel current density is calculated from the generalized Ohm's law neglecting the electron mass and using Spitzer-Härm resistivity  $\eta_{\parallel}$  [[60](#)]:

$$j_{\parallel} = \sigma_{\parallel} \left( E_{\parallel} + \frac{\vec{\nabla}_{\parallel} p_e}{n_e e} + \frac{0.71}{e} \vec{\nabla}_{\parallel} T_e \right) \quad \text{with:} \quad \sigma_{\parallel} = 1/\eta_{\parallel} \approx \frac{T_e^{1.5}}{5 \cdot 10^{-5} \log \Lambda} \quad (4.16)$$

For now, we assume a static magnetic field and define the parallel electric field as the negative gradient of the electrostatic potential in parallel direction  $E_{\parallel} = -\vec{\nabla}_{\parallel} \Phi$ . We can further assume that the pressure  $p_e = n_e T_e$  is static. We then get:

$$\frac{1}{n_e} \vec{\nabla}_{\parallel} p_e = T_e \vec{\nabla}_{\parallel} \log(n_e) + \vec{\nabla}_{\parallel} T_e$$

If we now inject Equation 4.16 into the vorticity equation Equation 4.15, we obtain:

$$\vec{\nabla} \cdot \left[ \frac{m_\alpha n_\alpha}{B^2} \partial_t \vec{\nabla}_\perp \Phi \right] = \vec{\nabla} \cdot \left[ -\sigma_\parallel \vec{\nabla}_\parallel \Phi + \frac{\sigma_\parallel T_e}{e} \vec{\nabla}_\parallel \log(n_e) + \frac{1.71 \sigma_\parallel}{e} \vec{\nabla}_\parallel T_e \right] \vec{b} + F_\Omega \quad (4.17)$$

where  $F_\Omega = (\vec{j}^* + \vec{j}_{\perp,\Pi} + \vec{j}_c + \vec{j}_\Omega) - \partial_t \Omega_\pi$  contains all generic right-hand side terms.

## 4.2. Electromagnetic Model in SOLEDGE3X

### 4.2.1. Electron Inertia

As we have seen in ..., the bad condition number of the vorticity equation has its roots in the combined perpendicular and parallel diffusion on the electric potential. One attempt to ameliorate the situation would be to split these terms in a way that their respective discrete operators are not applied on the same unknown in the vorticity matrix. To express the system in such a way, it is convenient to include the parallel current  $j_\parallel$  as a separate variable in the system. In the definition of the parallel current density Equation 4.16, we omitted the effects of electron inertia in the generalized Ohm's law. Its full expression states:

$$j_\parallel = \sigma_\parallel \left( E_\parallel + \frac{\vec{\nabla}_\parallel p_e}{n_e e} + \frac{0.71}{e} \vec{\nabla}_\parallel T_e + \frac{m_e}{e} \frac{\partial u_{\parallel,e}}{\partial t} \right)$$

We start with the parallel momentum conservation equations for electrons 4.18 and ions 4.19.

$$\partial_t (m_e n_e u_{\parallel,e}) + \nabla \cdot (m_e n_e u_{\parallel,e} \vec{u}_e) = -\nabla_\parallel p_e - e n_e E_\parallel - \vec{b} \cdot \nabla \cdot \bar{\bar{\Pi}}_{\parallel,e} + R_{\parallel,e} + S_{\Gamma,\parallel,e} \quad (4.18)$$

$$\partial_t (m_i n_i u_{\parallel,i}) + \nabla \cdot (m_i n_i u_{\parallel,i} \vec{u}_i) = -\nabla_\parallel p_i + Z_i e n_i E_\parallel - \vec{b} \cdot \nabla \cdot \bar{\bar{\Pi}}_{\parallel,i} + R_{\parallel,i} + S_{\Gamma,\parallel,i} \quad (4.19)$$

Next we multiply the equation for the electrons by  $e/m_e$  and the equation for ions  $-Z_i e/m_i$ . and then we take the sum over all species (electrons and all different ions). For now we ignore the source terms, omit the momentum fluxes under the quasi-neutrality assumption  $n_e = \sum_{\alpha \in i} Z_\alpha n_\alpha$  and because the very small ratio  $m_e/m_i$  we also neglect the ionic right-hand side terms for which the factor  $1/m_i$  does not cancel out.

$$\partial_t \left( e n_e u_{\parallel,e} - \sum_{\alpha \in i} Z_\alpha e n_\alpha u_{\parallel,\alpha} \right) = -\frac{e}{m_e} \nabla_\parallel p_e - \frac{e^2 n_e}{m_e} E_\parallel - \frac{e}{m_e} \vec{b} \cdot \nabla \cdot \bar{\bar{\Pi}}_{\parallel,e} + \sum_{\alpha \in i} \frac{Z_\alpha e}{m_\alpha} \vec{b} \cdot \nabla \cdot \bar{\bar{\Pi}}_{\parallel,\alpha} + \frac{e}{m_e} R_{\parallel,e} - \sum_{\alpha \in i} \frac{Z_\alpha e}{m_\alpha} R_{\parallel,\alpha}$$

#### 4. Electromagnetic effects coupled to the SOLEDGE3X framework – 4.2. Electromagnetic Model in SOLEDGE3X

The friction terms  $R_{\parallel,\alpha}$  between all species are computed with the multi-species Zhdanov closure:

$$\frac{1}{m_e} R_{\parallel,e} - \sum_{\alpha \in i} \frac{Z_\alpha}{m_\alpha} R_{\parallel,\alpha} = \frac{n_e}{m_e} \left[ \eta_\parallel e^2 \left( \sum_{\alpha \in i} Z_\alpha n_\alpha u_{\parallel,\alpha} - n_e u_{\parallel,e} \right) - 0.71 \nabla_\parallel T_e \right]$$

If we further use the definition of the parallel current density  $j_\parallel = \sum_{\alpha \in \{i,e\}} q_\alpha n_\alpha u_{\parallel,\alpha}$  the above equation can be expressed in terms of  $j_\parallel$ :

$$-\partial_t j_\parallel = -\frac{e}{m_e} \nabla_\parallel p_e - \frac{e^2 n_e}{m_e} E_\parallel - \frac{e}{m_e} \vec{b} \cdot \nabla \cdot \bar{\Pi}_{\parallel,e} + \sum_{\alpha \in i} \frac{Z_\alpha e}{m_\alpha} \vec{b} \cdot \nabla \cdot \bar{\Pi}_{\parallel,\alpha} + \frac{e^2 n_e}{m_e} \eta_\parallel j_\parallel - \frac{e n_e}{m_e} 0.71 \nabla_\parallel T_e$$

For the stress tensors  $\bar{\Pi}_{\parallel,*}$  it is numerically important to keep the anomalous perpendicular viscosity to ensure a coherence for  $j_\parallel$ . This term is then given by

$$\vec{b} \cdot \nabla \cdot \bar{\Pi}_{\perp,*} = \nabla \cdot (n_* v_* \nabla_\perp m_* u_{\parallel,*})$$

Since we are solving the equation on  $j_\parallel$  we can express any electron velocity by

$$u_{\parallel,e} = \sum_{\alpha \in i} \frac{Z_\alpha n_\alpha}{n_e} u_{\parallel,\alpha} - \frac{1}{e n_e} j_\parallel$$

and consequently the electronic viscous stress term becomes

$$\begin{aligned} \vec{b} \cdot \nabla \cdot \bar{\Pi}_{\perp,e} &= m_e \nabla \cdot \left( n_e v_e \nabla_\perp \left[ \sum_{\alpha \in i} \frac{Z_\alpha n_\alpha}{n_e} u_{\parallel,\alpha} - \frac{1}{e n_e} j_\parallel \right] \right) \\ &\approx m_e \sum_{\alpha \in i} Z_\alpha \vec{\nabla} \cdot (v_e \vec{\nabla}_\perp n_\alpha u_{\parallel,\alpha}) - \frac{m_e}{e} \nabla \cdot (v_e \nabla_\perp j_\parallel) \end{aligned}$$

For the sake of better readability, we define a variable

$$D_{\perp,u_i} = \frac{m_e}{n_e e} \sum_{\alpha \in i} Z_\alpha [\nabla \cdot ((v_\alpha - v_e) \nabla_\perp n_\alpha u_{\parallel,\alpha})]$$

that bundles the perpendicular diffusion of ionic momentum. It may be noted that if the electronic and ionic viscosities match, this diffusion term vanishes. If we now combine all elements and apply some algebraic transformations we obtain the generalized Ohm's law with electron inertia:

$$j_\parallel + \frac{\sigma_\parallel m_e}{n_e e^2} \left( \frac{\partial j_\parallel}{\partial t} - \vec{\nabla} \cdot (v_e \vec{\nabla}_\perp j_\parallel) \right) = \sigma_\parallel \left( E_\parallel + \frac{\vec{\nabla}_\parallel p_e}{n_e e} + \frac{0.71}{e} \vec{\nabla}_\parallel T_e + D_{\perp,u_i} \right) \quad (4.20)$$

The vorticity equation [Equation 4.14](#) needs to be written as a system of equations on the potential  $\Phi$  and the parallel current density  $j_\parallel$ .

$$\begin{cases} \vec{\nabla} \cdot \left[ \frac{m_a n_a}{B^2} \partial_t \vec{\nabla}_\perp \Phi \right] - \vec{\nabla} \cdot [j_\parallel \vec{b}] = -\partial_t \Omega_\pi \\ j_\parallel + \frac{\sigma_\parallel m_e}{n_e e^2} (\partial_t j_\parallel - \vec{\nabla} \cdot (\nu_e \vec{\nabla}_\perp j_\parallel)) + \sigma_\parallel \vec{\nabla}_\parallel \Phi = \sigma_\parallel \left( \frac{T_e}{e} \vec{\nabla}_\parallel \log(n_e) + \frac{1.71}{e} \vec{\nabla}_\parallel T_e + \frac{0.71}{e} \vec{\nabla}_\parallel T_e + D_{\perp, u_i} \right) \end{cases} \quad (4.21)$$

We now remain with a single perpendicular Laplacian on  $\Phi$ , whereas the parallel Laplacian appears as a gradient in the equation on  $j_\parallel$  succeeded by a divergence. It may be noted that it is not necessary to include electron inertia to split the two anisotropic Laplacians. If we still assume that the electron mass is neglectable, this system essentially takes the form of a Hessenberg index-1 DAE where  $j_\parallel$  is the algebraic variable —cite—. However such systems tend to be numerically hard to solve and one common approach —cite— is to replace the zero-side side of the algebraic equation by the time derivative of the algebraic variable with a small coefficient, which effectively transforms the system into a (stiff) ODE. Exactly this has been done in the new formulation of [Equation 4.21](#) with the further benefit that the  $j_\parallel$  has a physical meaning.

## 4.2.2. Electromagnetic Induction

In a more general setting, fluctuations in the magnetic field require taking into account the change of the magnetic vector potential  $\vec{A}$  linked to the magnetic field by  $\nabla \times \vec{A} = \vec{B}$ . This new quantity appears in the definition of the parallel electric field, which then depends on the change of  $A$  over time:

$$E_\parallel = -\nabla_\parallel \Phi - \partial_t A_\parallel \quad (4.22)$$

This field appears in the definition of the parallel current [4.16](#), which in turn is member of the vorticity equation [4.14](#). With the Coulomb gauge,  $j_\parallel$  is directly proportional to the perpendicular diffusion of  $A_\parallel$ :

$$\Delta_\perp A_\parallel = -\mu_0 j_\parallel \quad (4.23)$$

The electric potential  $\Phi$  is thus implicitly linked to  $j_\parallel$  and  $A_\parallel$  and all three unknowns need to be solved in one common system. To summarize, the new set of equations reads:

$$\nabla \cdot \left[ \frac{m_a n_a}{B^2} \partial_t \nabla_\perp \Phi \right] = \nabla \cdot (j_\parallel \vec{b}) - \partial_t \Omega_\pi \quad (4.24)$$

$$j_\parallel = \sigma_\parallel \left( -\nabla_\parallel \Phi - \partial_t A_\parallel + \frac{T_e}{e} \nabla_\parallel \log(n_e) + \frac{1.71}{e} \nabla_\parallel T_e \right) \quad (4.25)$$

$$\Delta_\perp A_\parallel = -\mu_0 j_\parallel \quad (4.26)$$

The equation [4.25](#) on the intermediate variable  $j_\parallel$  can be eliminated to obtain a

system of equations only on  $\Phi$  and  $A_{\parallel}$ :

$$\begin{cases} \nabla \cdot \left[ \frac{m_\alpha n_\alpha}{B^2} \partial_t \nabla_{\perp} \Phi \right] = \nabla \cdot \sigma_{\parallel} \left( -\nabla_{\parallel} \Phi - \partial_t A_{\parallel} + \frac{T_e}{e} \nabla_{\parallel} \log(n_e) + \frac{1.71}{e} \nabla_{\parallel} T_e \right) \vec{b} - \partial_t \Omega_{\pi} \\ \Delta_{\perp} A_{\parallel} = -\mu_0 \sigma_{\parallel} \left( -\nabla_{\parallel} \Phi - \partial_t A_{\parallel} + \frac{T_e}{e} \nabla_{\parallel} \log(n_e) + \frac{1.71}{e} \nabla_{\parallel} T_e \right) \end{cases} \quad (4.27)$$

These equations use Ohm's law without the electron inertia term introduced in [subsection 4.2.1](#). It is obviously possible to include the temporal change and perpendicular diffusion of  $j_{\parallel}$  in the electromagnetic equations and it is recommended to do so. To allow for maximal flexibility, any combination of  $\Phi$  with  $A_{\parallel}$  and/or  $j_{\parallel}$  can be used and we will discuss each of these combinations.

### 4.2.3. Electromagnetic Flutter

Due to the strong anisotropy in tokamaks, most edge turbulence codes rely on alignment to the magnetic equilibrium (see discussion in Ref.[55]). However, as mentioned in Sec. ??, in the electromagnetic model, small perturbations of  $\mathbf{B}_{eq}$  can exist driven by fluctuations of  $A_{\parallel}$  such as  $\tilde{\mathbf{B}} = \nabla \times (\tilde{A}_{\parallel} \mathbf{b})$ . Therefore, these fluctuations of  $A_{\parallel}$  have to be estimated and  $A_{\parallel}$  cannot be used directly. Indeed, the diamagnetic current induced by the evolution of the full plasma pressure is balanced by a stationary background parallel current, the Pfirsch-Schlüter current, which induces a stationary part of significant amplitude in  $A_{\parallel}$  through Ampere's law (Eq. ??). This latter is denoted  $A_{\parallel,0}$ , and corresponds to the Grad-Shafranov shift due to Pfirsch-Schlüter currents that are accounted for in the parallel current. This shift  $A_{\parallel,0}$  is obviously accounted for in  $B_{eq}$ , and therefore it has to be subtracted from  $A_{\parallel}$  in nonlinear parallel operators. This is done in this work by simply removing the toroidal average as proposed by Ref.[21] in the GBS code:

$$\tilde{A}_{\parallel} = A_{\parallel} - \langle A_{\parallel} \rangle_{\varphi} \quad (4.28)$$

Therefore, the flutter is computed as follows:

$$\nabla \times (\mathbf{A}_{\parallel,0} + \tilde{A}_{\parallel} \mathbf{b}_{eq}) = \mathbf{B}_{eq} + \tilde{\mathbf{B}} \quad (4.29)$$

This leads to:

$$\tilde{\mathbf{b}} = -\frac{\mathbf{b}_{eq} \times \nabla \tilde{A}_{\parallel}}{\|\mathbf{B}\|} + \frac{\tilde{A}_{\parallel} \nabla \times \mathbf{b}_{eq}}{\|\mathbf{B}\|} \quad (4.30)$$

The gradient  $\nabla \tilde{A}_{\parallel}$  scales with the characteristic turbulent length  $1/L_{\perp}$  and the curl  $\nabla \times \mathbf{b}$  with the machine dimension  $1/a$ . Therefore,  $\frac{\mathbf{b}_{eq} \times \nabla \tilde{A}_{\parallel}}{\|\mathbf{B}\|}$  is the main contributor to the flutter field.

The perturbed magnetic unit field  $\tilde{\mathbf{b}}$  is calculated at the beginning of each timestep and added to the equilibrium unit vector  $\mathbf{b}_{eq}$ . The complete vector  $\mathbf{b} = \mathbf{b}_{eq} + \tilde{\mathbf{b}}$  is then used in all parallel advection, gradient, and diffusion terms. Since we base our calculations on plasma fields from the previous timestep, this perturbation can be seen as an additional first-order drift in the equations.

Note that Hager et al. [26] have suggested an additional time-averaged  $\langle A_{\parallel} \rangle_{\varphi,t}$  to evaluate fluctuations in the parallel electromagnetic potential, arguing that turbulent structures might appear at the same position on all poloidal planes and should therefore not be removed in the flutter calculation. This approach has been used in recent work in the GRILLIX code [71], but was not adopted in the present work, as it was estimated that the gain in accuracy did not compensate for the additional computation and memory costs.

## 4.3. Boundary conditions

Boundary conditions are required at the tokamak wall and at the core edge boundary. They need to be defined in both parallel and perpendicular directions to the magnetic field lines.

- In the perpendicular direction, zero Neumann boundary conditions for all plasma variables, i.e.,  $\partial_{\perp}(\cdot) = 0$ , are imposed both at the wall and the core edge boundary except for the electromagnetic potential, which is fixed to  $A_{\parallel} = 0$  at the two radial boundaries.
- In the parallel direction, boundary conditions are derived from the generalized Bohm-Chodura sheath boundary conditions [61]. They model the physics of the sheath located next to the limiter wall, where many assumptions used to derive the fluid models (quasi-neutrality, drift-ordering) are no longer valid. They can be expressed as:

- $|\mathbf{v} \cdot \mathbf{n}_{wall}| \geq |c_s \mathbf{b} \cdot \mathbf{n}_{wall}|$  with  $\mathbf{n}_{wall}$  being the outward normal to the wall, meaning that the outgoing velocity normal to the wall is larger than the parallel sound speed normal to the wall. This property guarantees that the total plasma velocity is oriented outward.
- $\phi_{\mathcal{E},se} = \gamma T \phi_{n,se}$ . For each species,  $\phi_{\mathcal{E},se}$  is the total energy flux at the sheath entrance,  $\phi_{n,se}$  is the particle flux at the sheath entrance, and  $\gamma$  is the sheath transmission factor equal to 2.5 for ions and 4.5 for electrons.
- $j_{wall} = \left[1 - \exp\left(\Lambda - \frac{\phi}{T_e}\right)\right] \phi_{n,se}$  is the total plasma current on the wall. The ion saturation current is computed from ion particle fluxes  $\phi_{n,se}$ , and  $\Lambda$  denotes the normalized potential drop in the sheath with  $\Lambda \sim 3$ .

- $A_{\parallel} = 0$  at the magnetic pre-sheath entrance.

## 4.4. Dimensionless fields

To increase the numerical accuracy, the code solves the equation for dedimensionalized physical quantities. It means that each variable  $X$  is scaled by a factor  $X_0$  to obtain a dedimensionalized  $\hat{X} = X/X_0$ , where  $X_0$  is representative for the range of values of  $X$ . Therefore, all quantities  $\hat{X}$  have similar values and we can prevent some numerical issues that might occur in equations containing variables with radically different orders of magnitude.

For the terms in [Equation 4.17](#), some reference values, such as the reference magnetic field  $B_0$  or the reference density  $n_0$  depend on the simulation settings and geometry and need to be specified by the user. Masses are expressed as factors of the atomic unit mass  $m_u$  and the reference electric potential  $\Phi_0$  is set equal to the user-specified reference temperature  $T_0$ . In this context, it is important to remember that temperatures are always expressed as energies in units of electronvolts [eV]. Furthermore, the spatial and temporal differential operators also need to be dedimensionalized, for which we use the cyclotronic time  $\tau_0$  and the Larmor radius  $\rho_0$ :

$$\begin{aligned}\tau_0 &= \frac{m_u}{eB_0} \\ \rho_0 &= c_0 \tau_0 \quad \text{with the reference thermal speed } c_0 = \sqrt{\frac{eT_0}{m_u}} \\ \rho_0^2 &= \frac{T_0 m_u}{eB_0^2}\end{aligned}$$

To this, a dedimensionalized version of the Spitzer conductivity  $\sigma_{\parallel}$  may be defined and the temperature  $T$  [in eV] shall be homogeneous to the electric potential:

$$\sigma_{\parallel}^0 = en_0/B_0 \quad T_0 = \Phi_0$$

. With these additional reference values, a dedimensionalized form of the vorticity equation [4.17](#) reads:

$$\begin{aligned}\hat{\nabla} \cdot \left[ \frac{m_u n_0 \Phi_0}{\tau_0 B_0^2 \rho_0^2} \frac{\hat{m}_{\alpha} \hat{n}_{\alpha}}{\hat{B}^2} \hat{\partial}_t \hat{\nabla}_{\perp} \hat{\Phi} \right] &= \hat{\nabla} \cdot \left[ \sigma_{\parallel}^0 \hat{\sigma}_{\parallel} \left( \frac{-\Phi_0}{\rho_0^2} \hat{\nabla}_{\parallel} \hat{\Phi} + \frac{T_0 \hat{T}_e}{\rho_0^2 e} \hat{\nabla}_{\parallel} \log(\hat{n}_e) + \frac{T_0}{\rho_0^2 e} 1.71 \hat{\nabla}_{\parallel} \hat{T}_e \right) \vec{b} \right] + F_{\Omega} \\ \Rightarrow \quad \hat{\nabla} \cdot \left[ \frac{\hat{m}_{\alpha} \hat{n}_{\alpha}}{\hat{B}^2} \hat{\partial}_t \hat{\nabla}_{\perp} \hat{\Phi} \right] &= \hat{\nabla} \cdot \left[ \hat{\sigma}_{\parallel} \left( -\hat{\nabla}_{\parallel} \hat{\Phi} + \hat{T}_e \hat{\nabla}_{\parallel} \log(\hat{n}_e) + 1.71 \hat{\nabla}_{\parallel} \hat{T}_e \right) \vec{b} \right] + \hat{F}_{\Omega}\end{aligned}\tag{4.31}$$

As for all other physical quantities, the newly introduced fields  $A_{\parallel}$  and  $j_{\parallel}$  are replaced by dedimensionalized quantities in the code. The electromagnetic equations from

the previous section are thus reformulated to be in concordance with the general S3X model.

First of all we need to define two constants  $A_{\parallel}^0$  and  $j_{\parallel}^0$  so that the dedimensionalized quantities  $\hat{A}_{\parallel}$  and  $\hat{j}_{\parallel}$  have about the same magnitude as the existing fields:

$$\hat{A}_{\parallel} = A_{\parallel}/A_{\parallel}^0 \quad \hat{j}_{\parallel} = j_{\parallel}/j_{\parallel}^0$$

If we plug the dedimensionalized left-hand side of [Equation 4.31](#) into the new [Equation 4.24](#), an expression for  $j_{\parallel}^0$  can be derived:

$$\begin{aligned} \hat{\nabla} \cdot \left[ \frac{m_u n_0 \Phi_0}{\tau_0 B_0^2 \rho_0^2} \frac{\hat{m}_\alpha \hat{n}_\alpha}{\hat{B}^2} \hat{\partial}_t \hat{\nabla}_\perp \hat{\Phi} \right] &= \hat{\nabla} \cdot \left[ \frac{j_{\parallel}^0}{\rho_0} \hat{j}_{\parallel} \vec{b} \right] + \partial_t \Omega_\pi \\ \Rightarrow \quad j_{\parallel}^0 &= \frac{m_u n_0 \Phi_0}{\tau_0 B_0^2 \rho_0} = e n_0 c_0 \end{aligned}$$

To define  $A_{\parallel}^0$ , there are essentially two different possibilities: the first option relies on the revised definition of the parallel electric field in [Equation 4.22](#) and states that  $\partial_t A_{\parallel}$  is homogeneous to  $\nabla \Phi$ . This yields to:

$$\frac{A_{\parallel}^{0(1)}}{\tau_0} = \frac{\Phi_0}{\rho_0} \quad \Leftrightarrow \quad A_{\parallel}^{0(1)} = \frac{\Phi_0 \tau_0}{\rho_0} \quad (4.32)$$

The second option originates in [Equation 4.26](#) and compels  $A_{\parallel}^{0(2)}$  to depend on the magnetic permeability  $\mu_0$  and the reference parallel current  $j_{\parallel}^0$ .

$$\frac{A_{\parallel}^{0(2)}}{\rho_0^2} = \mu_0 j_{\parallel}^0 \quad \Leftrightarrow \quad A_{\parallel}^{0(2)} = \mu_0 e n_0 c_0 \rho_0^2 \quad (4.33)$$

With the reference values for a typical plasma (cf. —), both variants are valid and differ by a factor

$$\frac{A_{\parallel}^{0(1)}}{A_{\parallel}^{0(2)}} = \frac{\Phi_0 \tau_0}{\mu_0 e n_0 c_0 \rho_0^3} \approx 5 \cdot 10^3$$

and are thus three orders of magnitude away. From a numerical point of view, this should not make any noticeable difference and the second option is chosen out of convenience for the implementation. In the first line of [Equation 4.27](#), the temporal variation of  $A_{\parallel}$  needs to be scaled in order to be homogeneous to the remaining terms in [Equation 4.31](#). We thus look for a factor  $\xi$  that produces the following equality:

$$\xi \frac{\Phi_0 \sigma_{\parallel}^0}{\rho_0^2} = \frac{A_{\parallel}^0 \sigma_{\parallel}^0}{\tau_0 \rho_0} \quad \Leftrightarrow \quad \xi = \frac{1}{2} \beta_0$$

where the reference plasma parameter  $\beta_0$  is the ratio between reference plasma and

4. Electromagnetic effects coupled to the SOLEDGE3X framework – 4.5. Expressing the electromagnetic vorticity equation in matrix form

magnetic pressures:

$$\beta_0 = \frac{n_0 T_0}{B_0^2 / 2\mu_0}$$

## 4.5. Expressing the electromagnetic vorticity equation in matrix form

### 4.5.1. Vorticity system with electron inertia

The generalized Ohm's law with electron inertia [Equation 4.20](#) is dedimensionalized by the reference current density  $j_{\parallel}^0$ :

$$\begin{aligned} j_{\parallel}^0 \hat{j}_{\parallel} + \frac{j_{\parallel}^0 \sigma_{\parallel}^0 m_e}{n_0 \hat{n} e^2 \tau_0} \hat{\sigma}_{\parallel} (\hat{\partial}_t \hat{j}_{\parallel} - \hat{\nabla} \cdot (\hat{v}_e \hat{\nabla}_{\perp} \hat{j}_{\parallel})) &= \frac{\sigma_{\parallel}^0}{\rho_0} \hat{\sigma}_{\parallel} \left( -\Phi_0 \hat{\nabla}_{\parallel} \hat{\Phi} + T_0 \hat{T}_e \hat{\nabla}_{\parallel} \log(\hat{n}_e) + T_0 1.71 \hat{\nabla}_{\parallel} \hat{T}_e + \frac{\rho_0 n_0 m_e}{\tau_0 e} \hat{D}_{\perp, u_i} \right) \\ \Leftrightarrow \quad \hat{j}_{\parallel} + \frac{m_e \hat{\sigma}_{\parallel}}{m_u \hat{n}} \hat{\partial}_t \hat{j}_{\parallel} &= \hat{\sigma}_{\parallel} \left( -\hat{\nabla}_{\parallel} \hat{\Phi} + \hat{T}_e \hat{\nabla}_{\parallel} \log(\hat{n}_e) + 1.71 \hat{\nabla}_{\parallel} \hat{T}_e + \frac{m_e}{m_u} \hat{D}_{\perp, u_i} \right) \end{aligned}$$

The unit mass  $m_u$  appears here from the definition of the reference parameters in [??](#) from where we easily derive  $m_u = e B_0 \tau_0$ . The factor  $m_e/m_u \approx 10^{-4}$  indicates that the impact of the term  $\partial_t j_{\parallel}$  on Ohm's law is relatively small, however it is large enough to affect the solving properties of the vorticity matrix especially when the timestep size is significantly shorter than the cyclotronic time  $\tau_0$ . The new dedimensionalized vorticity system reads:

$$\begin{cases} \hat{\nabla} \cdot \left[ \frac{\hat{m}_a \hat{n}_a}{\hat{B}^2} \hat{\partial}_t \hat{\nabla}_{\perp} \hat{\Phi} \right] - \hat{\nabla} \cdot \left[ \hat{j}_{\parallel} \vec{b} \right] &= -\hat{\partial}_t \hat{\Omega}_{\pi} \\ \hat{j}_{\parallel} + \frac{m_e \hat{\sigma}_{\parallel}}{m_u \hat{n}} (\hat{\partial}_t \hat{j}_{\parallel} - \hat{\nabla} \cdot (\hat{v}_e \hat{\nabla}_{\perp} \hat{j}_{\parallel})) + \hat{\sigma}_{\parallel} \hat{\nabla}_{\parallel} \hat{\Phi} &= \hat{\sigma}_{\parallel} \left( \hat{T}_e \hat{\nabla}_{\parallel} \log(\hat{n}_e) + 0.71 \hat{\nabla}_{\parallel} \hat{T}_e + \frac{m_e}{m_u} \hat{D}_{\perp, u_i} \right) \end{cases} \quad (4.34)$$

For better readability this system can be expressed in matrix form, where  $\circ$  shall be replaced by the corresponding field within operators.

$$\begin{pmatrix} \hat{\nabla} \cdot \left[ \frac{\hat{m}_a \hat{n}_a}{\hat{B}^2} \hat{\partial}_t \hat{\nabla}_{\perp} \circ \right] & -\hat{\nabla} \cdot [\circ \vec{b}] \\ \hat{\sigma}_{\parallel} \hat{\nabla}_{\parallel} \circ & 1 + \frac{m_e \hat{\sigma}_{\parallel}}{m_u \hat{n}} (\hat{\partial}_t \circ - \hat{\nabla} \cdot \hat{v}_e \hat{\nabla}_{\perp} \circ) \end{pmatrix} \begin{pmatrix} \hat{\Phi} \\ \hat{j}_{\parallel} \end{pmatrix} = \begin{pmatrix} -\hat{\partial}_t \hat{\Omega}_{\pi} \\ \hat{\sigma}_{\parallel} \left( \hat{T}_e \hat{\nabla}_{\parallel} \log(\hat{n}_e) + 0.71 \hat{\nabla}_{\parallel} \hat{T}_e + \frac{m_e}{m_u} \hat{D}_{\perp, u_i} \right) \end{pmatrix} \quad (4.35)$$

4. Electromagnetic effects coupled to the SOLEDGE3X framework – 4.5. Expressing the electromagnetic vorticity equation in matrix form

### 4.5.2. Electromagnetic vorticity system

The second line of the system in [Equation 4.27](#) might be dedimensionalized as follows:

$$\begin{aligned} \hat{\nabla} \cdot \left[ \frac{A_{\parallel}^0}{\rho_0^2} \hat{\nabla}_{\perp} \hat{A}_{\parallel} \right] &= -\mu_0 \sigma_{\parallel}^0 \hat{\sigma}_{\parallel} \left( -\frac{\Phi_0}{\rho_0} \hat{\nabla}_{\parallel} \hat{\Phi} - \frac{A_{\parallel}^0}{\tau_0} \hat{\partial}_t \hat{A}_{\parallel} + \frac{T_0 \hat{T}_e}{e \rho_0} \hat{\nabla}_{\parallel} \log(\hat{n}_e) + \frac{1.71 T_0}{e \rho_0} \hat{\nabla}_{\parallel} \hat{T}_e \right) \\ \Leftrightarrow \quad \hat{\nabla} \cdot [\hat{\nabla}_{\perp} \hat{A}_{\parallel}] &= \hat{\sigma}_{\parallel} \left( \hat{\nabla}_{\parallel} \hat{\Phi} + \frac{\beta_0}{2} \hat{\partial}_t \hat{A}_{\parallel} - \hat{T}_e \hat{\nabla}_{\parallel} \log(\hat{n}_e) - 1.71 \hat{\nabla}_{\parallel} \hat{T}_e \right) \end{aligned}$$

Now, all components are available for a fully dedimensionalized version of the new system in [Equation 4.27](#):

$$\begin{cases} \hat{\nabla} \cdot \left[ \frac{\hat{m}_{\alpha} \hat{n}_{\alpha}}{\hat{B}^2} \hat{\partial}_t \hat{\nabla}_{\perp} \hat{\Phi} \right] + \hat{\nabla} \cdot \left[ \hat{\sigma}_{\parallel} (\hat{\nabla}_{\parallel} \hat{\Phi} + \frac{1}{2} \beta_0 \hat{\partial}_t \hat{A}_{\parallel}) \vec{b} \right] &= \hat{\nabla} \cdot \left[ \hat{\sigma}_{\parallel} (\hat{T}_e \hat{\nabla}_{\parallel} \log(\hat{n}_e) + 1.71 \hat{\nabla}_{\parallel} \hat{T}_e) \vec{b} \right] - \hat{\partial}_t \hat{\Omega}_{\pi} \\ -\hat{\nabla} \cdot [\hat{\nabla}_{\perp} \hat{A}_{\parallel}] + \hat{\sigma}_{\parallel} (\hat{\nabla}_{\parallel} \hat{\Phi} + \frac{1}{2} \beta_0 \hat{\partial}_t \hat{A}_{\parallel}) &= \hat{\sigma}_{\parallel} (\hat{T}_e \hat{\nabla}_{\parallel} \log(\hat{n}_e) + 1.71 \hat{\nabla}_{\parallel} \hat{T}_e) \end{cases} \quad (4.36)$$

It can also be compactly expressed in matrix form:

$$\begin{pmatrix} \hat{\nabla} \cdot \left[ \frac{\hat{m}_{\alpha} \hat{n}_{\alpha}}{\hat{B}^2} \hat{\partial}_t \hat{\nabla}_{\perp} \circ \right] + \hat{\nabla} \cdot \left[ \hat{\sigma}_{\parallel} \hat{\nabla}_{\parallel} \circ \vec{b} \right] & \frac{1}{2} \beta_0 \hat{\nabla} \cdot [\hat{\sigma}_{\parallel} \hat{\partial}_t \circ] \\ \hat{\sigma}_{\parallel} \hat{\nabla}_{\parallel} \circ & \frac{1}{2} \beta_0 \hat{\sigma}_{\parallel} \hat{\partial}_t \circ - \hat{\nabla} \cdot [\hat{\nabla}_{\perp} \circ] \end{pmatrix} \begin{pmatrix} \hat{\Phi} \\ \hat{A}_{\parallel} \end{pmatrix} = \begin{pmatrix} \hat{\nabla} \cdot \left[ \hat{\sigma}_{\parallel} (\hat{T}_e \hat{\nabla}_{\parallel} \log(\hat{n}_e) + 1.71 \hat{\nabla}_{\parallel} \hat{T}_e) \vec{b} \right] - \hat{\partial}_t \hat{\Omega}_{\pi} \\ \hat{\sigma}_{\parallel} (\hat{T}_e \hat{\nabla}_{\parallel} \log(\hat{n}_e) + 1.71 \hat{\nabla}_{\parallel} \hat{T}_e) \end{pmatrix} \quad (4.37)$$

### 4.5.3. Dimensionless electromagnetic vorticity system with electron inertia

The last formulation of the vorticity equation that will be introduced in this chapter is the natural combination of the two precedent. We have a system over current density  $j_{\parallel}$  and the potential fields  $\Phi$  and  $A_{\parallel}$ .

It might suggest itself to use the now available parallel current density in Ampère's law.

$$\begin{cases} \hat{\nabla} \cdot \left[ \frac{\hat{m}_{\alpha} \hat{n}_{\alpha}}{\hat{B}^2} \hat{\partial}_t \hat{\nabla}_{\perp} \hat{\Phi} \right] - \hat{\nabla} \cdot [\hat{j}_{\parallel} \vec{b}] &= -\hat{\partial}_t \hat{\Omega}_{\pi} \\ \frac{1}{\hat{\sigma}_{\parallel}} \hat{j}_{\parallel} + \frac{m_e}{m_u \hat{n}} (\hat{\partial}_t \hat{j}_{\parallel} - \hat{\nabla} \cdot \hat{v}_e \hat{\nabla}_{\perp} \hat{j}_{\parallel}) + \hat{\nabla}_{\parallel} \hat{\Phi} + \frac{1}{2} \beta_0 \hat{\partial}_t \hat{A}_{\parallel} &= \hat{T}_e \hat{\nabla}_{\parallel} \log(\hat{n}_e) + 1.71 \hat{\nabla}_{\parallel} \hat{T}_e + \frac{m_e}{m_u} \hat{D}_{\perp, u_i} \\ \hat{\nabla} \cdot [\hat{\nabla}_{\perp} \hat{A}_{\parallel}] + \hat{j}_{\parallel} &= 0 \end{cases} \quad (4.38)$$

4. Electromagnetic effects coupled to the SOLEDGE3X framework – 4.5. Expressing the electromagnetic vorticity equation in matrix form

In matrix form, this final system reads:

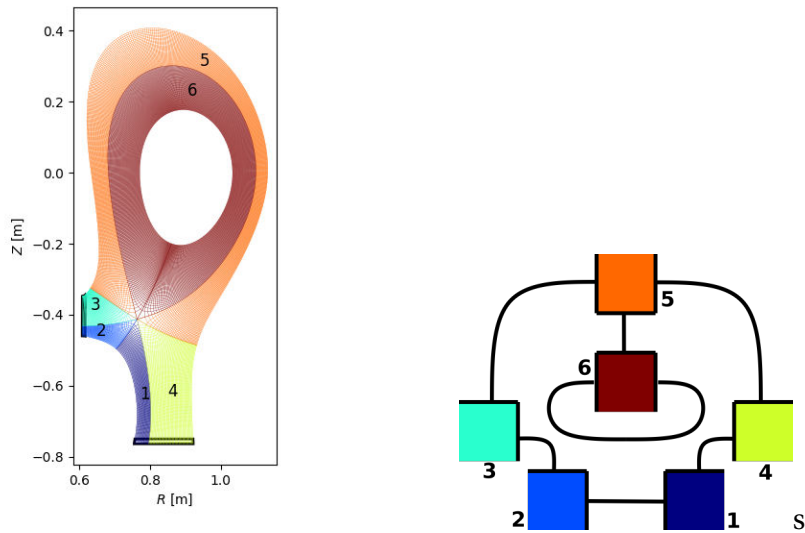
$$\begin{pmatrix}
 \hat{\nabla} \cdot \left[ \frac{\hat{m}_\alpha \hat{n}_\alpha}{\hat{B}^2} \hat{\partial}_t \hat{\nabla}_\perp \circ \right] & -\hat{\nabla} \cdot [\circ \vec{b}] & 0 \\
 \hat{\sigma}_\parallel \hat{\nabla}_\parallel \circ & 1 + \frac{m_e \hat{\sigma}_\parallel}{m_u \hat{n}} (\hat{\partial}_t \circ -\hat{\nabla} \cdot \hat{\nabla}_e \hat{\nabla}_\perp \circ) & \frac{1}{2} \beta_0 \hat{\sigma}_\parallel \hat{\partial}_t \\
 0 & 1 & \hat{\nabla} \cdot [\hat{\nabla}_\perp \circ]
 \end{pmatrix}
 \begin{pmatrix}
 \hat{\Phi} \\
 \hat{j}_\parallel \\
 \hat{A}_\parallel
 \end{pmatrix}
 = 
 \begin{pmatrix}
 -\hat{\partial}_t \hat{\Omega}_\pi \\
 \hat{\sigma}_\parallel \left( \hat{T}_e \hat{\nabla}_\parallel \log(\hat{n}_e) + 1.71 \hat{\nabla}_\parallel \hat{T}_e + \frac{m_e}{m_u} \hat{D}_{\perp, u_i} \right) \\
 0
 \end{pmatrix} \quad (4.39)$$

# 5. Numerical Implementation

## 5.1. Geometrical consideration

### 5.1.1. Domain decomposition and mesh design

In order to keep a structured flux-surfaces aligned mesh for any magnetic equilibrium, the real domain is mapped into a Cartesian domain decomposed into multiple connected zones [64]. Each point of the domain is distinctly identified by the set of curvilinear coordinates  $[\psi, \theta^*, \varphi]$  defined in Sec. ???. The domain is segmented along the toroidal coordinate  $\varphi$ , into  $N_\varphi$  poloidal planes. Tables of data fields are provided for each subdomain. Ghost cells store the information on the neighborhood within a matrix that defines how these subdomains are connected to each other. Depending on the domain, these ghost cells contain either the values of the neighboring subdomains' fields or the values imposed by the boundary conditions. An example of the mesh and its zone decomposition is shown in Fig. 5.1, where the X-point requires six zones.



(a) Typical mesh and zones decomposition in a poloidal plane of tokamak (b) Zones in the domain decomposition

Figure 5.1.: Example of typical mesh and domain decomposition mapping the real domain (a) to a Cartesian multiple zones domain (b). Each colored zone is isomorphic to a cube, the lines connecting the edges indicate the neighbours mapping.

### 5.1.2. Curvilinear coordinates

As it was described in the previous ??, the spatial discretization involves a curved grid in poloidal  $\theta$  and toroidal  $\varphi$  directions. The second chapter of the book by D'haeseleer et al [10] describes well the numerical implications of curvilinear grids and serves as the basis of the present implementation.

Let  $U = [u^\psi, u^\theta, u^\varphi]^T$  be the three parameters that describe every point in the domain  $\Omega$  with respect to the curvilinear system of coordinates. On a torus, we can find an invertible transformation  $R$  that maps each possible  $U \in \Omega$  to a unique point in cartesian coordinates, thus:

$$\begin{bmatrix} x \\ y \\ z \end{bmatrix} = \vec{R}(u^\psi, u^\theta, u^\varphi)$$

If we fix one parameter and allow the two remaining to vary freely, we obtain the so-called coordinate surface. Analogously if we fix two parameters, we obtain the coordinate curve associated to the free parameter and an accommodating choice for the scalar values  $u^i$  is the curve length from an arbitrary reference point. At any point  $P \in \Omega$ , a local basis  $\vec{e}_\psi, \vec{e}_\theta, \vec{e}_\varphi$  can be defined by the tangents to the respective coordinate curves crossing this point. Consequently, the basis vectors are easily expressed as:

$$\vec{e}_\psi = \frac{\partial \vec{R}}{\partial u^\psi} \quad \vec{e}_\theta = \frac{\partial \vec{R}}{\partial u^\theta} \quad \vec{e}_\varphi = \frac{\partial \vec{R}}{\partial u^\varphi}$$

The parameter choice of  $u^i$  can be seen as the curve length and it might or might not be a unit length. The dimension index appears in subscript  $\vec{e}_i$  to indicate that the basis vectors originate from a  $u^i$  located below the fraction line.

An alternative basis can be defined from the gradients of the parameters  $u^i$  which hence uses a superscript notation:

$$\vec{e}^\psi = \nabla u^\psi \quad \vec{e}^\theta = \nabla u^\theta \quad \vec{e}^\varphi = \nabla u^\varphi$$

These basis vectors are orthogonal to the respective coordinate surfaces at the point  $P$ . It can be shown that both basis are reciprocal, thus:

$$e^i \cdot e_j = \delta_j^i$$

where  $\delta_j^i$  is the Kronecker delta.

This leads to the introduction of the covariant (linked to subscripts) and contravariant (linked to the superscripts) components of a vector. As it is known from linear algebra, any vector  $\vec{v}$  can be expressed with respect to an arbitrary basis  $\tilde{e}_i$  as  $\vec{v} = \tilde{v}_i \tilde{e}_i$ . For the

## 5. Numerical Implementation – 5.1. Geometrical consideration

two previously introduced basis, the respective components of  $\vec{v}$  are given by:

$$\begin{array}{lll} \text{Covariant components: } v_i = \vec{v} \cdot \vec{e}_i & \Rightarrow & \vec{v} = v_i \vec{e}^i \\ \text{Contravariant components: } v^i = \vec{v} \cdot \vec{e}^i & \Rightarrow & \vec{v} = v^i \vec{e}_i \end{array}$$

It is common practice to call the representation of  $\vec{v}$  using the co-/contravariant components the co-/contravariant vector of  $\vec{v}$  albeit the co- and contravariant vectors both naturally describe the same vector  $\vec{v}$ .

Next, we introduce the metric coefficients  $g_{ij} = \vec{e}_i \cdot \vec{e}_j$  and their reciprocal metric coefficients  $g^{ij} = \vec{e}^i \cdot \vec{e}^j$ . If available, they allow for an easy both-way conversion of contravariant to covariant vectors and consequently an easy change of basis.

$$\begin{array}{ll} v_i = g_{ij} v^j & \vec{e}_i = g_{ij} \vec{e}^j \\ v^i = g^{ij} v_j & \vec{e}^i = g^{ij} \vec{e}_j \end{array}$$

It may be noted that the matrices formed by the indices  $i, j \in \{\theta, \psi, \varphi\}$  are each other's inverse matrix.

### 5.1.2.1. Linear algebra

The metric coefficients together with the co-/contravariant vectors are useful tools to perform several operations on the curvilinear grid. First of all, the squared Jacobian of the transformation from the cartesian to the curvilinear coordinate systems is equal to the determinant of  $g_{ij}$ .

$$J = \frac{\partial(x, y, z)}{\partial(u^\psi, u^\theta, u^\varphi)} = \sqrt{\det[g_{ij}]} \quad (5.1)$$

The dot product between two vectors  $\vec{v}$  and  $\vec{w}$  is calculated with the co-/contravariant vectors.

$$\vec{v} \cdot \vec{w} = g_{ij} v^i w^j = g^{ij} v_i w_j \quad (5.2)$$

The co-/contravariant components of the cross product can also be calculated:

$$\left\{ \begin{array}{l} (\vec{v} \times \vec{w})_k = J \epsilon_{ijk} v^i w^j \\ (\vec{v} \times \vec{w})^k = \frac{1}{J} \epsilon_{ijk} v_i w_j \end{array} \right. \quad (5.3)$$

This operations involves the Levi-Civita symbol  $\epsilon_{ijk}$  which takes the value +1 for all even permutations  $\{\psi, \theta, \varphi\}, \{\theta, \varphi, \psi\}$  and  $\{\varphi, \psi, \theta\}$ , the value -1 for all odd permutations  $\{\varphi, \theta, \psi\}, \{\theta, \psi, \varphi\}$  and  $\{\psi, \varphi, \theta\}$ , and is 0 for all other cases.

In various formulae such as ..., ... or ... of the SOLEDGE3X model, we need to split a vector into its parallel and perpendicular component with respect to the magnetic

field  $\vec{B}$ .

$$\vec{v}_\parallel = \vec{v} \cdot \vec{b} \quad \vec{v}_\perp = -\vec{b} \times (\vec{b} \times \vec{v}) \quad (5.4)$$

The vector  $\vec{b}$  contains the normalized magnetic field and hence represents a unit vector in parallel direction at each point. In the code only its co- and contravariants are calculated and stored for the entire mesh:

$$b_\psi = \vec{b} \cdot \vec{e}_\psi \quad b_\theta = \vec{b} \cdot \vec{e}_\theta \quad b_\varphi = \vec{b} \cdot \vec{e}_\varphi \quad (5.5)$$

$$b^\psi = \vec{b} \cdot \vec{e}^\psi \quad b^\theta = \vec{b} \cdot \vec{e}^\theta \quad b^\varphi = \vec{b} \cdot \vec{e}^\varphi \quad (5.6)$$

### 5.1.2.2. Differentiation

The gradient of a scalar field  $S(u^\psi, u^\theta, u^\varphi)$  is calculated in terms of the reciprocal basis:

$$(\nabla S)_i = \frac{\partial S}{\partial u^i} \vec{e}^i \quad (5.7)$$

In the transport equations, we need to calculate gradients in parallel direction of the field which allows us to express  $\vec{\nabla}_\parallel$  in terms of the contravariant vector of the unit magnetic field from [Equation 5.6](#).

$$\nabla_\parallel S = \frac{\partial S}{\partial u^i} \vec{b} \cdot \vec{e}^i = \frac{\partial S}{\partial u^\theta} b^\theta + \frac{\partial S}{\partial u^\varphi} b^\varphi \quad (5.8)$$

The terms in  $\psi$  are omitted in the above formula since the equilibrium magnetic flux surfaces are located on the  $\theta$ - $\varphi$  coordinate surface and the vector  $\vec{b}$  has therefore a zero value in its radial component. Note that this gradient is a scalar as it always points in  $\vec{b}$  direction.

Similarly, a perpendicular gradient can be defined as:

$$\vec{\nabla}_\perp S = \vec{\nabla} S - (\nabla_\parallel S) \vec{b}$$

In terms of metric coefficients, it translates to:

$$\begin{aligned} (\vec{\nabla}_\perp S)^i &= g^{ij} (\nabla S)_j - (\nabla_\parallel S) b^i \\ &= g^{ij} \frac{\partial S}{\partial u^j} - \left( \frac{\partial S}{\partial u^\theta} b^\theta + \frac{\partial S}{\partial u^\varphi} b^\varphi \right) b^i \end{aligned} \quad (5.9)$$

We have to keep in mind that the above expression leads to the contravariant components of the perpendicular gradient whereas the general expression for the gradient in [Equation 5.7](#) gives its covariant components.

## 5. Numerical Implementation – 5.2. The staggered mesh

Next, the divergence of a vector  $\vec{v}$  is calculated by:

$$\vec{\nabla} \cdot \vec{v} = \frac{1}{J} \frac{\partial(JA^i)}{\partial u^i} \quad (5.10)$$

and further the divergence of parallel vector fields  $S_{\parallel} \vec{b}$  comes in handy:

$$\vec{\nabla} \cdot (S_{\parallel} \vec{b}) = \frac{1}{J} \left[ \frac{\partial(JS_{\parallel} b^{\theta})}{\partial u^{\theta}} + \frac{\partial(JS_{\parallel} b^{\varphi})}{\partial u^{\varphi}} \right] \quad (5.11)$$

The gradient and divergence operators can be combined to define a diffusion operator. The parallel Laplacian with some diffusion coefficients  $D$  reads in metric terms:

$$\vec{\nabla} \cdot [D(\nabla_{\parallel} S) \vec{b}] = \frac{1}{J} \left[ \frac{\partial \left( JD \left( \frac{\partial S}{\partial u^{\theta}} b^{\theta} + \frac{\partial S}{\partial u^{\varphi}} b^{\varphi} \right) b^{\theta} \right)}{\partial u^{\theta}} + \frac{\partial \left( JD \left( \frac{\partial S}{\partial u^{\theta}} b^{\theta} + \frac{\partial S}{\partial u^{\varphi}} b^{\varphi} \right) b^{\varphi} \right)}{\partial u^{\varphi}} \right] \quad (5.12)$$

Similarly, a perpendicular diffusion operator can be defined:

$$\begin{aligned} \vec{\nabla} \cdot [D \vec{\nabla}_{\perp} S] &= \vec{\nabla} \cdot \left[ D \left( \vec{\nabla} S - (\nabla_{\parallel} S) \vec{b} \right) \right] \\ &= \frac{1}{J} \frac{\partial}{\partial u^i} \left[ JD \left( g^{ij} \frac{\partial S}{\partial u^j} - \left( \frac{\partial S}{\partial u^{\theta}} b^{\theta} + \frac{\partial S}{\partial u^{\varphi}} b^{\varphi} \right) b^i \right) \right] \\ &= \frac{1}{J} \left( \frac{\partial}{\partial u^{\psi}} \left[ JD \left( g^{\psi\psi} \frac{\partial S}{\partial u^{\psi}} + g^{\psi\varphi} \frac{\partial S}{\partial u^{\theta}} + g^{\psi\theta} \frac{\partial S}{\partial u^{\varphi}} \right) \right] \right. \\ &\quad + \frac{\partial}{\partial u^{\theta}} \left[ JD \left( g^{\theta\psi} \frac{\partial S}{\partial u^{\psi}} + \left( g^{\theta\theta} - b^{\theta} b^{\theta} \right) \frac{\partial S}{\partial u^{\theta}} + \left( g^{\theta\varphi} - b^{\varphi} b^{\theta} \right) \frac{\partial S}{\partial u^{\varphi}} \right) \right] \\ &\quad \left. + \frac{\partial}{\partial u^{\varphi}} \left[ JD \left( g^{\varphi\psi} \frac{\partial S}{\partial u^{\psi}} + \left( g^{\varphi\varphi} - b^{\theta} b^{\varphi} \right) \frac{\partial S}{\partial u^{\theta}} + \left( g^{\varphi\theta} - b^{\varphi} b^{\theta} \right) \frac{\partial S}{\partial u^{\varphi}} \right) \right] \right) \end{aligned} \quad (5.13)$$

### 5.1.3. Finite volume approach

The spatial discretization is based on a second-order conservative finite-volume scheme associated with a 3rd-order WENO reconstruction and Donat, Marquina fluxes for a modified Riemann solver for the advection terms to handle both shocks and complicated smooth solution structures [4, 64].

## 5.2. The staggered mesh

In order to benefit from the first-order parallel derivative that separates the  $A_{\parallel}$  and  $j_{\parallel}$  from the other plasma fields  $\Phi$ ,  $n_e$ , and  $T_e$  (Eqs. ?? and ??), these two variables are defined on a toroidally  $\varphi$  and poloidally  $\theta$  staggered grid. They are calculated at

cell edges in the parallel direction and can be directly matched to the fluxes entering and leaving the collocated cells. One of the major benefits is to minimize numerical diffusion and preserve turbulent structures, following findings in FVM simulations for fluid mechanics [43]. In the radial  $\psi$  direction, we keep the collocated position as the only parallel gradient in  $\psi$  comes from the flutter term, which in nature is much smaller than the equilibrium field. If the mesh were also staggered in  $\psi$ , we would face strong numerical radial diffusion of parallel fluxes, defying the motivation of a staggered grid for  $A_{\parallel}$  and  $j_{\parallel}$ .

### 5.2.1. Description and notation of the staggered grid

The scalar variable  $A_{\parallel}$  is the magnitude of the parallel magnetic vector potential that is a factor of the unit vector  $\vec{b}$  in direction of the externally induced magnetic field lines. By construction of the domain,  $\vec{b}$  has only components in  $\varphi$  and  $\theta$  directions. So far, all physical quantities are calculated on the collocated grid points at the domain cell centers. In the newly introduced equation on  $A_{\parallel}$ , the magnetic vector potential appears homogeneous to the potential, pressure and temperature gradients and the additional  $A_{\parallel}$  term in the original equation states that the divergence of  $A_{\parallel}$  accounts for the change in vorticity. Thus,  $A_{\parallel}$  is always one spatial derivative away from the original quantities. As it is common in classical CFD simulation the velocity,  $A_{\parallel}$  is not defined on cell centers but on a staggered grid on the cell edges in  $\psi$ -direction. Because the magnetic field lines do not evolve in radial direction and only parallel gradients contribute to  $A_{\parallel}$ , its grid is only staggered in poloidal and toroidal directions. To distinguish quantities on both grids, the indexes  $[i_{\psi}, i_{\theta} - \frac{1}{2}, i_{\varphi} - \frac{1}{2}]$  describe discrete positions on the staggered grid.

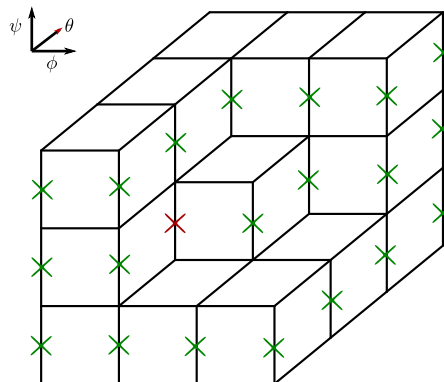


Figure 5.2.: General view of the staggered grid points marked as crosses on top of the collocated cells. The red cross at the position  $[i_{\psi}, i_{\theta} - \frac{1}{2}, i_{\varphi} - \frac{1}{2}]$  corresponds to the central cell with index  $[i_{\psi}, i_{\theta}, i_{\varphi}]$

In the following work, quantities evaluated at staggered grid points are indicated either by the superscript  $stg$  or by a  $-\frac{1}{2}$  shift in the index. This means that following

notations are equivalent:

$$X_{[i_\psi, i_\theta, i_\varphi]}^{stg} = X_{[i_\psi, i_\theta - \frac{1}{2}, i_\varphi - \frac{1}{2}]} \quad \text{or} \quad X_{[i_\psi, i_\theta + 1, i_\varphi]}^{stg} = X_{[i_\psi, i_\theta + \frac{1}{2}, i_\varphi - \frac{1}{2}]}^{}$$

### 5.2.2. Boundary cells

Staggered quantities require a different treatment at the domain boundary. In the geometry definition, entire cells belong either to the plasma or to the physical wall. Collocated quantities in the boundary layer are thus always half a cell width away from the wall and boundary conditions are enforced accordingly. For the magnetic vector potential this holds for walls in  $\psi$  direction but in  $\varphi$  and  $\theta$  directions, the staggered grid points are on the tokamak wall for the boundary cells with lowest index and one cell width away at the highest index. For consistency, accuracy and symmetry purposes, the staggered solvable domain shall be either extended by one row of cells at the upper index to include the wall in the solution or reduced by one row at the lower end. In both cases, the number of collocated and staggered grid points do not match anymore and inhibit all eventual symmetry properties of the matrix in the dual-grid system (??).  $A_{\parallel}$  requires Dirichlet boundary conditions with the value 0 everywhere, thus the solution on the wall is already known and is not needed in the system. Therefore the latter option without the staggered grid points of the lower boundary cell layer is more suitable and has been implemented as depicted in [Figure 5.3](#).

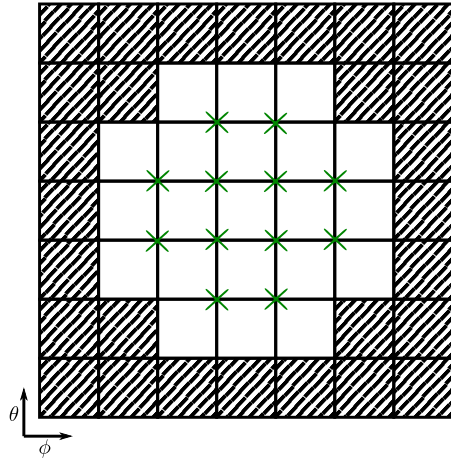


Figure 5.3.: General view of the staggered grid points in the  $\theta - \varphi$  plane that are solved in the vorticity equation. Note that at the lower boundaries, collocated fields are included in the system but not their staggered counterparts.

In the system (??), some entries for the electric potential  $\Phi$  do not have a corresponding magnetic potential  $A_{\parallel}$ . To ensure a correct implementation of the system and the stencils that appear in it, a new mask  $\chi^{stg}$  describes which cells contain staggered grid points in the solvable domain. It is defined from the original collocated wall mask  $\chi$

## 5. Numerical Implementation – 5.2. The staggered mesh

as:

$$\chi_{[i_\psi, i_\theta, i_\varphi]}^{stg} = 1 - (1 - \chi_{[i_\psi, i_\theta, i_\varphi]})(1 - \chi_{[i_\psi, i_\theta-1, i_\varphi]})(1 - \chi_{[i_\psi, i_\theta, i_\varphi-1]})(1 - \chi_{[i_\psi, i_\theta-1, i_\varphi-1]}) \quad (5.14)$$

The value of  $\chi_{[i_\psi, i_\varphi, i_\theta]}^{stg}$  is therefore 1 if the staggered grid point of the cell with index  $[i_\psi, i_\varphi, i_\theta]$  lies on or in the wall and it is 0 inside the solvable domain.

Another implication for staggered fields occurs at sheath boundaries, where  $A_{\parallel}$  and  $j_{\parallel}$  lie on the domain boundary. For collocated fields, we impose sheath fluxes from the Bohm-Chodura model (see Sec. ??) on the first cell in the simulation domain. For the magnetic potential  $A_{\parallel}$ , the 0-Dirichlet condition is imposed in the concerned cell. For the parallel current  $j_{\parallel}$ , we add the sheath current  $j_{\text{wall}}$  to any parallel currents tangential to the wall. Indeed, if the sheath boundary is in the  $\theta$  direction, the  $\varphi$  component of the parallel current remains unaffected and needs to be solved.

### 5.2.3. Staggered discrete operators

As the parallel current  $j_{\parallel}$  and the magnetic vector potential  $A_{\parallel}$  are defined on a staggered grid, new stencil operators are needed to be compatible with the electric potential  $\Phi$  defined on the collocated grid at the cell centers.

#### 5.2.3.1. Divergence on a parallel vector field

In [Equation 4.27](#), the divergence of  $j_{\parallel}$  needs to be calculated at the collocated grid. We thus need a discrete stencil operator

$$[\nabla \cdot X^{stg} \vec{b}]_{[i_\psi, i_\theta, i_\varphi]}^{col}$$

In [Equation 5.11](#), the divergence of a parallel vector field has been introduced. We consider a collocated cell as in [Figure 5.2](#). The flux  $\frac{\partial(JXb^{\theta})}{\partial i^{\theta}}$  is then the difference between the inflow and the outflow through the two cell faces facing the  $\theta$  axis. We want to calculate these fluxes from the flux  $F^{X,in} = JXb^{\theta}$  of the staggered field  $X$  known at the crosses in the schematic. We further assume that the inflow to the central collocated cell is the mean of the fluxes at the red cross and at the green cross right to it:

$$\begin{aligned} F_{[i_\psi, i_\theta, i_\varphi]}^{X,\theta} &= \frac{1}{2} \left( F_{[i_\psi, i_\theta-\frac{1}{2}, i_\varphi-\frac{1}{2}]}^{X,\theta} + F_{[i_\psi, i_\theta-\frac{1}{2}, i_\varphi+\frac{1}{2}]}^{X,\theta} \right) \\ &= J_{[i_\psi, i_\theta-\frac{1}{2}, i_\varphi-\frac{1}{2}]} X_{[i_\psi, i_\theta-\frac{1}{2}, i_\varphi-\frac{1}{2}]} b_{[i_\psi, i_\theta-\frac{1}{2}, i_\varphi-\frac{1}{2}]}^{\theta} + J_{[i_\psi, i_\theta-\frac{1}{2}, i_\varphi+\frac{1}{2}]} X_{[i_\psi, i_\theta-\frac{1}{2}, i_\varphi+\frac{1}{2}]} b_{[i_\psi, i_\theta-\frac{1}{2}, i_\varphi+\frac{1}{2}]}^{\theta} \end{aligned}$$

If one of the two staggered points lies on the domain boundary, it is not included in the flux calculation and consequently the factor 1/2 is dropped.

This numerical calculation can be performed for all in- and outflows in  $\theta$  and  $\varphi$

directions, leading to the final form of the numerical form of the staggered divergence stencil:

$$[\nabla \cdot X^{stg} \vec{b}]_{[i_\psi, i_\theta, i_\varphi]}^{col} = \frac{1}{J_{[i_\psi, i_\theta, i_\varphi]}} \left( F_{[i_\psi, i_\theta, i_\varphi]}^{X, \theta} - F_{[i_\psi, i_\theta+1, i_\varphi]}^{X, \theta} + F_{[i_\psi, i_\theta, i_\varphi]}^{X, \varphi} - F_{[i_\psi, i_\theta, i_\varphi+1]}^{X, \varphi} \right) \quad (5.15)$$

### 5.2.3.2. Parallel gradient

In [Equation 4.27](#), another operator is needed to represent the gradient of  $A_{\parallel} \vec{b}$  on the staggered grid.

$$[\nabla_{\parallel} X^{col}]_{[i_\psi, i_\theta, i_\varphi]}^{stg}$$

According to [Equation 5.8](#), its numerical evaluation is quite straight-forward:

$$\begin{aligned} [\nabla_{\parallel} X^{col}]_{[i_\psi, i_\theta, i_\varphi]}^{stg} &= \frac{1}{2} \left( X_{[i_\psi, i_\theta, i_\varphi]} - X_{[i_\psi, i_\theta-1, i_\varphi]} \right) b_{[i_\psi, i_\theta-\frac{1}{2}, i_\varphi-\frac{1}{2}]}^{\theta} \\ &\quad + \frac{1}{2} \left( X_{[i_\psi, i_\theta, i_\varphi]} - X_{[i_\psi, i_\theta, i_\varphi-1]} \right) b_{[i_\psi, i_\theta-\frac{1}{2}, i_\varphi-\frac{1}{2}]}^{\varphi} \end{aligned} \quad (5.16)$$

If any of the used  $X$  happens to lie inside the boundary, it is eliminated from the stencil.

The staggered divergence and parallel gradient stencils already existed in a hidden form in the original SOLEDGE implementation as part of the parallel Laplacian operator on collocated fields, which first computes the parallel gradient leading to intermediate staggered results and then applies the divergence operator on these staggered intermediate results.

### 5.2.3.3. Perpendicular Laplacian

Finally, [Equation 4.27](#) requires the perpendicular Laplacian on the staggered grid to link  $j_{\parallel}$  and  $A_{\parallel}$ .

$$[\Delta_{\perp} X^{stg}]_{[i_\psi, i_\theta, i_\varphi]}^{stg}$$

In the scheme proposed by Günter et al. [\[25\]](#), this operation is performed in two steps: first the perpendicular gradient is evaluated on  $X^{stg}$  which produces an intermediate collocated vector field  $\vec{Y}^{col}$  whose divergence leads to the final staggered result. [Equation 5.13](#) includes all needed metrics to achieve this operation. To better understand the final divergence operation, we must imagine a cell centered around the point where the perpendicular Laplacian is required, depicted in [Figure 5.4a](#). We then need to calculate the fluxes  $F^{Y,i}$  across all six faces. The metric and diffusion coefficients  $JD(g^{ij} - b^i b^j)$  are also required at the faces and we obtain them by taking their average on the closest collocated points. In poloidal and toroidal directions two collocated points shown in green in [Figure 5.4c](#) and [Figure 5.4d](#) are sufficient but in radial direction we need to consider eight points around the face to calculate the

## 5. Numerical Implementation – 5.2. The staggered mesh

correct coefficients.

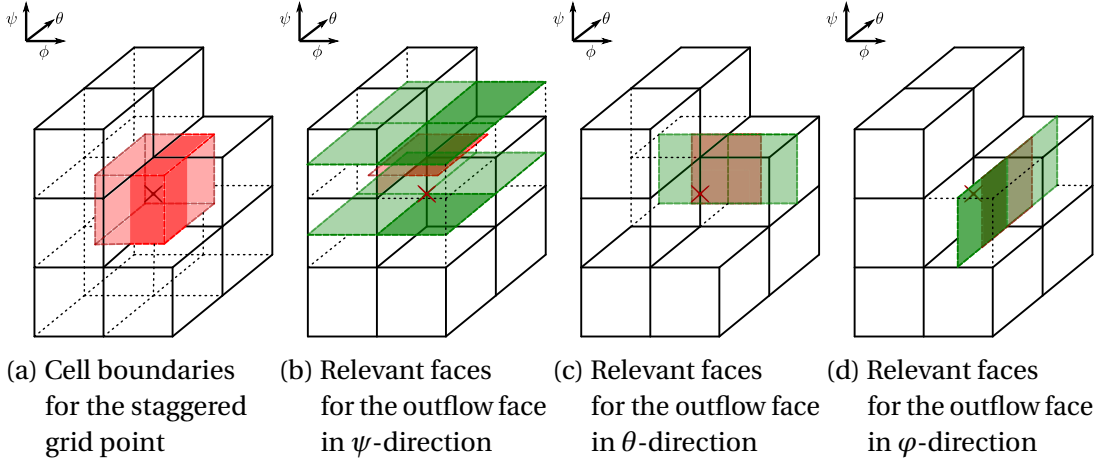


Figure 5.4.: Depiction of the relevant cell faces to calculate fluxes of a staggered field at coordinate index  $[i_\psi, i_\theta - \frac{1}{2}, i_\varphi - \frac{1}{2}]$

The perpendicular Laplacian can thus be succinctly written in term of the fluxes in and out of the staggered red cell:

$$[\Delta_{\perp} X^{stg}]_{[i_\psi, i_\theta, i_\varphi]}^{stg} = \frac{1}{J_{[i_\psi, i_\theta - \frac{1}{2}, i_\varphi - \frac{1}{2}]}} \left( F_{[i_\psi + \frac{1}{2}, i_\theta - \frac{1}{2}, i_\varphi - \frac{1}{2}]}^{Y, \psi} - F_{[i_\psi - \frac{1}{2}, i_\theta - \frac{1}{2}, i_\varphi - \frac{1}{2}]}^{Y, \psi} \right. \\ \left. + F_{[i_\psi, i_\theta, i_\varphi - \frac{1}{2}]}^{Y, \theta} - F_{[i_\psi, i_\theta - 1, i_\varphi - \frac{1}{2}]}^{Y, \theta} + F_{[i_\psi, i_\theta - \frac{1}{2}, i_\varphi]}^{Y, \varphi} - F_{[i_\psi, i_\theta - \frac{1}{2}, i_\varphi - 1]}^{Y, \varphi} \right) \quad (5.17)$$

If any of the staggered cell faces touches the domain boundary in any form, the corresponding flux is excluded from the divergence operator. It only remains to calculate the fluxes  $F^{Y,i}$ . The metric and diffusion coefficients at all faces have already been described and are represented by the term  $\xi^{ij} = JD(g^{ij} - b^i b^j)$ . We then can express the fluxes as:

$$F^{Y,i} = \xi^{ij} \frac{\partial X}{\partial u^j}$$

The remaining gradient must use  $X^{stg}$  at staggered points in the domain. If  $[ijk]$  stands for any permutation of the staggered indices  $[i_\psi, i_\theta - \frac{1}{2}, i_\varphi - \frac{1}{2}]$  we always have a flux of the kind:

$$F_{i-\frac{1}{2}, jk}^{Y,i} = \xi^{ii} \left( X_{ijk}^{stg} - X_{i-1,jk}^{stg} \right) \\ + \frac{1}{4} \xi^{ij} \left( X_{i,j+1,k}^{stg} - X_{i,j-1,k}^{stg} + X_{i-1,j+1,k}^{stg} - X_{i-1,j-1,k}^{stg} \right) \\ + \frac{1}{4} \xi^{ik} \left( X_{i,j,k+1}^{stg} - X_{i,j,k-1}^{stg} + X_{i-1,j,k+1}^{stg} - X_{i-1,j,k-1}^{stg} \right)$$

If any of the field points  $X$  lie in or on the domain boundary, it is not considered in

the stencil and the factor  $\frac{1}{4}$  is changed to  $\frac{1}{3}$ .

### 5.2.4. Discretization around the X-point

The staggered grid has direct implications on the estimation of fluxes around mesh singularities: while for regular fields, every cell around the X-point has well-defined neighbors (see Fig. 5.5a), radial fluxes in and out of staggered cells directly cross the X-point (see Fig. 5.5b). They affect the perpendicular Laplacian operator on  $A_{\parallel}$  in Ampere's law (Eq. ??), advection on  $j_{\parallel}$  in Eq. ??, and the anomalous perpendicular diffusion  $\mathcal{D}_{\perp}$ . To cope with the ill-defined cell faces, fluxes across the X-point are forced to 0 by Neumann-like boundary conditions. Neighbors of the involved cells must be defined separately from the regular cells with the same index.

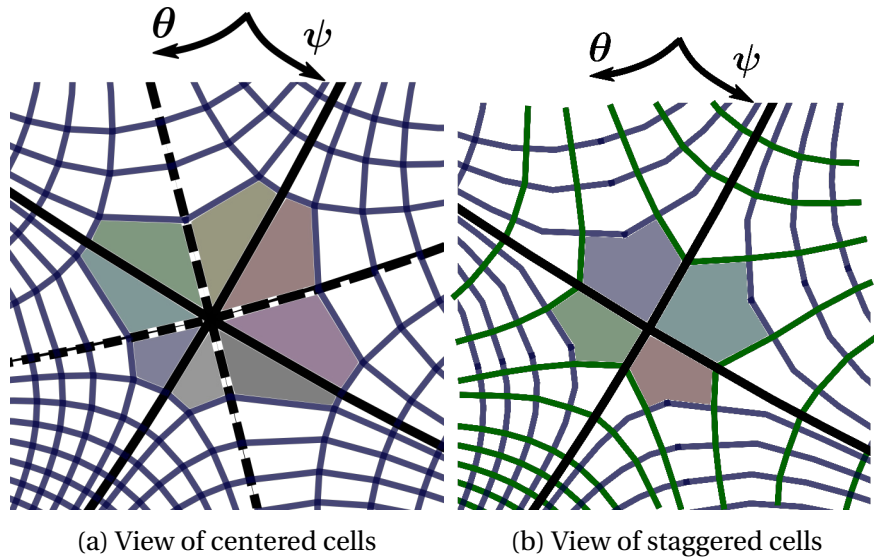


Figure 5.5.: Sketches of the mesh around the X-point. For centered cells (a), 8 cells touch the X-point at a corner. For staggered cells (b), the X-point is located at the radial face of 4 cells, effectively modifying the shape of the cells to pentagons. Fluxes across the involved faces are hence ill-defined.

## 5.3. Time discretization

The model uses an explicit time discretization for the advection terms and an implicit one for the diffusive terms. In turbulence simulations, we limit ourselves to timescales slower than the cyclotronic frequency  $\omega_C$ . This applies to all advection phenomena, as well as to friction, pressure, and energy source terms, which can then comfortably be solved explicitly in time.

However, ionization/recombination processes, resistive and viscous effects from the Spitzer-Härm model, and electron inertia involve much faster dynamics that would massively constrain the allowed timestep size. Therefore, these terms are solved implicitly. To reduce numerical complexity, they can be decoupled and solved sequentially for the density, the parallel velocity, the temperature, and finally the potentials.

### 5.3.1. Explicit Runge-Kutta solver

### 5.3.2. Implicit-explicit VSIMEX solver

The time discretization is based on a variable stepsize implicit-explicit scheme (VSIMEX) [69], associating explicit time discretization for the advection terms and an implicit one for the diffusive terms. In turbulence simulations, we limit ourselves to timescales slower than the cyclotronic frequency  $\omega_C$ . This applies to all advection phenomena, as well as to friction, pressure, and energy source terms, which can then comfortably be solved explicitly in time.

This multi-step method is implemented for orders 1 to 3, and the timestep is updated such that fluxes and velocities in the simulation domain match a targeted CFL value.

## 5.4. Initialization at Restart

### 5.4.1. Electron Inertia

Use the steady-state Ohm's law from the existing profile in  $\Phi$ .

### 5.4.2. Parallel Magnetic Vector Potential

Solve for the steady-state Ampère's law with the now available profile in  $j_{\parallel}$ . Creation of a new solver class for this purpose.

## 5.5. Implicit Numerical Treatment

### 5.5.1. Parallel diffusion operator with flutter

In the magnetostatic setting, the parallel diffusion operator on  $v_i$  and  $T_\alpha$  can be solved independently on each flux surface in a 2D system on the  $\theta - \varphi$  plane. The scheme developed by Günter et al. [24] has proven well-suited to solve the 2D parallel Laplacian equations with minimized numerical spread for highly anisotropic problems. For an operator of the type  $\nabla \cdot (\kappa \nabla_{\parallel} \circ \mathbf{b})$ , parallel gradients are first calculated in cell

corners with finite differences and then used in the fluxes across each cell face to get the divergence. The corners where gradients are calculated are shown in Figure 5.6a. This scheme is particularly effective if the poloidal and toroidal components  $b^\theta$  and  $b^\psi$  of the contravariant magnetic unit vector in the curvilinear metric have similar magnitudes. This is usually enforced through careful mesh generation.

However, with flutter (Sec. ??), magnetic flux surfaces are no longer aligned to the  $\theta - \varphi$  plane because of the new radial component  $b^\psi$ . As a consequence, all independent 2D problems across flux surfaces are now coupled into a single 3D problem. For the parallel diffusion solver, a first approach would be to extend the above scheme by calculating gradients in the 3D corners of our cells. However, the new component  $b^\psi$  is a pure fluctuation, which is therefore expected to be much smaller than  $b^\theta$  or  $b^\varphi$  and can even vanish locally. This results in significant spurious numerical diffusion in the radial direction of equilibrium gradients. To prevent this diffusion, and still properly capture radial flutter gradients, only crossed derivatives  $b^\theta b^\psi$  and  $b^\varphi b^\psi$  as well as the principal radial diffusion  $b^\psi b^\psi$  use gradients evaluated at 3D corners, while the equilibrium diffusion remains aligned to the  $\theta - \varphi$  plane. Examples of the gradients used in this new scheme are shown in Figs. 5.6b and 5.6c. The new discretization stencil then corresponds exactly to the equilibrium 2D stencil in the limit  $b^\psi = 0$ .

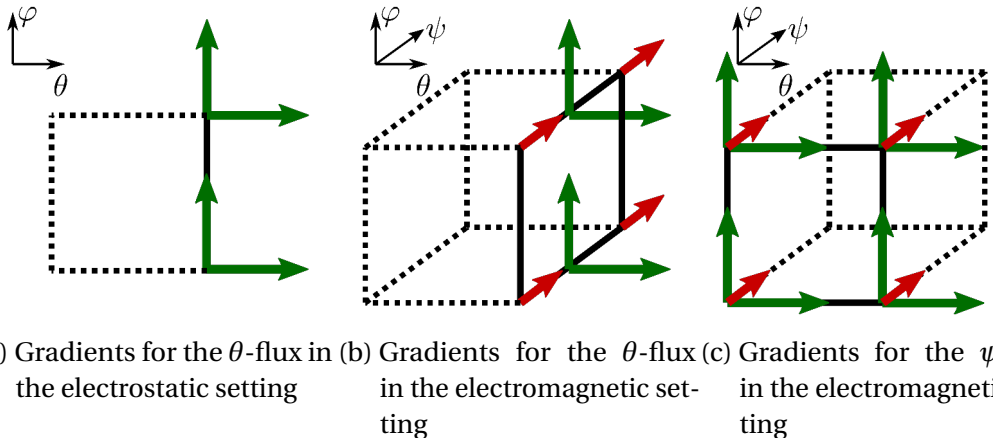


Figure 5.6.: Sketches showing the calculation of gradients for the parallel diffusion scheme. It shows the position where the different gradients are calculated that are relevant for a flux across the cell face with a solid line. Green and red arrows symbolize gradients in the equilibrium and in the radial direction, respectively.

### 5.5.2. Electromagnetic vorticity system

The newly introduced fields  $j_{\parallel}$  and  $A_{\parallel}$  are solved implicitly along with the electric potential  $\Phi$ . As we face a coupled system that connects all points in the domain, direct

solvers such as PASTIX are not suitable, especially for fine 3D meshes. We instead prefer to use iterative solvers available in the PETSc or HYPRE libraries. For the original vorticity system, the Stabilized version of the Biconjugate Gradient method (BiCGStab) along with the Geometric Algebraic Multigrid (GAMG) preconditioner proved to be very efficient and it is desirable to use them on the new systems. This section describes some special numerical features in the construction of the system to facilitate the convergence of the above iterative scheme. [subsubsection 5.5.2.2](#) introduces specific row and column scaling to equilibrate the blocks in the new system and [subsubsection 5.5.2.3](#) describes how to handle staggered fields to be compatible with the iterative scheme.

### 5.5.2.1. Expression for the coupled system

With the values for  $n_e$  and  $T_e$  known at time-step  $n + 1$ , the vorticity equation (Eq. ??) corresponds to a 3D costly system involving  $\Phi$ ,  $j_{\parallel}$ , and  $A_{\parallel}$ . To solve it efficiently, the  $j_{\parallel}$  advection and perpendicular diffusion are treated explicitly, allowing the integration of Ohm's law into the vorticity equation and Ampère's law. Then, at time-step  $n + 1$ , the following dimensionless system coupling the two potentials  $\Phi$  and  $A_{\parallel}$  must be solved:

$$\begin{pmatrix} \nabla \cdot [D_{\perp} \nabla_{\perp} \circ] + \nabla \cdot [D_{\parallel} \nabla_{\parallel} \circ \mathbf{b}] & \frac{\beta_0}{\delta t} \nabla \cdot [D_{\parallel} \circ \mathbf{b}] \\ D_{\parallel} \nabla_{\parallel} \circ & \frac{\beta_0}{\delta t} D_{\parallel} \circ - \nabla \cdot [\nabla_{\perp} \circ] \end{pmatrix} \begin{pmatrix} \Phi^{n+1} \\ A_{\parallel}^{n+1} \end{pmatrix} = \begin{pmatrix} \nabla \cdot [D_t j_{\parallel}^n \mathbf{b}] + \text{RHS}^{\Phi} \\ D_t j_{\parallel}^n + \text{RHS}^{A_{\parallel}} \end{pmatrix} \quad (5.18)$$

with  $D_{\perp} = \frac{m_i n_i}{B^2 \delta t}$ ,  $D_{\parallel} = \frac{1}{\eta_{\parallel} + \mu}$ ,  $D_t = \frac{\mu}{\eta_{\parallel} + \mu}$ , and  $\mu = m_e / (m_u n_e \delta t)$  accounting for electron inertia effects. The parameter  $\delta t$  derives from the integration scheme and is equal to the time-step in the case of a first-order implicit Euler scheme.

Since  $\eta_{\parallel} \propto T_e^{-1.5}$ , the parallel resistivity  $\eta_{\parallel}$  is often a small parameter that leads to strong anisotropy between the perpendicular and parallel Laplacian operators. However, the electron inertia term, being implemented in the current solver, acts as an upper limit for the parallel diffusion coefficient, which is expected to improve the matrix conditioning as  $\eta_{\parallel}$  approaches zero. This is in contrast to the original electrostatic model from [\[4\]](#).

### 5.5.2.2. Equilibration of the Matrix Blocks

The matrices in the electromagnetic model [section 4.4](#) can be decomposed in 2x2 or 3x3 block matrices that apply on the respective fields  $\Phi$ ,  $A_{\parallel}$  and/or  $j_{\parallel}$ . Apart of the use of dedimensionalized quantities, no effort was made so far to ensure that the blocks

are roughly of the same order of the magnitude, which is important for the condition number of the matrix, nor that the matrix is diagonally dominant, which is generally a desirable feature for fast convergence of iterative schemes.

In the following bits, we introduce some column  $c_X$  and row  $r_X$  scaling factors that are specific to the blocks  $X$  of the matrix such that the above conditions are fulfilled as well as possible. To ensure a correct solution, the row scaling factor  $r_X$  must be applied to the corresponding entry in the RHS vector and as a matter of fact, in the original vorticity matrix, we already have  $r_\Phi = J$  the metrical Jacobian from [subsection 5.1.2](#) to remove the effect of different mesh sizes in the domain on the discrete Laplacian operators. The column scaling factors  $c_X$  must be taken care of when retrieving the fields from the numerical solution and it is strongly recommended to apply them to the initial guess for the iterative scheme.

Some existing algorithms optimize the scaling task such as —cite—. However, they all require an expensive matrix analysis phase that must be repeated regularly since the matrix changes with the progress of the simulation. Therefore, we use the knowledge about the construction of the matrix blocks to define sufficiently good scaling factors. In the system with electron inertia ??

### 5.5.2.3. Staggered Fields in the Matrix

The GAMG multigrid solves the system on different coarser levels by restricting the matrix and the RHS vector and then interpolates the solution back to the finer levels. In the new system, two consecutive entries belong to different fields, which makes the whole restriction-interpolation task obsolete from the very first level since neither the solution nor the matrix entries are similar between neighbours. In general, PETSc takes care of multiple fields in a coupled system if one defines a block size (in our case either 2 or 3) that indicates GAMG how to match corresponding entries.vim However, as seen in ??, the fields  $A_{\parallel}$  and  $j_{\parallel}$  are defined on a staggered grid in poloidal and toroidal directions as opposed to the centered field for  $\Phi$ . For the system it means that at each wall in negative directions (at the left target and for non-axisymmetric geometries), a line and column for  $\Phi$  exists but not for the two other fields. This in turn is problematic for GAMG as the blocks are globally defined and two different fields would again end up together and the total system size might even not be a multiple of the blocksize (2 resp. 3), which at all prevents the initialization of the preconditioner.

For the parallel diffusion on the electric potential  $\nabla \cdot [D_{\parallel} \nabla_{\parallel} \Phi \mathbf{b}]$  with flutter, we do not use the stencil introduced in Sec. [5.5.1](#). To avoid numerical difficulties and the appearance of unphysical modes, the discretization of this term needs to be consistent with the parallel gradient and divergence operators in the same system. Since the grid for  $A_{\parallel}$  and  $j_{\parallel}$  is only staggered in the  $\theta$  and  $\varphi$  directions, we do not know them in the radial corners from Figs. [5.6b](#) and [5.6c](#). Instead, the discrete diffusion operator is defined as the combination of the operators for the gradient and the divergence. It involves two neighbors on both radial sides, so the resulting stencil is less compact but consistent with the remaining system. Note that in cases without

## *5. Numerical Implementation – 5.5. Implicit Numerical Treatment*

flutter ( $b^\psi = 0$ ), the diffusion operator exactly corresponds to Günter's scheme [24] because the staggered fields are known at the position of the green gradients in Fig. 5.6.

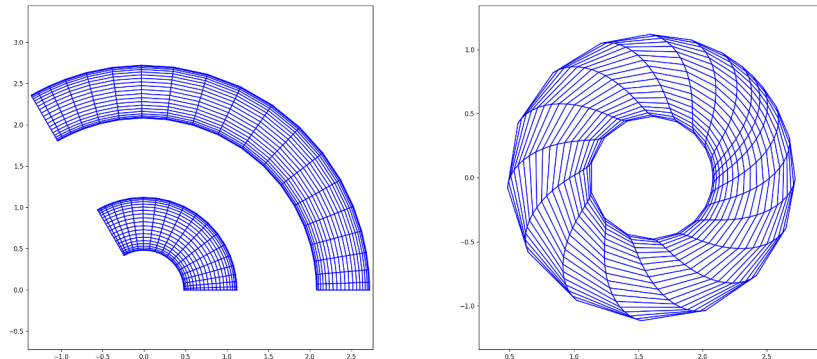
# 6. Verification and Validation

## 6.1. Verification by the Method of manufactured solutions

To ensure the correctness of the newly implemented system with the magnetic vector potential  $A_{\parallel}$ , a test model has been set up with the method of manufactured solutions (MMS) [53]. This allows to directly compare the numerical and analytic solutions and therefore validate the implementation and verify the order of convergence of the numerical operators.

### 6.1.1. Test system

The MMS test model is a fraction of a torus with a circular cross-section with an inner radius of 0.48m, an outer radius of 2.72m and a simulated plasma edge width of 0.64m. An example of the 3D mesh geometry is shown in Figure 6.1. To test the information exchange between zones in the model topology from ??, each coordinate direction is split in two zones totaling to 8 zones.



(a) Top view of the  $\psi - \varphi$  plane  
*the two bands correspond to the poloidal angles 0 and  $\pi$*

(b) View of a cross-section of the torus  
in the  $\psi - \theta$  plane  
*The cross-section is at  $\varphi = 0$*

Figure 6.1.: Distorted MMS mesh geometry with  $N = 20$  cells per dimension on a 3rd of a torus

## 6. Verification and Validation – 6.1. Verification by the Method of manufactured solutions

In the MMS geometry,  $\psi$  denotes the radius of the tube and  $R$  the radius of the entire torus. If  $aR_0 = 1.6$  is the distance of the tube center to the torus center, we have:

$$R = aR_0 + \psi \cdot \cos(\theta)$$

Together with the poloidal coordinate  $\theta \in [0, 2\pi]$  and the toroidal coordinate  $\varphi \in [0, 2\pi/N_{div}]$  where  $1/N_{div}$  is the considered fraction of the torus, each point in the domain is uniquely described by the curvilinear coordinates  $[\psi, \theta, \varphi]$ . We can define some  $\vec{P} = [X, Y, Z]^T$  in a cartesian basis of the 3D domain:

$$X = R \cos(\varphi) \quad Y = \psi \cdot \sin(\theta) \quad Z = R \sin(\varphi)$$

In this setting, the basis vectors of the curvilinear coordinates from [subsection 5.1.2](#) can be calculated analytically. The covariant basis vectors are:

$$\vec{e}_\psi = \frac{\partial \vec{P}}{\partial \psi} = \begin{bmatrix} \cos(\theta) \cos(\varphi) \\ \sin(\theta) \\ \cos(\theta) \sin(\varphi) \end{bmatrix} \quad \vec{e}_\theta = \frac{\partial \vec{P}}{\partial \theta} = \begin{bmatrix} -\psi \sin(\theta) \cos(\varphi) \\ \psi \cos(\theta) \\ -\psi \sin(\theta) \sin(\varphi) \end{bmatrix} \quad \vec{e}_\varphi = \frac{\partial \vec{P}}{\partial \varphi} = \begin{bmatrix} -Z \\ 0 \\ X \end{bmatrix}$$

We can further calculate the metric coefficients:

$$g_{ij} = \vec{e}_i \cdot \vec{e}_j = \begin{bmatrix} 1 & 0 & 0 \\ 0 & \psi^2 & 0 \\ 0 & 0 & R^2 \end{bmatrix} \quad \text{and} \quad J = \sqrt{\det[g_{ij}]} = \psi R$$

As generally required by S3X, the magnetic field is axisymmetric and thus does not depend on the toroidal coordinate  $\varphi$ . By construction, it only has a poloidal and a toroidal component but no radial component, which are given in [Equation 6.1](#).

$$\begin{cases} B_\theta = \frac{1}{aR} \Psi_0 & \text{poloidal magnetic field} \\ B_\varphi = \frac{R_0}{R} B_0 & \text{toroidal magnetic field} \end{cases} \quad (6.1)$$

The magnetic field parameters are chosen such that the ratio of toroidal over poloidal magnetic field strength is  $aR_0 B_0 / \Psi_0 = 12$ . Tests have been performed on various mesh geometries in the scope of S3X from a perfectly regular grid with equally spaced cells in all coordinate directions to the distorted mesh depicted above. As the program can be either executed in a 2D or 3D mode with adapted stencils and geometry calculations, MMS tests have been developed for both scenarios.

### 6.1.2. Analytic solution

We are interested in the vorticity system on the electric potential  $\Phi$  and the parallel magnetic vector potential  $A_{\parallel}$ . We postulate that their analytic form is:

$$\Phi = \Phi_0 \left( 1 + 0.1 \cos(\theta) \cos\left(\frac{\varphi}{N_{div}}\right) \sin\left(2\pi \frac{\psi - \psi_{min}}{\psi_{max} - \psi_{min}}\right) \right) \quad (6.2)$$

$$A_{\parallel} = A_{\parallel,0} \left( 1 + 0.1 \cos(\theta) \cos\left(\frac{\varphi}{N_{div}}\right) \sin\left(2\pi \frac{\psi - \psi_{min}}{\psi_{max} - \psi_{min}}\right) \right) \quad (6.3)$$

A similar expression is chosen for the densities  $n_{i/e}$  and temperatures  $T_{i/e}$  that also contribute to the vorticity equation. The entire form of the test equation is:

$$\begin{cases} \partial_t \vec{\nabla} \cdot \left( \frac{m_i n_i}{B^2} \vec{\nabla}_{\perp} \Phi \right) + \vec{\nabla} \cdot \sigma_{\parallel} \left( \nabla_{\parallel} \Phi \vec{b} + \partial_t A_{\parallel} \right) &= \partial_t \Omega_{\pi} + \vec{\nabla} \cdot \sigma_{\parallel} \left( + \frac{T_e}{e} \nabla_{\parallel} \log(n_e) \vec{b} + \frac{1.71}{e} \nabla_{\parallel} T_e \vec{b} \right) - S_{\Phi}^{MMS} \\ \vec{\nabla} \cdot \left( \vec{\nabla}_{\perp} A_{\parallel} \vec{b} \right) - \mu_0 \sigma_{\parallel} \left( \nabla_{\parallel} \Phi + \partial_t A_{\parallel} \right) &= -\mu_0 \sigma_{\parallel} \left( \frac{T_e}{e} \nabla_{\parallel} \log(n_e) + \frac{1.71}{e} \nabla_{\parallel} T_e \right) - S_{A_{\parallel}}^{MMS} \\ \Omega_{\pi} = \vec{\nabla} \cdot \left( \frac{m_i}{Z_i B^2} \vec{\nabla}_{\perp} [nT] \right) & \end{cases} \quad (6.4)$$

The main difference to the original system of equations in [Equation 4.27](#) are the MMS source terms  $S_{\Phi}^{MMS}$  and  $S_{A_{\parallel}}^{MMS}$ . They contain the analytic evaluation of all other time-independant terms in the respective line of the equation. The derivatives on curvilinear coordinates can be calculated analytically with the metric theory discussed in [subsection 5.1.2](#). Boundary conditions are enforced by a penalty method on the boundary cell layer where the two quantities are set to their analytic expression. The MMS system is initialized with the analytic expressions for  $\Phi$  and  $A_{\parallel}$  in [Equation 6.3](#) and uniquely the vorticity equation is solved for one timestep. We are in a steady state, so the numerical solution after the first timestep should be equal to the initial state. One drawback of a steady state system is that time derivatives are always assumed to vanish and terms such as  $\Omega_{\pi}$ , the perpendicular Laplacian of  $\Phi$  or the divergence of  $A_{\parallel}$  are not confronted to their analytic form. To catch these terms, we add the vorticity  $\Omega$  to the MMS system and include it in the subsequent analysis. It is initialized with its analytic form:

$$\Omega = \Omega_{\pi} + \vec{\nabla} \cdot \left( \frac{m_i n_i}{B^2} \vec{\nabla}_{\perp} \Phi \right) + \vec{\nabla} \cdot \sigma_{\parallel} A_{\parallel}$$

and then calculated numerically after the first timestep. This allows to compare a numerical and an analytic form of the vorticity and hence all terms in [Equation 6.4](#).

### 6.1.3. Order of convergence

-  
-  
-  
Describe

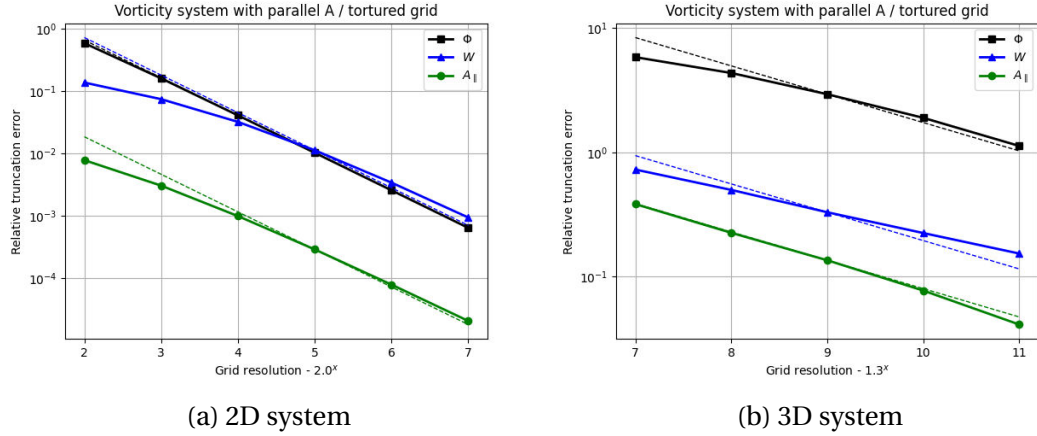


Figure 6.2.: Relative error between the initial plasma and the solution after one timestep. The  $x$ -axis indicates the number of points per zone in each direction, the total number of points is thus  $N_{tot}^{3D} = 8 \cdot X^3$  (resp.  $N_{tot}^{2D} = 4 \cdot X^2$ ). The dashed lines indicate the slope of the ideal 2nd order convergence

this beautiful graph

Thanks.

## 6.2. Linear Analysis

....

### 6.2.1. Pure advection

A first step to verify the correct physical behaviour of the simulation would be to investigate the plasma advection equations.

For this objective we set up a simplistic plasma model on a rectangular 2D SLAB topology. Periodic boundary conditions in all directions allow to properly observe wave propagation without any inference at the domain boundaries. In an isothermal hydrogen plasma without source terms and drifts, the governing equations then simplify to:

$$\partial_t n_i + \vec{\nabla} \cdot (n_i \vec{u}_i) = 0 \quad (6.5)$$

$$n_e = n_i \quad (6.6)$$

$$\partial_t (m_i n_i u_{\parallel}) + \vec{\nabla} \cdot (m_i n_i u_{\parallel} \vec{u}_i) = -2 T_e \vec{\nabla}_{\parallel} n_e \quad (6.7)$$

In this simple plasma, only the density and the velocity evolve over time and depend on each other. The electric potential  $\Phi$  can also be computed and observed, but it does not interfere with the system because the parallel electric field in the momentum balance [Equation 6.7](#) is calculated from the electron pressure gradient  $E_{\parallel} = (\vec{\nabla}_{\parallel} p_e + R_e)/n_e$ .

To perform the linear analysis of the system, we assume that field variables such as the velocity or density respect some Fourier solution as sum of several wave modes with respective amplitudes  $\tilde{X}_{\omega, k_{\perp}, k_{\parallel}}$ :

$$X = \bar{X} + \hat{X} = X_0 + \sum \tilde{X}_{\omega, k_{\perp}, k_{\parallel}} e^{i(-\omega t + k_{\perp} \psi + k_{\parallel} \theta)} \quad (6.8)$$

Electron and ion density are identical because of the quasi-neutrality assumption in [Equation 6.6](#). Since we do not consider any drifts the radial component  $u_{\psi}$  of the velocity vector vanishes. Further, the mean density is  $\bar{n} = n_0$  while the mean velocity  $\bar{u}_{\theta}$  is zero. Because we are only interested in a first order approximation of the solution, we neglect all higher-order mixed fluctuating terms. Thus, [Equation 6.5](#) and [Equation 6.7](#) transform to:

$$\begin{aligned} -i\omega \hat{n} + i\bar{n}k_{\parallel}\hat{u}_{\theta} + i\bar{u}_{\theta}k_{\parallel}\hat{n} &= 0 & \Leftrightarrow \hat{u}_{\theta} &= \frac{\omega}{n_0 k_{\parallel}} \hat{n} \\ -i\omega m_i (\bar{n}\hat{u}_{\theta} + \bar{u}_{\theta}\hat{n}) + i m_i k_{\parallel} (2\bar{n}\bar{u}_{\theta}\hat{u}_{\theta} + \bar{u}_{\theta}^2 \hat{n}) &= -2i T k_{\parallel} \hat{n} & \Leftrightarrow \hat{u}_{\theta} &= \frac{2T k_{\parallel}}{m_i n_0 \omega} \hat{n} \end{aligned}$$

Both are combined to obtain a dispersion relation for the frequency  $\omega$ :

$$\frac{\omega}{n_0 k_{\parallel}} = \frac{2T k_{\parallel}}{m_i n_0 \omega} \quad \Leftrightarrow \quad \omega = \pm \sqrt{\frac{2T}{m}} k_{\parallel} \quad (6.9)$$

It is apparent that both solutions for  $\omega$  are real therefore non-decaying waves travelling with the speed of sound  $c_s = \sqrt{2T/m}$  appear. The perpendicular wave mode does not contribute to the equation so a 1D system along the poloidal axis is sufficient to simulate the behaviour. Both the electron and the ion density are initialized with one sinusoidal perturbation and [Figure 6.3a](#) shows their evolution. The electron velocity in [Figure 6.3b](#) responds to this initial excitation with a shifted standing wave with same frequency.

## 6. Verification and Validation – 6.2. Linear Analysis

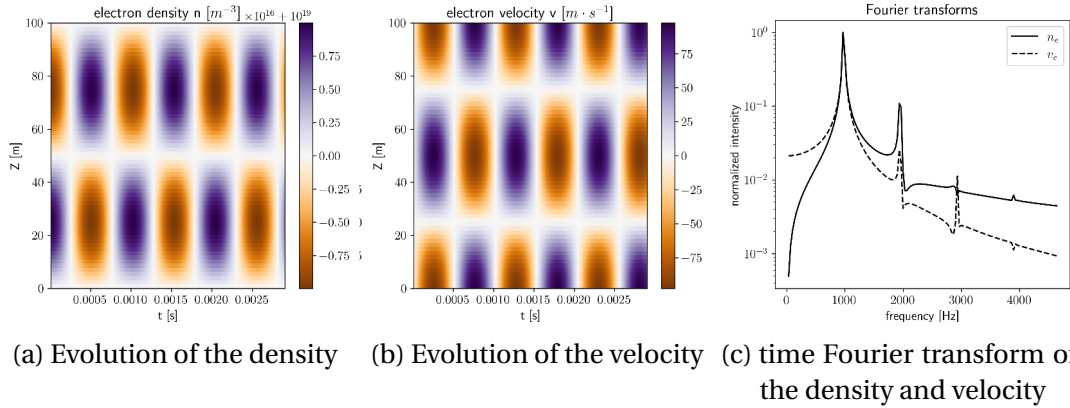


Figure 6.3.: Evolution of the 1D SLAB system with 64 cells in poloidal direction over 10000 timesteps with the RK4 scheme. For a better readability only parts of the graphs are represented

The system is initialized with one wavemode along the "poloidal" length of  $L = 100\text{m}$  so the wavenumber here is  $k_{\parallel} = 2\pi/L \approx 0.0628$ . The plasma temperature is kept constant at  $T = 100\text{eV}$  and the mass of a deuterium atom equals to  $m_i \approx 3.34 \cdot 10^{-27}\text{kg}$ , so we can expect a system frequency of  $\omega \approx 978\text{Hz}$  from the dispersion relation in [Equation 6.9](#). This corresponds precisely to the main frequency peak in [Figure 6.3c](#) and thus acoustic waves appear in the system as expected. The smaller peaks at higher frequency modes are however not physical and are likely due to numerical noise as their appearance highly depends on the spatial and temporal resolution and their intensity increases for longer simulations.

### 6.2.2. Electrostatic case

Before plunging into the vorticity equation with  $A_{\parallel}$  it may be interesting to discuss whether the correct behaviour is actually observed in the original electrostatic implementation. For that we reduce the system to the bare minimum set of equations that involve the electric potential  $\Phi$ . Neglecting all kind of transport equations and source phenomena remains the following simple equation on  $\Phi$ :

$$\partial_t \nabla \cdot \left[ \frac{m_i n_i}{B^2} \nabla_{\perp} \Phi \right] = -\nabla \cdot \sigma_{\parallel} \nabla_{\parallel} \Phi \quad (6.10)$$

whose simple dispersion relation reads, assuming that  $k_{\perp} \neq 0$ :

$$\omega = -\frac{B^2 \sigma_{\parallel}}{m_i n_i} \frac{k_{\parallel}^2}{k_{\perp}^2} i \quad \Rightarrow \quad \lambda = \frac{B^2 \sigma_{\parallel}}{m_i n_i} \frac{k_{\parallel}^2}{k_{\perp}^2} \quad (6.11)$$

As  $\omega$  is a pure negative complex number, we do not expect any oscillations but an exponential decay of the solution. All points in the domain decay with

$$\Phi(t) = \Phi_0 e^{-\lambda t} + C \quad (6.12)$$

where the decay rate  $\lambda$  is the negative imaginary part of  $\omega$  and  $\Phi_0$  relates to the initial distribution of the electric potential.

The time integration of this system can only be performed by solving the implicit system because there is no direct expression for the time derivative of  $\Phi$ . Further, the electric potential  $\Phi$  appears only in perpendicular and parallel Laplacian operators. Together with the periodic boundary conditions in all directions, one degree of freedom remains and the solution of  $\Phi$  can only be calculated up to a constant  $C$ . To make the system invertible, it is thus necessary to add some term to the system. One simple approach is to fix (or ground)  $\Phi$  to a set value  $\Phi^G$  at one point  $[i_\psi^G, i_\theta^G]$  in the domain. This defines the free parameter  $C$  and  $\Phi(t)$  at all points converges to  $\Phi^G$ .

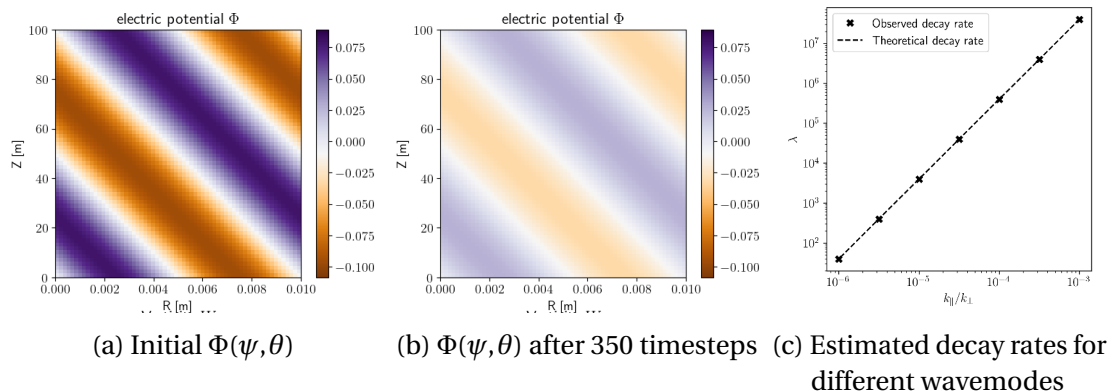


Figure 6.4.: Evolution of the 2D electrostatic SLAB system with 64 cells in radial and poloidal direction over 10000 timesteps with the implicit Euler scheme. The system is grounded at the center of the domain to  $\Phi^G = 0V$ .

The uniform decay can be clearly seen between Figure 6.4a and Figure 6.4b. It remains to investigate whether the observed attenuation matches the expected decay rate  $\lambda$ . A Fourier transformation as to determine oscillatory modes for the standing acoustic waves in the previous section is not of great help here, instead we use a non-linear least squares to fit the time evolution of  $\Phi(t)$  at an arbitrary point in the domain except the grounded point. We fit the parameters  $\Phi_0$ ,  $\lambda$  and  $C$  from Equation 6.12 to the simulation data and compare the hence estimated  $\lambda$  to the theoretical decay rate for the given initial wave. Figure 6.4c shows that there is a strong agreement between the theoretical and fitted decay rates for a large array of domain configurations. The wavenumbers  $k_{\parallel}$  and  $k_{\perp}$  were modified by changing the poloidal respectively the radial size of the domain with always the first wave mode spanning the entire domain. We can safely claim that the original electrostatic implementation produces the expected physical behaviour.

### 6.2.3. Electromagnetic case

While acoustic waves are characteristic for a physical medium, Alfvén waves dominate oscillations of ions within a magnetic field. The motion occurs in direction of the

magnetic field lines where the ion mass accounts for the inertia and the magnetic field tension for the restoring wave force. The Alfvén wave group velocity for a species  $i$  is given by:

$$v_A = \frac{B}{\sqrt{m_i n_i \mu_0}} \quad (6.13)$$

With the new parallel magnetic vector potential  $A_{\parallel}$  into the vorticity [Equation 4.27](#) Alfvén waves should appear in the simulation and the aim of this section is to prove their existence. We follow the same approach as in the previous section for the electrostatic case and reduce the system to the strict necessary minimum and keep following equations:

$$\partial_t \nabla \cdot \left[ \frac{m_i n_i}{B^2} \nabla_{\perp} \Phi \right] = \nabla \cdot \sigma_{\parallel} (-\nabla_{\parallel} \Phi - \partial_t A_{\parallel}) \quad (6.14)$$

$$\Delta_{\perp} A_{\parallel} = -\mu_0 \sigma_{\parallel} (-\nabla_{\parallel} \Phi - \partial_t A_{\parallel}) \quad (6.15)$$

We ignore any kind of advection phenomena thus all densities  $n_{i/e}$  and temperatures  $T_{i/e}$  keep their initial uniform distributions their gradients vanish. If we perform the linear analysis of the remaining system we get following relation for [Equation 6.14](#):

$$\begin{aligned} i \frac{m_i n_i}{B^2} k_{\perp}^2 \omega \hat{\Phi} &= \sigma_{\parallel} k_{\parallel}^2 \hat{\Phi} - \sigma_{\parallel} k_{\parallel} \omega \hat{A}_{\parallel} \\ \Leftrightarrow \qquad \qquad \qquad \hat{A}_{\parallel} &= \left( \frac{k_{\parallel}}{\omega} - i \frac{m_i n_i k_{\perp}^2}{\sigma_{\parallel} B^2 k_{\parallel}} \right) \hat{\Phi} \end{aligned}$$

and for [Equation 6.15](#):

$$\begin{aligned} -k_{\perp}^2 \hat{A}_{\parallel} &= i \mu_0 \sigma_{\parallel} k_{\parallel} \hat{\Phi} - i \mu_0 \sigma_{\parallel} \omega \hat{A}_{\parallel} \\ \Leftrightarrow \qquad \qquad \qquad \hat{A}_{\parallel} &= \frac{\mu_0 \sigma_{\parallel} k_{\parallel}}{\mu_0 \sigma_{\parallel} \omega + i k_{\perp}^2} \hat{\Phi} \end{aligned}$$

If we combine both expressions we can relate the frequency to the parallel and perpendicular wave modes:

$$\begin{aligned} \frac{k_{\parallel}}{\omega} - i \frac{m_i n_i k_{\perp}^2}{\sigma_{\parallel} B^2 k_{\parallel}} &= \frac{\mu_0 \sigma_{\parallel} k_{\parallel}}{\mu_0 \sigma_{\parallel} \omega + i k_{\perp}^2} \\ \Leftrightarrow \qquad \qquad \qquad i \frac{m_i n_i k_{\perp}^2 \omega}{\sigma_{\parallel} B^2 k_{\parallel}^2} &= 1 - \frac{\mu_0 \sigma_{\parallel} \omega}{\mu_0 \sigma_{\parallel} \omega + i k_{\perp}^2} \\ \Leftrightarrow \qquad \qquad \qquad \omega^2 + i \frac{k_{\perp}^2 \omega}{\mu_0 \sigma_{\parallel}} &= \frac{B^2}{m_i n_i \mu_0} k_{\parallel}^2 \end{aligned}$$

We find the square of the Alfvén group velocity [6.13](#) as a factor before the parallel wave number. There is an additional imaginary term in the dispersion relation which depends on the perpendicular wave number and adds some damping to the system.

## 6. Verification and Validation – 6.2. Linear Analysis

Let us call  $\gamma = 1/(\mu_0\sigma_{||})$  the associated damping coefficient. The dispersion relation can then be rewritten to:

$$\omega^2 + i\gamma k_\perp^2 \omega - v_A^2 k_{||}^2 = 0 \quad (6.16)$$

If we transform the system back to the time domain, we expect a damped solution for the potentials  $\Phi$  and  $A_{||}$  of the form [8]:

$$X = X_0 + \hat{X} e^{-\lambda t} e^{i(-\omega_0 t + k_\perp \psi + k_{||} \theta)} \quad (6.17)$$

where the decay rate  $\lambda$  contains the imaginary part and the oscillation frequency  $\omega_0$  the real part of  $\omega$ .

In the case that  $\gamma k_\perp^2 > 2v_A k_{||}$ , the frequency  $\omega$  is purely imaginary and the system decays to the mean value  $X_0$  with the rate:

$$\lambda = \frac{\gamma}{2} k_\perp^2 \pm \sqrt{\frac{\gamma^2}{4} k_\perp^4 - v_A^2 k_{||}^2} \quad (6.18)$$

If on the other hand  $\gamma k_\perp^2 < 2v_A k_{||}$ , the frequency  $\omega$  has both a real and an imaginary part. The decay rate is then:

$$\lambda = \frac{\gamma}{2} k_\perp^2 \quad (6.19)$$

and the system frequency:

$$\omega_0 = \pm \sqrt{v_A^2 k_{||}^2 - \frac{\gamma^2}{4} k_\perp^4} \quad (6.20)$$

In the case that the damping term is much smaller than the oscillatory term (if for instance the parallel wave mode dominates over the perpendicular one),  $\omega$  is a real number and the system frequency only depends on the Alfvén group velocity and we should be able to observe pure Alfvén waves.

$$\omega_0 = v_A k_{||}$$

In [Equation 6.18](#) and [Equation 6.20](#) we see that there are two possible solution for the decay rate respectively the oscillation frequency. This does not conflict with our assumed wave solution which has been defined in [Equation 6.8](#) as the sum of several Fourier modes and each solution here contributes to one mode.

As in the electrostatic case from the previous section, the just described system is not invertible and  $\Phi$  is defined up to a constant. Grounding the potential in one single point is however not a suitable solution here because it deteriorates the condition number of the vorticity matrix past solvability. Instead two other approaches will be followed to check if simulations can reproduce the expected physical behaviour.

### 6.2.3.1. Grounded line

One approach is to set the potential not in one but in several points to a fixed value. The potential in the remaining domain then distributes according to this value and the whole system becomes solvable. Numerically, this is achieved by replacing the row of the matrix corresponding to the grounded point by a single 1 on the diagonal and the matching term in the RHS vector by the desired value for  $\Phi$ . This operation is equal to enforcing Dirichlet boundary conditions in radial direction if  $\Phi$  is grounded at all points with index  $i_\psi^G$ .

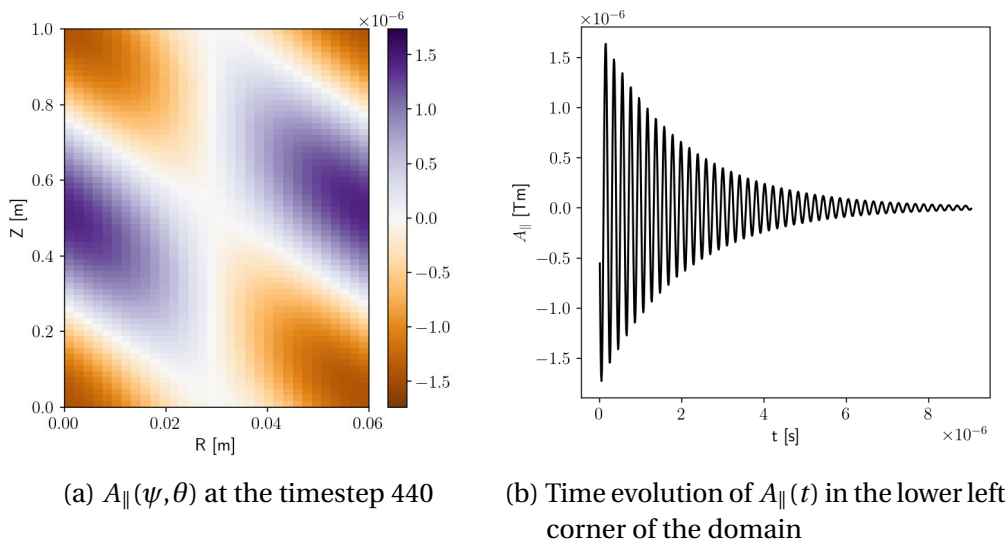


Figure 6.5.: Snapshot of an electromagnetic SLAB simulation on a domain with  $N_\psi = 32$  and  $N_\theta = 64$  grid points. All point at the radial center with  $i_\psi^G$  are grounded.

In the simulations with a grounded line, the initial wave solution has been applied to the vorticity field  $\Omega$  to prevent steep gradients and instabilities if it was done on  $\Phi$  directly. Very soon, the two potentials  $\Phi$  and  $A_{\parallel}$  respond to this initial excitation and a wave profile appears as depicted in Figure 6.5a. The line of grounded points in the middle of the domain however breaks the wave which then smoothly lines up with the equilibrium point  $\Phi_0 = 0V$  and  $A_{\parallel,0} = 0Tm$  around the grounded line. At this point it may be emphasized that only the electric potential  $\Phi$  is grounded, but as both potential fields are strongly coupled the grounded line affects  $A_{\parallel}$  equally. We thus have a wave that is guided between two poloidal grounded lines (remember that the domain is periodic in radial direction) so by construction the system cannot account for radial dynamics. If we consider a point that is furthest away from the grounded line (e.g. any point on the domain boundary in the example above) we might still be able to observe some expected physical behaviour. At first glance, if we track  $A_{\parallel}$  in one point over time as in Figure 6.5b, a decaying oscillation appears which is in line with the here dominant underdamped regime.

## 6. Verification and Validation – 6.2. Linear Analysis

First we investigate the underdamped scenario by opposing simulation results to the expected damping rates  $\lambda$  and frequencies  $\omega_0$ . As for the previous electromagnetic we fit the four free parameters in [Equation 6.17](#) to simulation data with a nonlinear least squares method. With 1000 sample points we get a high fitting fidelity with a relative standard deviation of the order of  $10^{-9}$  and the difference if the fit is performed on  $\Phi$  or  $A_{\parallel}$  has about the same magnitude.

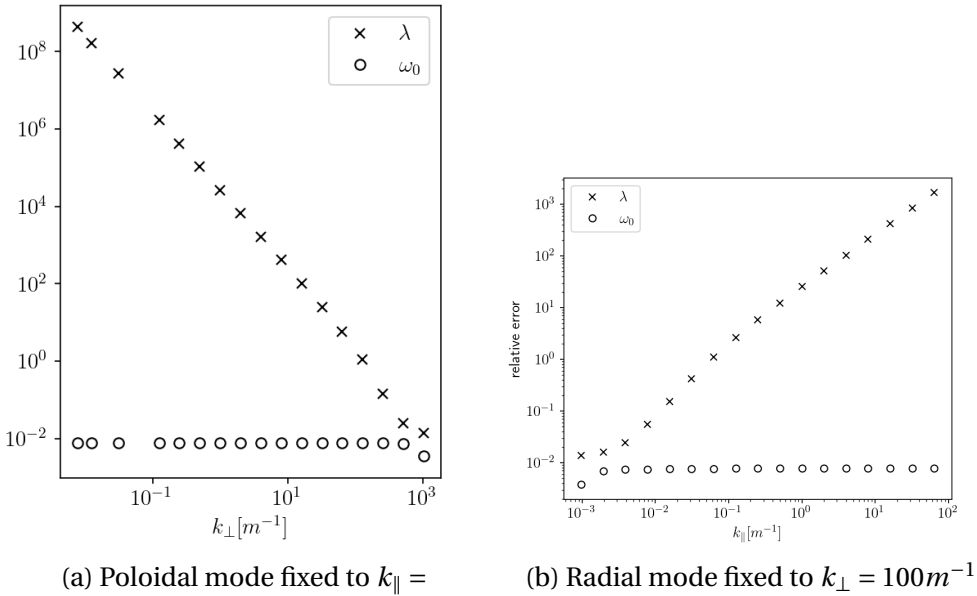


Figure 6.6.: Relative error for the fits of the frequency  $\omega_0$  and the decay rate  $\lambda$  on the evolution of  $A_{\parallel}$  with respect to the expected values in a grounded electromagnetic SLAB simulation on a domain with  $N_{\psi} = 32$  and  $N_{\theta} = 64$  grid points.

### 6.2.3.2. Diagonal perturbation

Another approach that

[Equation 6.14](#) on the potential is then replaced by:

$$\partial_t \nabla \cdot \left[ \frac{m_i n_i}{B^2} \nabla_{\perp} \Phi \right] + \varepsilon \Phi = \nabla \cdot \sigma_{\parallel} (-\nabla_{\parallel} \Phi - \partial_t A) + \varepsilon \Phi_e$$

This addition naturally affects the dispersion relation and we end up with:

$$\omega^2 + \left( i \gamma k_{\perp}^2 - \frac{B^2 \epsilon}{m_i n_i k_{\perp}^2} \right) \omega - v_A^2 k_{\parallel}^2 + \frac{v_A^2 \epsilon}{\sigma_{\parallel}} = 0$$

This eventually changes the previously calculated frequencies and damping rates.

## 6. Verification and Validation – 6.2. Linear Analysis

For the overdamped case, we get:

$$\lambda = \frac{\gamma}{2} k_{\perp}^2 - \frac{B^2 \epsilon}{2m_i n_i k_{\perp}^2} \pm \sqrt{\frac{\gamma^2}{4} k_{\perp}^4 - v_A^2 k_{\parallel}^2}$$

## **Part IV.**

# **Impact of Electromagnetic Effects on Plasma Simulations**

# 7. Electromagnetic simulations on analytic geometries

## 7.1. Slab configurations

### 7.1.1. Analysis of a plasma blob

The linear analysis from the previous section has only , as characteristic shear Alfvén and thermal electron times are much shorter than the ion cyclotronic time, which underlies the resolution of typical turbulent SOLEDGE3X simulations. Drift Alfvén waves in turn correspond to the impact of inductive electromagnetic effect on the formation of drift waves, where the term  $\partial_t A_\parallel$  in Ohm's law (Eq. ??) modifies the non-adiabatic response of the potential  $\Phi$  to parallel fluctuations of the electron pressure  $p_e$ . To study the these effects on a plasma blob in a slab domain.

We place ourselves in a plasma environment similar to the separatrix region in the diverted TCV simulations from the next Sec. ???. The magnetic field is aligned to the toroidal coordinate with  $B_{eq,t} = 1.3\text{T}$  with a curvature of 1.1m from the tokamak center, similar to the position of the separatrix at the outer mid-plane in TCV. Limiters are placed at both toroidal ends such that that connection length  $L_\varphi = 65\text{m}$ . A cartesian grid with coordinates  $r$  and  $z$  discretizes each poloidal plane, allowing radial fluxes out and with periodic boundary conditions in the vertical  $z$ -direction. The electron temperature is kept constant at  $T_e = 60\text{eV}$ , ions are cold and the background density is set to  $n_0 = 10^{19}\text{part/m}^3$ . To simplify the study and prevent numerical difficulties at the sheath, we apply Neumann-0 boundary  $\partial_\parallel n^{BC} = 0$  on the density and the potential  $\Phi$  is fixed to  $\Phi^{BC} = \Lambda T_e^{BC}$ . This is a major simplification to the typical SOLEDGE3X sheath conditions described in Sec. ???. The axisymmetric blob initially takes a Gaussian profile

$$n = n_0 \left(1 + \alpha e^{-[(r-r_b)^2 + (z-z_b)^2]/\delta_b}\right) \quad (7.1)$$

with a blob overdensity  $\alpha = 2$  and radius  $\delta_b = 1\text{cm}$ . The blob evolves with curvature and electric drifts, neglecting anomalous perpendicular diffusion and viscous effects. Further, electron inertia effect are neglected with  $m_e = 0$ . We compare the reference electrostatic case with magnetic induction in the parallel electric field and the full electromagnetic setting including flutter. The simulation results are collected in Fig. 7.1.

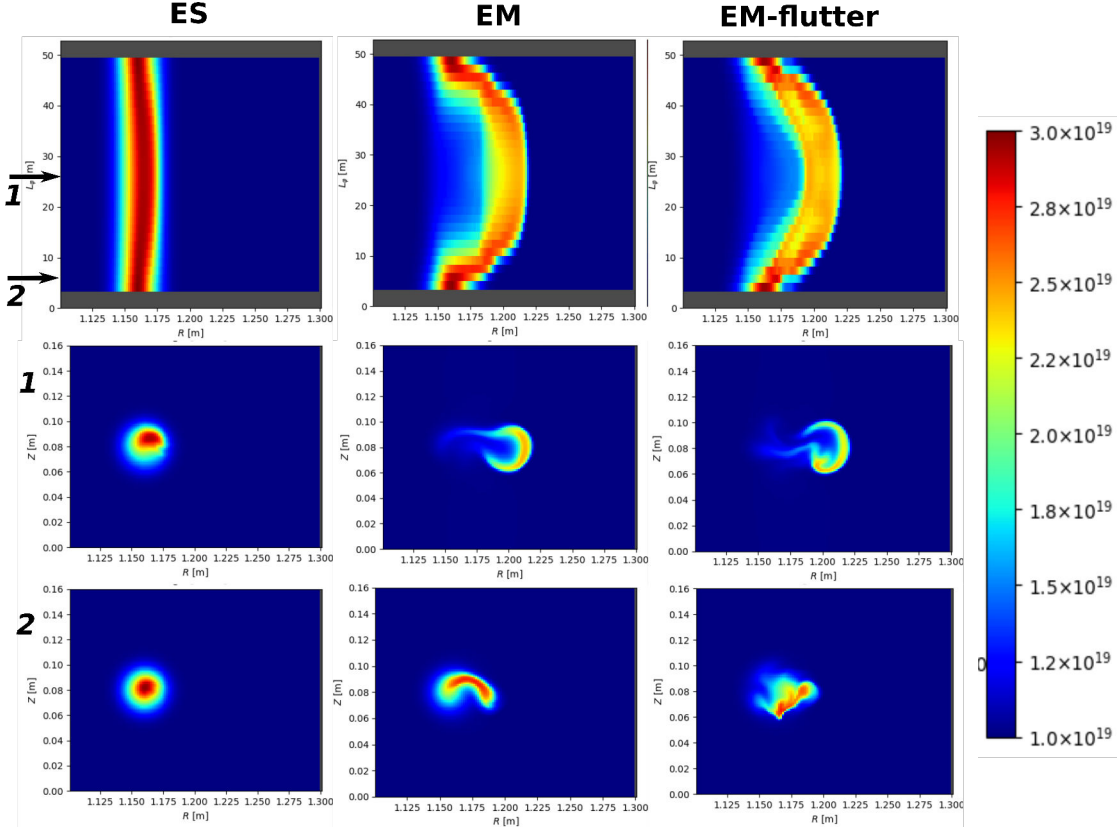


Figure 7.1.: Density profiles [ $\text{part}/\text{m}^3$ ] after  $9.6\mu\text{s}$  simulated plasma time for the electrostatic (ES), magnetic inductive (EM) and full electromagnetic scenarios (EM-flutter). The first row shows a view of the  $R - \varphi$  plane with the maximum density taken along the  $Z$  coordinate. The second and third rows show the density on poloidal planes ( $R - Z$ ) at the center of the field lines (1) and in proximity to the sheath (2).

In the center of the domain, drift waves determine the potential  $\Phi$  but it is dominated by the sheath in proximity to the limiters. Hence a parallel gradient appears on  $\Phi$ , which in turn induces a parallel current responsive to inductive electromagnetic effects. As a result, the blob filaments bends along the toroidal direction, with higher advection velocities in the center of the domain than at the sheath. The bending is much more pronounced for the two electromagnetic scenarios, in line with the findings of previous blob studies[39, 40, 63]. On closed field lines, the blob would conserve its axisymmetry and both  $j_{\parallel}$  and  $A_{\parallel}$  would remain 0 throughout the simulation.

### 7.1.2. Generation of drift waves

In the previous section, we examined how a single plasma blob propagates across open field lines. However, this does not account for how the blob appears in the first place. In this second part of the slab study, we investigate the onset of drift waves.

## 7. Electromagnetic simulations on analytic geometries – 7.1. Slab configurations

We consider the same setting as before but with a background density of  $n_0 = 2 \cdot 10^{19}$  part/m<sup>3</sup> and isothermal electrons and ions at  $T_e = T_i = 50$  eV. Instead of an initial overdensity, we apply a constant particle source of  $5 \cdot 10^{22}$  part/s on the core side, at all  $R < 1.12$  m. The emergence of drift-wave instabilities for the three scenarios is shown in Fig. 7.2.

Initially, the particle source causes the density to build up on the core side of the slab. The radial gradient becomes stronger and soon collapses into drift waves. These waves are particularly pronounced in the electrostatic and electromagnetic inductive models. The term  $\partial_t A_{\parallel}$  in Ohm's law intensifies the turbulent interchange, with plasma filaments reaching much further outward. On the other hand, the electromagnetic model with flutter has a stabilizing effect, producing only a thin turbulent layer at the exit of the source and maintaining a strong gradient at the transition from high-to low-density regions. As more particles are introduced at the source, the pressure differential causes this transition line to bend at scales of the simulation box, while the local gradient remains very steep.

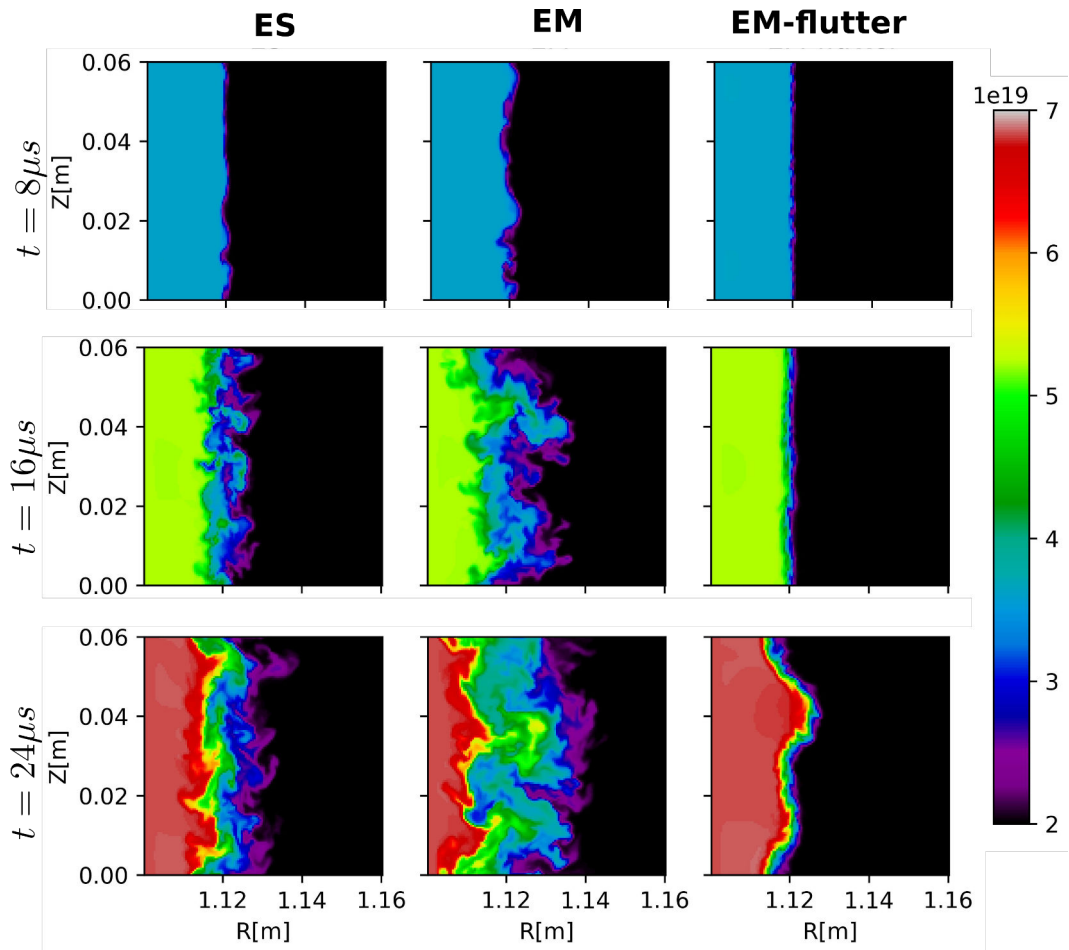


Figure 7.2.: Density profiles [part/m<sup>3</sup>] at the toroidal center of the slab, at about 32m from both limiters. The snapshots compare the electrostatic (ES), magnetic inductive (EM) and full electromagnetic scenarios (EM-flutter) scenarios after 8, 16 and 24 $\mu s$  simulated plasma time.

## 7.2. Circular geometry

# 8. Electromagnetic simulations on a realistic diverted geometry

To demonstrate the abilities of SOLEDGE3X to perform electromagnetic turbulence simulations of a realistic tokamak geometry, the configuration of the test cases has been inspired by the TCV-X21 benchmark [47]. This latter addresses L-mode discharges in TCV with a single lower X-point. The semi-implicit time discretization implemented in this model allows comparisons to be made between the electrostatic and electromagnetic models using the same code. Four cases have therefore been considered here: electrostatic (ES), electrostatic with electron inertia (ES-inert), electromagnetic (EM), and electromagnetic with flutter (EM-Flutter).

## 8.1. Simulation set-up

The plasma is pure deuterium, and only a quarter-torus with a relatively low resolution of approximately 1.9 million cells has been considered to speed up computations (see the mesh in a poloidal plane in Fig. 5.1a). A constant heat source of 25 kW is applied to both electrons and ions, equating to a full-torus equivalent total Ohmic heating of 200 kW. The external toroidal magnetic field is  $B_t = 0.95$  T, and the density at the separatrix is targeted to  $7 \cdot 10^{18}$  part/m<sup>3</sup>.

Since the aim of these preliminary computations was to focus on electromagnetic effects, neutrals have been omitted to speed up the convergence of the solutions. Simulations with a more complete physical model will be performed in a further work, including in particular the latest fluid neutral model [48] developed for regimes dominated by charge exchanges [31].

In all cases, the initial condition is the corresponding 2D transport solution obtained by increased perpendicular diffusion coefficients.

In Fig. 8.1, typical poloidal cuts of important plasma fields are shown. The local value of  $\beta$  varies between  $10^{-3}$  at the hot core boundary,  $10^{-4}$  around the separatrix and divertor region, and  $10^{-5}$  or lower in the far SOL. Consequently, the flutter perturbation  $\tilde{B}$  of the magnetic field remains small compared to the equilibrium field, barely exceeding 0.1% of  $B_t$  on the hot core side of the domain. The advection velocity associated with the flutter is also minimal, contributing to less than 0.1% of the cross-field

## 8. Electromagnetic simulations on a realistic diverted geometry – 8.1. Simulation set-up

transport, dominated by the electric "ExB" drift.

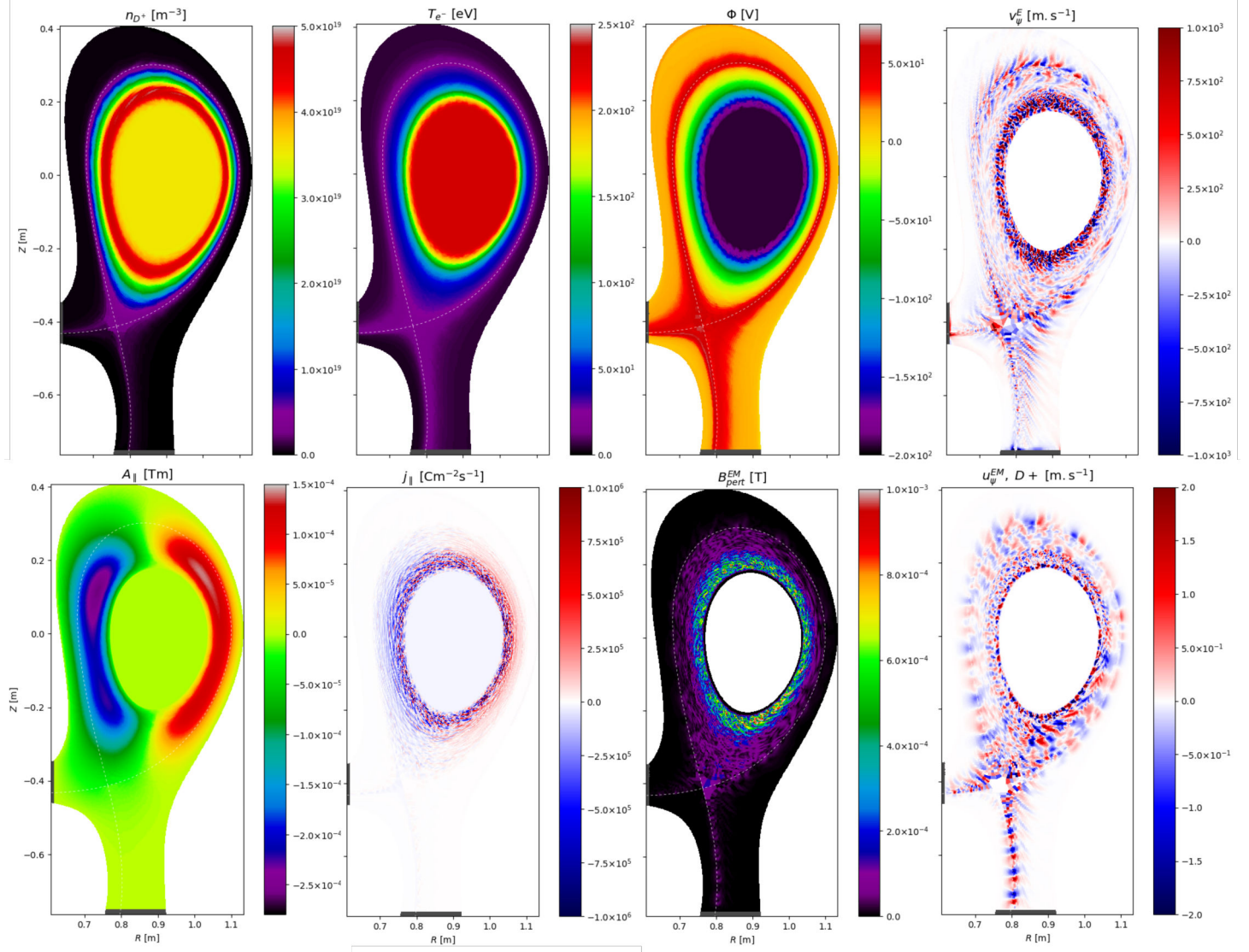


Figure 8.1.: Simulation snapshots of the full electromagnetic scenario with flutter. The first poloidal plane is shown after 6 ms simulated plasma time on the TCV case. From left to right, the first row shows the ion density  $n_i$ , the electron temperature  $T_e$ , the electric potential  $\Phi$ , and the radial "ExB" drift velocity  $v_E^\psi$ . The second row shows the parallel magnetic potential  $A_\parallel$ , the parallel current density  $j_\parallel$ , the amplitude of the flutter field  $\|\tilde{\mathbf{B}}\|$ , and the radial flutter advection velocity  $v_{\tilde{b}\psi}$ .

## 8.2. Comparison between the scenarios

We now compare the impact of the different levels of new physics on the TCV scenario. Since turbulent structures are essentially driven by the electric "ExB" drift, we consider the associated total kinetic energy  $E_{ExB} = \frac{1}{2} m_i \int_V n_i \|v_E\|^2 dV$  to estimate the turbulence level. As shown in Fig. 8.2a, a finite electron mass does not change the energy level with respect to the reference electrostatic scenario. Next, adding magnetic induction with  $A_\parallel$  further amplifies the turbulent interchange. This enhancement arises from the increased coupling between the magnetic and electric fields, leading to more instabilities and modified turbulent dynamics. Consequently, turbulent filaments give way to smaller, rounder blobs. Finally, the inclusion of flutter has a stabilizing effect on the turbulence, where fluctuations fall again to the level in the electrostatic case. Nonlinear effects in the parallel current equation, namely from the parallel pressure gradient  $\nabla_\parallel p_e$ , substantially impact the profiles of  $j_\parallel$  and hence the response of the potential  $\Phi$ . The direct consequence is a modification of the radial electric field and a modified evolution of "ExB" drifts. This does not contradict our previous observation that magnetic advection is negligible with respect to the electric drift.

With a different turbulence level, the heat exhaust is also affected, as shown in Fig. 8.2b. Without radiative effects, the quasi-totality of the heat leaves the tokamak at two divertor targets. The supplementary radial turbulent transport in the magnetic inductive scenario allows more hot particles to cross the separatrix from the core, which will then eventually reach the divertor. Overall, the heat flux is multiplied by a factor of 10. Electron inertia alone leads to an increase by a factor of 2, despite very similar turbulence levels. This phenomenon needs further investigation. Flutter does not reduce further the heat exhaust as one might expect because it is already very low in the electrostatic case.

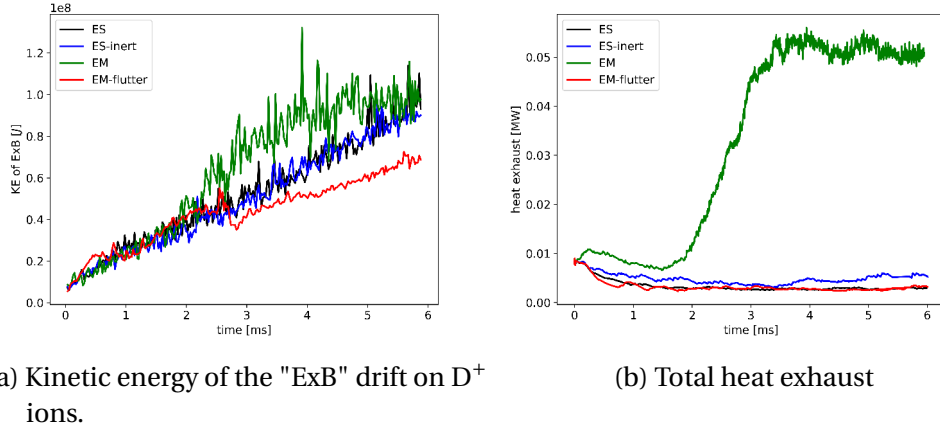


Figure 8.2.: Evolution of the kinetic energy and heat exhaust over time iterations on the turbulent TCV scenario. It indicates the turbulence level and its consequence on the total heat transport.

The change in turbulence intensity naturally impacts the mean profiles in Fig. 8.3. The most noticeable change affects the electromagnetic inductive scenario, where density and temperature gradients are considerably reduced by the additional radial turbulent transport. Again, the finite electron mass has no significant impact, and the reduced turbulence levels by flutter lead to steeper gradients. At this point, we stress the similarity to the simplified drift wave simulations on slab in Sec. 7.1.2, where the gradients from the dense core follow the same pattern.

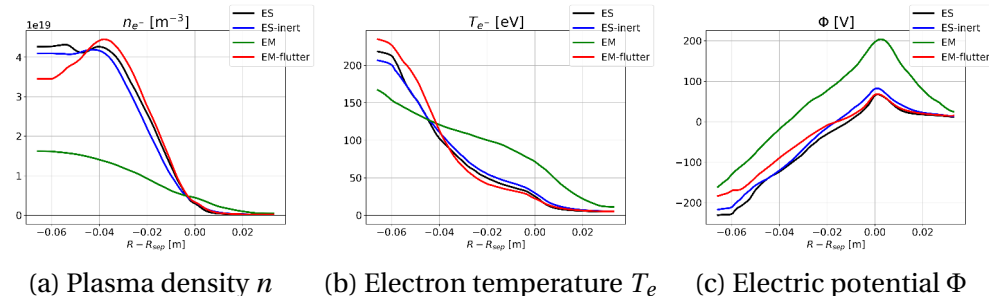


Figure 8.3.: Radial profiles at the outer mid-plane after 6 ms simulated plasma time. These profiles were obtained by averaging simulation data across all 32 toroidal planes and over the last 20 available plasma saves.

### 8.3. Numerical performances

In our previous work [4, 64] about the electrostatic model, it was pointed out that solving the implicit 3D vorticity operator is the most expensive and tricky operation in the algorithm. Adding new variables inevitably modifies the code's performance.

With the rather coarse mesh used in the present work, simulations have been run on 16 nodes with 48 CPUs each on the MARCONI supercomputer operated by CINECA [33]. Implicit systems, such as the 3D vorticity operator, have been inverted using the stabilized biconjugate gradient method (BCGS) [68] with the generalized algebraic multigrid preconditioner (GAMG) by PETSc [1].

The overall performance of the code largely depends on how quickly a certain plasma timespan can be calculated. Table 8.1 presents the average simulation time for one timestep, broken down by the cost of each implicit solver. For the vorticity system, we also provide the number of iterations the BCGS needed to match the imposed tolerance ( $10^{-8}$ ), as it relates to the condition number of the matrix. This system has always accounted for a considerable share of the total execution time and was heavily modified with the new electromagnetic model. Finally, the timestep size is provided, as a higher timestep size can compensate a costlier problem because the desired simulation time is reached in fewer iterations. As described earlier in Sec. ??, SOLEDGE3X uses a variable timestep scheme to maximize the CFL condition with the calculated fluxes.

	Total execution time per timestep [ms]	Execution time for the viscosity [ms]	Execution time for the heat diffusion [ms]	Execution time for the vorticity [ms]	N° of vorticity solver iterations	Timestep size [ns]
<b>ES</b>	664	61	76	339	80	15.6
<b>ES-inert</b>	523	61	77	193	32	16.4
<b>EM</b>	895	63	82	552	60	15.9
<b>EM-flutter</b>	2019	225	390	1147	55	16.6

Table 8.1.: Numerical metrics on the four TCV scenarios for one timestep. All quantities are averaged over the last 20000 timesteps of the simulation. The execution time refers to the wall-clock time and must be multiplied by the number of used processors (768) to get the actual used CPU time.

Introducing finite electron mass to the vorticity system significantly reduces the number of BCGS iterations and the overall solve time. This improvement occurs because electron inertia effects dominate Ohm's law, thereby reducing the anisotropy between the perpendicular and parallel Laplacians on  $\Phi$  in the electrostatic scenario. This reduction in anisotropy is due to the parallel diffusion coefficient being the conductivity  $\sigma_{\parallel}$  in the electrostatic case, but a finite electron mass  $m_e$  imposes an upper limit on it. Adding  $A_{\parallel}$  doubles the size of the matrix and introduces a more complex structure, challenging the solvers and requiring more iterations. Despite the higher complexity, a finite electron mass allows the solver to converge in fewer iterations than in the reference electrostatic case. However, the effective solve time is still worse due

to the doubling in system size. Finally, including flutter slightly improves the matrix condition compared to the scenario with only magnetic induction, but the execution time is significantly increased. At first glance, one would expect the solve time to correlate with the number of BCGS iterations as both electromagnetic scenarios solve a coupled 3D system on  $\Phi$  and  $A_{\parallel}$ . Since flutter introduces the radial direction to parallel gradients, and the coupling terms between the two unknowns are exactly a parallel gradient and a divergence (see Eq. 5.18), the matrix exhibits a decreased sparsity ratio. This circumstance is further aggravated by the fact that  $A_{\parallel}$  is not staggered in the radial direction, so the radial discrete gradient/divergence operator has a larger stencil width than its poloidal and toroidal counterparts.

The viscosity and heat diffusion solvers are not directly affected by the electromagnetic model, and their solve times are similar for the first three scenarios. Electromagnetic flutter, however, with its radial gradient (again), heavily modifies the parallel diffusion operators and requires solving one global 3D system instead of separate 2D systems on each flux surface (see Sec. 5.5.1). This is immediately reflected in the code performance, as both solvers take up to 5 times longer to solve.

In total, electron inertia decreases the computing time with an excellent improvement of the vorticity matrix condition. The magnetic inductive model means slightly higher computational costs, because the implicit vorticity problem doubles in size. Including electromagnetic flutter in the system almost quadruples the execution time compared to the original implementation because the radial parallel gradient complicates both the implicit vorticity and the parallel diffusion problem. The timestep size does not vary considerably between the scenarios and hence has only a limited impact on the overall performance.

## **Part V.**

# **Further Applications: Ripple Simulations**

# 9. Simulations of Magnetic ripple

Developments performed in the scope of this thesis can be useful for applications other than electromagnetic effects on plasmas. In transport mode with large perpendicular diffusion coefficients, a regime where drifts and turbulent scales are not solved, modulations of the magnetic field can have an external source. Because of the toroidal locality of toroidal field coils, the equilibrium magnetic field itself is not axisymmetric, a phenomenon usually referred to as "magnetic ripple". This chapter describes how the implementation of fluctuating magnetic fields in the framework of flutter can be used to simulate perturbations of the equilibrium magnetic field.

## 9.1. Motivation for simulating magnetic ripple

Power exhaust is a major concern in magnetic fusion research. Accurately predicting the heat load on the divertor plates is essential for the design and operation of current and future tokamaks. Estimates for the International Thermonuclear Experimental Reactor (ITER), the most powerful device currently under construction, indicate maximum local heat loads close to material limits[23]. For this reason it is important to study transport of heat and particle fluxes in present experiments, coupling the experimental analysis with a modelling effort with dedicated numerical tools.

Experiments conducted on the tungsten environment steady-state tokamak (WEST) at CEA in Cadarache, France[3], have demonstrated that the heat deposition on the divertor targets is not uniform in the toroidal direction. A "snake skin" pattern (see Figure 9.1), with alternating local maxima, appears on the inner and outer divertor targets. Reconstructions from infrared camera images exhibit a considerable difference between peaks and lows along a target line. These variations correlate with the disposition of the toroidal magnetic field coils, which locally modify the field lines and amplitude. This effect is known as magnetic ripple[65], and it is particularly pronounced on WEST, where the 18 coils cause strong variations in the amplitude of the magnetic field  $\mathbf{B}$ . For example, fast ions trapped in the toroidal magnetic field ripple have been found to be responsible for significant power losses[46]. Moreover, it is important to determine the impact of this toroidal modulation on impurity transport, in particular on tungstene contamination of the core[12].

SOLEDGE3X is a powerful fluid code for scrape-off-layer (SOL) and edge plasma analysis. The simulation domain extends from the far core across the separatrix up to the first wall in complex geometries. Its full model is capable of simulating resistive

## 9. Simulations of Magnetic ripple – 9.2. Generation of a non-axisymmetric magnetic configuration

drift-wave turbulence[5] with advanced fluid closures[6] and interactions with recycling neutrals[48]. A "transport" mode, where cross-field transport is approximated with effective diffusion coefficients, allows simulations to run until convergence on large machines like ITER[52] or JT-60SA[11]. Applications of this code include studies on impurity transport[7], heat exhaust[51], and detachment regimes in the divertor[70].

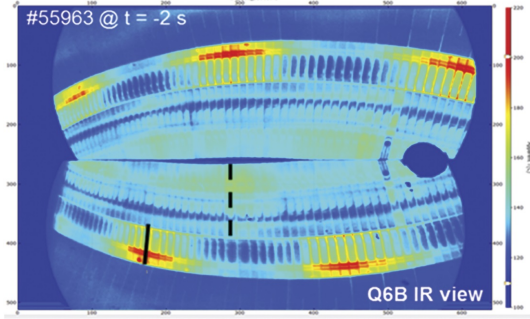


Figure 9.1.: Infrared camera view of the divertor target, taken from [3]. Red zones correspond to hot regions with high heat deposition. One can see the "snake skin" pattern, where the maximal intensity alternates between the inner and outer strike points.

In its current form, SOLEDGE3X can address 2D and 3D axisymmetric configurations as well as 3D non axisymmetric wall geometries[13], but still requires a 3D axisymmetric magnetic field. Therefore, toroidal variations of the magnetic field due to ripple could not be taken into account. Moreover, matching simulation results to experimental data is made difficult by the toroidal locality of Langmuir probes and their consequent susceptibility to ripple effects. Recent developments in the turbulence model have introduced electromagnetic effects[17], where magnetic field lines are perturbed by fluctuations of the magnetic vector potential. In this paper, we demonstrate that the new implementations can be used not only for plasma-induced perturbations but also for external perturbations of the axisymmetric magnetic field. This paves the way for ripple simulations in SOLEDGE3X and will be applied to a WEST scenario in this paper.

## 9.2. Generation of a non-axisymmetric magnetic configuration

The SOLEDGE3X framework is capable of addressing magnetic configurations with singularities at one or more X-points. Constructed by a combination of a toroidal field,  $\mathbf{B}_t$ , and a poloidal field,  $\mathbf{B}_{pol}$ , the expression for the magnetic field is:

$$\mathbf{B}_{axi} = \mathbf{B}_t + \mathbf{B}_{pol} = F \nabla \varphi + \nabla \Psi \times \nabla \varphi \quad (9.1)$$

## 9. Simulations of Magnetic ripple – 9.2. Generation of a non-axisymmetric magnetic configuration

where  $\varphi$  represents the toroidal angle. The toroidal field  $\mathbf{B}_t$  is derived from a toroidal flux  $F$  and  $\mathbf{B}_{pol}$  from a poloidal flux function  $\Psi$ . For high numerical accuracy, the meshing in SOLEGE3X is aligned to magnetic flux surfaces, treating singularities with a multi-domain decomposition shown in Figure 9.2

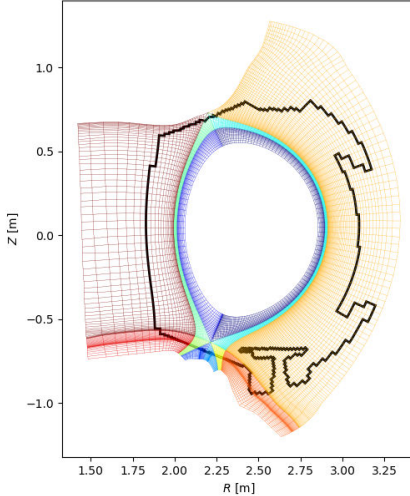


Figure 9.2.: Exemplary SOLEGE3X mesh for a WEST single-null geometry

On top of this axisymmetric basis, we calculate the ripple perturbation of the magnetic field induced by the toroidal distribution of the toroidal field coils. For that, we simplify each coil to a single, circular wire. We first discretize each of the  $N_c$  coils into  $N_{seg}$  segments. For every cell in the SOLEGE3X grid, we then calculate the magnetic field associated with the coils using the Biot-Savart law:

$$\mathbf{B}_{ripple} = \frac{\mu_0}{4\pi} I_c \sum_{i=1}^{N_c} \sum_{j=1}^{N_{seg}} \frac{\mathbf{d}_{i,j} \times (\mathbf{s}_{i,j+1} - \mathbf{s}_{i,j})}{\|\mathbf{d}_{i,j}\|^3} \quad (9.2)$$

where the coil current  $I_c$  corresponds to the nominal coil current times the number of wire turns in a coil,  $\mathbf{s}_{i,j}$  represents the start and end locations of each coil segment, and  $\mathbf{d}_{i,j}$  is the vector from each mesh point to the segment center. To avoid accounting for the axisymmetric component of the magnetic field twice, we define the perturbation field as the toroidal fluctuations of the ripple field:

$$\mathbf{B}_{pert} = \mathbf{B}_{ripple} - \langle \mathbf{B}_{ripple} \rangle_\varphi \quad (9.3)$$

Together with the axisymmetric part from Equation ??, the equilibrium magnetic field as applied to the simulation is given by:

$$\mathbf{B} = \mathbf{B}_{axi} + \mathbf{B}_{pert} \quad (9.4)$$

## 9. Simulations of Magnetic ripple – 9.2. Generation of a non-axisymmetric magnetic configuration

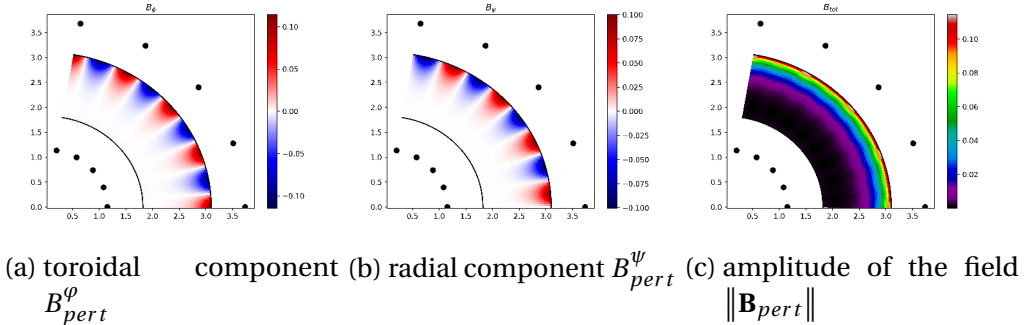


Figure 9.3.: Top views of the perturbed field  $\mathbf{B}_{\text{pert}}$  on the WEST tokamak at the mid plane. The black dots indicate the position of the toroidal field coils. The amplitude of the perturbed field remains much smaller than the axisymmetric component, whose amplitude ranges around 1T.

This strategy is now applied to compute the magnetic field ripple for the WEST tokamak, with the coil parameters described in Table 9.1. The ripple has a twofold impact on the magnetic equilibrium. A toroidal perturbation field, as shown in Figure 9.3a, modifies  $\mathbf{B}_t$  with local maxima located at the coils' positions and minima midway between two coils. Conversely, the radial perturbation in Figure 9.3b vanishes at the coils and midway, and modifies the poloidal field  $\mathbf{B}_{\text{pol}}$ .

Number of coils	$N_c$	18
Major coil radius	$R_c$	2.443 m
Minor coil radius	$a_c$	1.292 m
Nominal coil current	$I_c$	1.2 kA
Number of wire turns	$N_{\text{turns}}$	2028

Table 9.1.: Technical parameters of the toroidal field coils used to generate the ripple field for the WEST tokamak

Even if the amplitude of the ripple field is small compared to the axisymmetric one, it strongly impacts the poloidal field  $\mathbf{B}_{\text{pol}}$  from one poloidal plane to another. As  $\mathbf{B}_{\text{pol}}$  approaches zero at X-points, the radial perturbation  $\mathbf{B}_{\text{pert}}^{\psi}$  induced by the coils dominates over the axisymmetric component. In Figure 9.4, we observe that the X-point based on  $B_{\text{pol}}$  shifts by about 4.1 cm towards the high-field side at the maximal radial perturbation and by 2.7 cm inwards at the minimum.

## 9. Simulations of Magnetic ripple – 9.2. Generation of a non-axisymmetric magnetic configuration

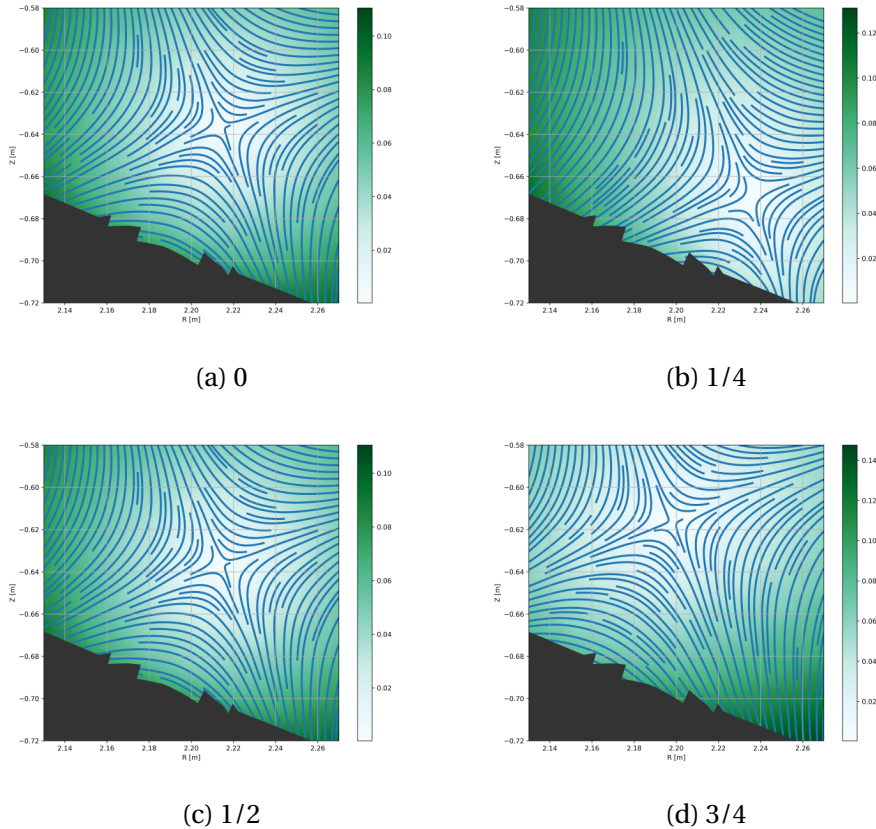


Figure 9.4.: Map of the poloidal field  $B_{pol}$  [T] at several poloidal planes within a ripple period around the lower X-point and the divertor targets. Streamlines are superposed to the fields to better visualize the position of the X-point and the separatrix at the divertor. The phase shifts 0 and  $1/2$  with respect to the coil positions are identical to the axisymmetric configuration as  $B_{pert}^\psi$  vanishes while the planes at  $1/4$  and  $3/4$  correspond to the respective maximum and minimum of  $B_{pert}^\psi$

However, this does not mean that the last closed flux surface (LCFS) experiences such a strong modulation. Indeed, the toroidal field  $\mathbf{B}_t$  imposes a strong self-similarity between poloidal planes. Tracing particles in the magnetic field, we observe in Figure 9.5 that particles seeded at the same position in different poloidal planes are only modulated by a few millimeters, and key features of the configuration, such as strike points or the X-point, remain almost unaffected.

## 9. Simulations of Magnetic ripple – 9.3. Application to a WEST scenario

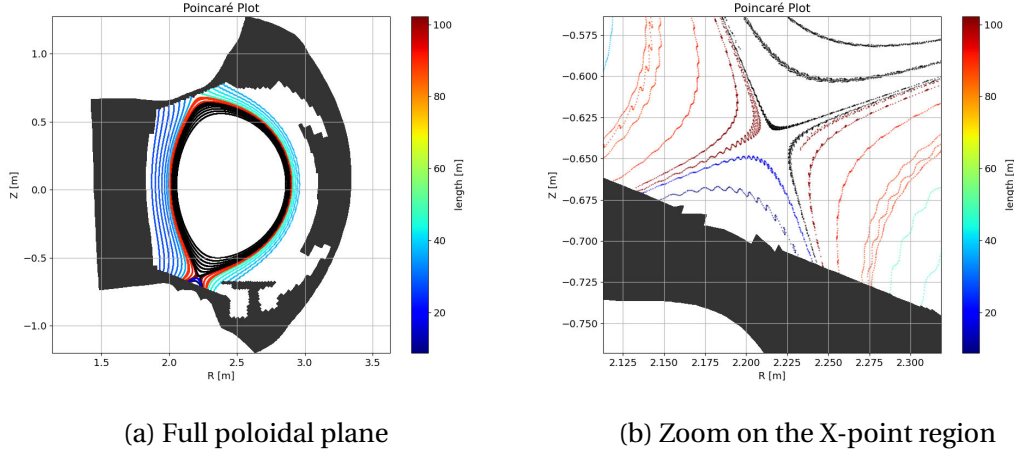


Figure 9.5.: Poincaré plot at coil-aligned poloidal planes. Seed points are uniformly distributed on the mid-plane along the radial and toroidal directions. Because of the periodicity of the perturbed field, each point corresponds to a field line crossing any of the  $N_c$  planes aligned with a coil. The total length of a field line from wall to wall translates in its color, black standing for an infinite closed field line.

### 9.3. Application to a WEST scenario

To demonstrate the newly implemented feature, we perform a SOLEDGE3X simulation on a WEST scenario with ripple. We consider a simple deuterium plasma with recycling fluid neutrals (recycling coefficient 98%). The core density fixed to  $2 \times 10^{19}$  particles/m<sup>3</sup>, and 1 MW Ohmic heating is equally applied to electrons and ions. Cross-field transport is emulated by a constant diffusion of 0.3 m<sup>2</sup>/s.

To reduce numerical costs, we only simulate one ripple period, or 1/18th of the full torus, and periodically expand the simulated plasma in the toroidal direction. The simulation contains 250,000 cells spread over 16 poloidal planes and was run on 384 processors of the MARCONI computing center[33] for 20 ms simulated plasma time. The plasma has not yet reached a converged state, but is sufficiently stable to observe ripple-induced phenomena.

## 9. Simulations of Magnetic ripple – 9.4. Conclusion

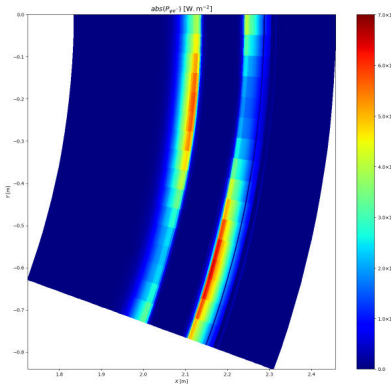


Figure 9.6.: Calculated electron wall heat flux in the divertor region from the SOLEDGE3X simulation. View on the target from the top for one ripple period.

In Figure 9.6, the heat fluxes originating at the core source reach the divertor target with maximal heat loads that alternate between the inner and the outer strike point with the toroidal coordinate. It has a strong resemblance with the "snake skin" pattern in Figure 9.1 observed on infrared imagery during the tokamak operation.

## 9.4. Conclusion

The incorporation of magnetic ripple perturbations into the SOLEDGE3X framework significantly enhances its capability to simulate complex magnetic configurations in tokamaks. Using the Biot-Savart law to calculate the ripple effects, this study exhibits the impact of the toroidal magnetic ripple on the magnetic equilibrium configuration in the WEST tokamak. These perturbations both affect the poloidal and the radial component of the axisymmetric magnetic equilibrium, with an important modulation of the poloidal field.

The perturbed magnetic field has been integrated into all parallel advection and gradient terms of the SOLEDGE3X transport model. The radial component of the poloidal perturbation field required major refactoring of the transport model because the mesh remains aligned to axisymmetric flux surfaces. Parallel fluxes now occur in all three directions in the curvilinear coordinates. Consequently, implicit solvers for the heat and viscosity problems are now applied to full-domain 3D systems instead of independent 2D systems on each flux surface, resulting in additional computational costs.

Simulations on a realistic WEST geometry demonstrate the new capability to perform simulations in a non-axisymmetric magnetic configuration. Key features of magnetic ripple, such as the modulation of heat loads on the divertor strike points along the toroidal coordinate, are successfully recovered.

## *9. Simulations of Magnetic ripple – 9.4. Conclusion*

With this new implementation, it will be possible to explore new physics, such as ripple effects on tungsten core contamination or improved predictions of power exhaust in tokamaks. Additionally, this enhancement allows for better comparisons between simulation and experimental data due to the toroidal locality of several plasma diagnostics.

# Conclusion

Lorem ipsum dolor sit amet, consectetuer adipiscing elit. Ut purus elit, vestibulum ut, placerat ac, adipiscing vitae, felis. Curabitur dictum gravida mauris. Nam arcu libero, nonummy eget, consectetuer id, vulputate a, magna. Donec vehicula augue eu neque. Pellentesque habitant morbi tristique senectus et netus et malesuada fames ac turpis egestas. Mauris ut leo. Cras viverra metus rhoncus sem. Nulla et lectus vestibulum urna fringilla ultrices. Phasellus eu tellus sit amet tortor gravida placerat. Integer sapien est, iaculis in, pretium quis, viverra ac, nunc. Praesent eget sem vel leo ultrices bibendum. Aenean faucibus. Morbi dolor nulla, malesuada eu, pulvinar at, mollis ac, nulla. Curabitur auctor semper nulla. Donec varius orci eget risus. Duis nibh mi, congue eu, accumsan eleifend, sagittis quis, diam. Duis eget orci sit amet orci dignissim rutrum.

Nam dui ligula, fringilla a, euismod sodales, sollicitudin vel, wisi. Morbi auctor lorem non justo. Nam lacus libero, pretium at, lobortis vitae, ultricies et, tellus. Donec aliquet, tortor sed accumsan bibendum, erat ligula aliquet magna, vitae ornare odio metus a mi. Morbi ac orci et nisl hendrerit mollis. Suspendisse ut massa. Cras nec ante. Pellentesque a nulla. Cum sociis natoque penatibus et magnis dis parturient montes, nascetur ridiculus mus. Aliquam tincidunt urna. Nulla ullamcorper vestibulum turpis. Pellentesque cursus luctus mauris.

# Bibliography

- [1] Satish Balay, Shirirang Abhyankar, Mark F. Adams, et al. *PETSc Web page*. <https://petsc.org/>. 2023. URL: <https://petsc.org/> (cit. on p. 101).
- [2] Charles K Birdsall. “Particle-in-cell charged-particle simulations, plus Monte Carlo collisions with neutral atoms, PIC-MCC”. In: *IEEE Transactions on plasma science* 19.2 (1991), pp. 65–85 (cit. on p. 33).
- [3] J. Bucalossi, J. Achard, O. Agullo, et al. “Operating a full tungsten actively cooled tokamak: overview of WEST first phase of operation”. In: *Nuclear Fusion* 62.4 (Feb. 2022), p. 042007. DOI: [10.1088/1741-4326/ac2525](https://doi.org/10.1088/1741-4326/ac2525). URL: <https://dx.doi.org/10.1088/1741-4326/ac2525> (cit. on pp. 104, 105).
- [4] H Bufferand, J Bucalossi, G Ciraolo, et al. “Progress in edge plasma turbulence modelling—hierarchy of models from 2D transport application to 3D fluid simulations in realistic tokamak geometry”. In: *Nuclear Fusion* 61.11 (2021), p. 116052 (cit. on pp. 68, 77, 100).
- [5] H. Bufferand, C. Baudoin, J. Bucalossi, et al. “Implementation of drift velocities and currents in SOLEDGE2D–EIRENE”. In: *Nuclear Materials and Energy* 12 (2017). Proceedings of the 22nd International Conference on Plasma Surface Interactions 2016, 22nd PSI, pp. 852–857. ISSN: 2352-1791. DOI: [10.1016/j.nme.2016.11.031](https://doi.org/10.1016/j.nme.2016.11.031). URL: <https://www.sciencedirect.com/science/article/pii/S2352179116301946> (cit. on p. 105).
- [6] Hugo Bufferand, J Balbin, S Baschetti, et al. “Implementation of multi-component Zhdanov closure in SOLEDGE3X”. In: *Plasma Physics and Controlled Fusion* 64.5 (2022), p. 055001 (cit. on p. 105).
- [7] G Ciraolo, S Di Genova, H Yang, et al. “Interpretative modeling of impurity transport and tungsten sources in WEST boundary plasma”. In: *Nuclear Fusion* 61.12 (2021), p. 126015 (cit. on p. 105).
- [8] L. Cohen. “Wave propagation with dispersion and damping”. In: *Proceedings of SPIE - The International Society for Optical Engineering* 5559 (Oct. 2004). DOI: [10.1117/12.564247](https://doi.org/10.1117/12.564247) (cit. on p. 88).
- [9] James William S Cook, RO Dendy, and Sandra C Chapman. “Particle-in-cell simulations of the magnetoacoustic cyclotron instability of fusion-born alpha-particles in tokamak plasmas”. In: *Plasma Physics and Controlled Fusion* 55.6 (2013), p. 065003 (cit. on p. 33).

## Bibliography

- [10] W. D. D'haeseleer, W. N. G. Hitchon, J. D. Shohet Callen, et al. *Flux Coordinates and Magnetic Field Structure*. Springer Series in Computational Physics, 1991. ISBN: 978-3-642-75595-8 (cit. on p. 65).
- [11] Ludovica De Gianni, Guido Ciraolo, Gerardo Giruzzi, et al. “Core and edge modeling of JT-60SA H-mode highly radiative scenarios using SOLEDGE3X-EIRENE and METIS codes”. In: *Frontiers in Physics* 12 (2024), p. 1422286 (cit. on p. 105).
- [12] S Di Genova, A Gallo, N Fedorczak, et al. “Modelling of tungsten contamination and screening in WEST plasma discharges”. In: *Nuclear Fusion* 61.10 (2021), p. 106019 (cit. on p. 104).
- [13] Stefano Di Genova. “Heavy ions migration in tokamak boundary plasmas : development of a numerical model to interpret WEST experiments”. PhD thesis. Aix-Marseille University, 2023 (cit. on p. 105).
- [14] G. Dif-Pradalier, V. Grandgirard, Y. Sarazin, et al. “Interplay between Gyrokinetic Turbulence, Flows, and Collisions: Perspectives on Transport and Poloidal Rotation”. In: *Phys. Rev. Lett.* 103 (6 Aug. 2009), p. 065002. DOI: [10.1103/PhysRevLett.103.065002](https://doi.org/10.1103/PhysRevLett.103.065002). URL: <https://link.aps.org/doi/10.1103/PhysRevLett.103.065002> (cit. on p. 39).
- [15] B. D. Dudson, S. L. Newton, J. T. Omotani, et al. “On Ohm's law in reduced plasma fluid models”. In: *Plasma Physics and Controlled Fusion* 63.12 (Oct. 2021). ISSN: 0741-3335. DOI: [10.1088/1361-6587/ac2af9](https://doi.org/10.1088/1361-6587/ac2af9). URL: <https://www.osti.gov/biblio/1840134> (cit. on pp. 45, 47).
- [16] B.D. Dudson, M.V. Umansky, X.Q. Xu, et al. “BOUT++: A framework for parallel plasma fluid simulations”. In: *Computer Physics Communications* 180.9 (2009), pp. 1467–1480. ISSN: 0010-4655. DOI: <https://doi.org/10.1016/j.cpc.2009.03.008>. URL: <https://www.sciencedirect.com/science/article/pii/S0010465509001040> (cit. on p. 39).
- [17] Raffael Düll, Hugo Bufferand, Eric Serre, et al. “Introducing electromagnetic effects in Soledge3X”. In: *Contributions to Plasma Physics* (2024), e202300147 (cit. on p. 105).
- [18] Thomas Eich, AW Leonard, RA Pitts, et al. “Scaling of the tokamak near the scrape-off layer H-mode power width and implications for ITER”. In: *Nuclear fusion* 53.9 (2013), p. 093031 (cit. on p. 31).
- [19] Richard Fitzpatrick. “A simple model of the resistive wall mode in tokamaks”. In: *Physics of Plasmas* 9.8 (2002), pp. 3459–3469 (cit. on p. 21).
- [20] HP Furth, PH Rutherford, and H Selberg. “Tearing mode in the cylindrical tokamak”. In: *The Physics of Fluids* 16.7 (1973), pp. 1054–1063 (cit. on p. 21).

## Bibliography

- [21] M. Giacomin, P. Ricci, A. Coroado, et al. “The GBS code for the self-consistent simulation of plasma turbulence and kinetic neutral dynamics in the tokamak boundary”. In: *Journal of Computational Physics* 463 (2022), p. 111294. ISSN: 0021-9991. DOI: [10.1016/j.jcp.2022.111294](https://doi.org/10.1016/j.jcp.2022.111294). URL: <https://www.sciencedirect.com/science/article/pii/S0021999122003564> (cit. on pp. 39, 57).
- [22] H. Grad and H. Rubin. *Hydromagnetic Equilibria and Force-Free Fields*. INIS-XU-021. United Nations (UN), 1958, pp. 190–197. URL: [http://inis.iaea.org/search/search.aspx?orig\\_q=RN:39082408](http://inis.iaea.org/search/search.aspx?orig_q=RN:39082408) (cit. on p. 22).
- [23] James P Gunn, S Carpentier-Chouchana, F Escourbiac, et al. “Surface heat loads on the ITER divertor vertical targets”. In: *Nuclear Fusion* 57.4 (2017), p. 046025 (cit. on pp. 31, 104).
- [24] S. Günter, Q. Yu, J. Krüger, et al. “Modelling of heat transport in magnetised plasmas using non-aligned coordinates”. In: *Journal of Computational Physics* 209.1 (2005), pp. 354–370. ISSN: 0021-9991. DOI: <https://doi.org/10.1016/j.jcp.2005.03.021>. URL: <https://www.sciencedirect.com/science/article/pii/S0021999105001373> (cit. on pp. 75, 79).
- [25] S. Günter, Q. Yu, J. H. Krüger, et al. “Modelling of heat transport in magnetised plasmas using non-aligned coordinates”. In: *Journal of Computational Physics* 209 (2005), pp. 354–370 (cit. on p. 72).
- [26] Robert Hager, S. Ku, A. Y. Sharma, et al. “Electromagnetic total-f algorithm for gyrokinetic particle-in-cell simulations of boundary plasma in XGC”. In: *Phys. Plasmas* 29.11 (2022), p. 112308. DOI: [10.1063/5.0097855](https://doi.org/10.1063/5.0097855). URL: <https://doi.org/10.1063/5.0097855> (cit. on p. 58).
- [27] Akira Hasegawa and Masahiro Wakatani. “Plasma edge turbulence”. In: *Physical Review Letters* 50.9 (1983), p. 682 (cit. on p. 44).
- [28] RJ Hastie, Jesus J Ramos, and Francesco Porcelli. “Drift ballooning instabilities in tokamak edge plasmas”. In: *Physics of Plasmas* 10.11 (2003), pp. 4405–4412 (cit. on p. 46).
- [29] RD Hazeltine, M Kotschenreuther, and PJ Morrison. “A four-field model for tokamak plasma dynamics”. In: *Physics of Fluids* 28.8 (1985), p. 2466 (cit. on p. 43).
- [30] P Hennequin, R Sabot, C Honoré, et al. “Scaling laws of density fluctuations at high-k on Tore Supra”. In: *Plasma Physics and Controlled Fusion* 46.12B (Nov. 2004), B121. DOI: [10.1088/0741-3335/46/12B/011](https://doi.org/10.1088/0741-3335/46/12B/011). URL: <https://dx.doi.org/10.1088/0741-3335/46/12B/011> (cit. on p. 39).
- [31] N. Horsten, G. Samaey, and M. Baelmans. “Development and assessment of 2D fluid neutral models that include atomic databases and a microscopic reflection model”. In: *Nuclear Fusion* 57.11 (Aug. 2017), p. 116043. DOI: [10.1088/1741-4326/aa8009](https://doi.org/10.1088/1741-4326/aa8009). URL: <https://dx.doi.org/10.1088/1741-4326/aa8009> (cit. on p. 97).

## Bibliography

- [32] IH Hutchinson, J Freidberg, et al. “Introduction to plasma physics”. In: *Electronic book available from: http://silas.psfc.mit.edu/introplasma/index.html* (2001) (cit. on p. 27).
- [33] F. Iannone, G. Bracco, C. Cavazzoni, et al. “MARCONI-FUSION: The new high-performance computing facility for European nuclear fusion modelling”. In: *Fusion Engineering and Design* 129 (2018), pp. 354–358. ISSN: 0920-3796. DOI: [10.1016/j.fusengdes.2017.11.004](https://doi.org/10.1016/j.fusengdes.2017.11.004). URL: <https://www.sciencedirect.com/science/article/pii/S0920379617309018> (cit. on pp. 101, 109).
- [34] I. Keramidas Charidakos, J. R. Myra, S. Parker, et al. “Analysis of equilibrium and turbulent fluxes across the separatrix in a gyrokinetic simulation”. In: *Physics of Plasmas* 25.7 (July 2018), p. 072306. ISSN: 1070-664X. DOI: [10.1063/1.5037723](https://doi.org/10.1063/1.5037723). eprint: [https://pubs.aip.org/aip/pop/article-pdf/doi/10.1063/1.5037723/14763677/072306\\_1\\_online.pdf](https://pubs.aip.org/aip/pop/article-pdf/doi/10.1063/1.5037723/14763677/072306_1_online.pdf). URL: <https://doi.org/10.1063/1.5037723> (cit. on p. 39).
- [35] Rinat Khaziev and Davide Curreli. “hPIC: A scalable electrostatic particle-in-cell for plasma–material interactions”. In: *Computer Physics Communications* 229 (2018), pp. 87–98 (cit. on p. 33).
- [36] M Kruskal and JL Tuck. “The instability of a pinched fluid with a longitudinal magnetic field”. In: *Proceedings of the Royal Society of London. Series A. Mathematical and Physical Sciences* 245.1241 (1958), pp. 222–237 (cit. on p. 21).
- [37] J D Lawson. “Some Criteria for a Power Producing Thermonuclear Reactor”. In: *Proceedings of the Physical Society. Section B* 70.1 (Jan. 1957), p. 6. DOI: [10.1088/0370-1301/70/1/303](https://doi.org/10.1088/0370-1301/70/1/303). URL: <https://dx.doi.org/10.1088/0370-1301/70/1/303> (cit. on p. 17).
- [38] Jarrod Leddy, Ben Dudson, Michele Romanelli, et al. “On the validity of drift-reduced fluid models for tokamak plasma simulation”. In: *Plasma Physics and Controlled Fusion* 57.12 (2015), p. 125016 (cit. on p. 46).
- [39] Wonjae Lee, J.R. Angus, Maxim V. Umansky, et al. “Electromagnetic effects on plasma blob-filament transport”. In: *Journal of Nuclear Materials* 463 (2015), pp. 765–768. ISSN: 0022-3115. DOI: [10.1016/j.jnucmat.2014.09.083](https://doi.org/10.1016/j.jnucmat.2014.09.083). URL: <https://www.sciencedirect.com/science/article/pii/S0022311514006837> (cit. on p. 94).
- [40] Wonjae Lee, Maxim V Umansky, JR Angus, et al. “Electromagnetic effects on dynamics of high-beta filamentary structures”. In: *Physics of Plasmas* 22.1 (2015) (cit. on p. 94).
- [41] A Lessig, C Caldin Queiros, E Franck, et al. “Fluid models for Tokamak Plasmas: Magneto-Hydrodynamic”. In: (2016) (cit. on p. 36).
- [42] A. Loarte, B. Lipschultz, A.S. Kukushkin, et al. “Chapter 4: Power and particle control”. In: *Nuclear Fusion* 47.6 (June 2007), S203. DOI: [10.1088/0029-5515/47/6/S04](https://doi.org/10.1088/0029-5515/47/6/S04). URL: <https://dx.doi.org/10.1088/0029-5515/47/6/S04> (cit. on p. 39).

## Bibliography

- [43] HF Meier, JJN Alves, and M Mori. "Comparison between staggered and collocated grids in the finite-volume method performance for single and multi-phase flows". In: *Computers & chemical engineering* 23.3 (1999), pp. 247–262 (cit. on p. 69).
- [44] AB Mikhailovskii and LI Rudakov. "The stability of a spatially inhomogeneous plasma in a magnetic field". In: *Soviet Physics JETP* 44 (1963), pp. 912–918 (cit. on p. 47).
- [45] AB Mikhailovskii and VS Tsypin. "Transport equations and gradient instabilities in a high pressure collisional plasma". In: *Plasma Physics* 13.9 (1971), p. 785 (cit. on p. 43).
- [46] D Moiraf, J Morales, L Colas, et al. "Optimization of the operational domain for ICRH scenarios in WEST from statistical analysis". In: *Nuclear Fusion* 63.8 (2023), p. 086010 (cit. on p. 104).
- [47] D.S. Oliveira, T. Body, D. Galassi, et al. "Validation of edge turbulence codes against the TCV-X21 diverted L-mode reference case". In: *Nuclear Fusion* 62.9 (July 2022), p. 096001. DOI: [10.1088/1741-4326/ac4cde](https://doi.org/10.1088/1741-4326/ac4cde). URL: <https://dx.doi.org/10.1088/1741-4326/ac4cde> (cit. on p. 97).
- [48] V. Quadri, P. Tamain, Y. Marandet, et al. "Self-organization of plasma edge turbulence in interaction with recycling neutrals". In: *Contributions to Plasma Physics* n/a.n/a (), e202300146. DOI: <https://doi.org/10.1002/ctpp.202300146>. eprint: <https://onlinelibrary.wiley.com/doi/pdf/10.1002/ctpp.202300146>. URL: <https://onlinelibrary.wiley.com/doi/abs/10.1002/ctpp.202300146> (cit. on pp. 97, 105).
- [49] Tariq Rafiq, Chris C Hegna, James D Callen, et al. "Unified theory of resistive and inertial ballooning modes in three-dimensional configurations". In: *Physics of Plasmas* 16.10 (2009) (cit. on p. 47).
- [50] K-U Riemann. "The Bohm criterion and sheath formation". In: *Journal of Physics D: Applied Physics* 24.4 (1991), p. 493 (cit. on p. 30).
- [51] Nicolas Rivals, Patrick Tamain, Yannick Marandet, et al. "Impact of enhanced far-SOL transport on first wall fluxes in ITER from full vessel edge-plasma simulations". In: *Nuclear Materials and Energy* 33 (2022), p. 101293 (cit. on p. 105).
- [52] Nicolas Rivals, Patrick Tamain, Yannick Marandet, et al. "SOLEDGE3X full vessel plasma simulations for computation of ITER first-wall fluxes". In: *Contributions to Plasma Physics* 62.5-6 (2022), e202100182 (cit. on p. 105).
- [53] P. J. Roache. "Code Verification by the Method of Manufactured Solutions ". In: *Journal of Fluids Engineering* 124.1 (Nov. 2001), pp. 4–10. ISSN: 0098-2202. DOI: [10.1115/1.1436090](https://doi.org/10.1115/1.1436090). URL: <https://doi.org/10.1115/1.1436090> (cit. on p. 80).
- [54] DD Ryutov, RH Cohen, TD Rognlien, et al. "The magnetic field structure of a snowflake divertor". In: *Physics of Plasmas* 15.9 (2008) (cit. on p. 25).

- [55] Frédéric Schwander, Eric Serre, Hugo Bufferand, et al. “Global fluid simulations of edge plasma turbulence in tokamaks: a review”. In: *Computers & Fluids* 270 (2024), p. 106141. ISSN: 0045-7930. DOI: <https://doi.org/10.1016/j.compfluid.2023.106141>. URL: <https://www.sciencedirect.com/science/article/pii/S0045793023003663> (cit. on pp. 39, 57).
- [56] Bruce D. Scott. “Three-dimensional computation of drift Alfvén turbulence”. In: *Plasma Phys. Control. Fusion* 39 (1997), p. 1635 (cit. on pp. 46, 47).
- [57] VD Shafranov. “Stability of plasmas confined by magnetic fields”. In: *Soviet Journal of Atomic Energy* 5 (1956), p. 38 (cit. on p. 21).
- [58] VD Shafranov. “On equilibrium magnetohydrodynamic configurations”. In: *Zh. Eksp. Teor. Fiz.* 33.3 (1957), pp. 710–722 (cit. on p. 22).
- [59] A.N. Simakov and P.J. Catto. “Drift-ordered fluid equations for field-aligned modes in low- beta collisional plasma with equilibrium pressure pedestals”. In: *Phys. of Plasma* 10.1 (2003), pp. 4744–57 (cit. on pp. 42, 43).
- [60] L. Spitzer and R. Härm. “Transport Phenomena in a Completely Ionized Gas”. In: *Phys. Rev.* 89 (5 Mar. 1953), pp. 977–981. DOI: [10.1103/PhysRev.89.977](https://doi.org/10.1103/PhysRev.89.977). URL: <https://link.aps.org/doi/10.1103/PhysRev.89.977> (cit. on p. 53).
- [61] P. C. Stangeby. *The Plasma Boundary of Magnetic Fusion Devices* (1st ed.) Boca Raton: CRC Press, 2000 (cit. on pp. 30, 58).
- [62] A. Stegmeir, A. Ross, T. Body, et al. “Global turbulence simulations of the tokamak edge region with GRILLIX”. In: *Phys. Plasmas* 26.5 (2019), p. 052517. DOI: [10.1063/1.5089864](https://doi.org/10.1063/1.5089864). URL: <https://doi.org/10.1063/1.5089864> (cit. on p. 39).
- [63] A. A. Stepanenko. “Impact of electromagnetic effects on macroscopic dynamics of blobs in hot low- $\beta$  edge plasma of fusion devices”. In: *Physics of Plasmas* 27.9 (Sept. 2020), p. 092301. DOI: [10.1063/5.0013435](https://doi.org/10.1063/5.0013435). URL: <https://doi.org/10.1063/5.0013435> (cit. on p. 94).
- [64] P. Tamain, H. Bufferand, G. Ciraolo, et al. “The TOKAM3X code for edge turbulence fluid simulations of tokamak plasmas in versatile magnetic geometries”. In: *Journal of Computational Physics* 321 (2016), pp. 606–623. ISSN: 0021-9991. DOI: [10.1016/j.jcp.2016.05.038](https://doi.org/10.1016/j.jcp.2016.05.038). URL: <https://www.sciencedirect.com/science/article/pii/S0021999116301838> (cit. on pp. 64, 68, 100).
- [65] Keiji Tani, Masafumi Azumi, Hiroshi Kishimoto, et al. “Effect of toroidal field ripple on fast ion behavior in a tokamak”. In: *Journal of the Physical Society of Japan* 50.5 (1981), pp. 1726–1737 (cit. on p. 104).
- [66] Asdex Team et al. “The H-mode of ASDEX”. In: *Nuclear Fusion* 29.11 (1989), p. 1959 (cit. on p. 30).
- [67] David Tskhakaya, Konstantin Matyash, Ralf Schneider, et al. “The Particle-In-Cell Method”. In: *Contributions to Plasma Physics* 47.8-9 (2007), pp. 563–594 (cit. on p. 32).

## Bibliography

- [68] H. A. van der Vorst. “Bi-CGSTAB: A Fast and Smoothly Converging Variant of Bi-CG for the Solution of Nonsymmetric Linear Systems”. In: *SIAM J. Sci. Stat. Comput.* 13.2 (1992), pp. 631–644. DOI: [10.1137/0913035](https://doi.org/10.1137/0913035) (cit. on p. 101).
- [69] Dong Wang and Steven J Ruuth. “Variable step-size implicit-explicit linear multistep methods for time-dependent partial differential equations”. In: *Journal of Computational Mathematics* (2008), pp. 838–855 (cit. on p. 75).
- [70] Hao Yang. “Control of detachment in the divertor region of tokamaks: impact of wall geometry, particle, and energy sources”. PhD thesis. Aix-Marseille University, 2023 (cit. on p. 105).
- [71] Kaiyu Zhang, Wladimir Zhlobenko, Andreas Stegmeir, et al. “Magnetic flutter effect on validated edge turbulence simulations”. In: *Nuclear Fusion* 64.3 (2024), p. 036016 (cit. on p. 58).

# Index

L

  Lorem ipsum, 4, 5

N

  Nam dui ligula, 6

# **APPENDICES**

# **A. New software modules**

In the course of the PhD, several software modules were created outside of SOLEDGE3X.

## **A.1. Grad-Shafranov solver**

Python script

## **A.2. Poincaré plots**

Python script

## **A.3. Generation of a modulated magnetic configuration**

Python script cite ERGOS here.

## **A.4. Toroidal plots in pySOLEDGE3X**

Python script

## **B. Intitulés des doctorats AMU**

- Discipline
  - Spécialité

### **ED 62 SCIENCES DE LA VIE ET DE LA SANTE**

- Biologie santé
  - Biochimie structurale
  - Génomique et Bioinformatique
  - Biologie du développement
  - Immunologie
  - Génétique
  - Microbiologie
  - Biologie végétale
  - Neurosciences
  - Oncologie
  - Maladies infectieuses
  - Pathologie vasculaire et nutrition
  - Ethique
  - Recherche clinique et Santé Publique
  - Biotechnologie

### **ED 67 SCIENCES JURIDIQUES ET POLITIQUES**

- Droit
  - Droit Privé
  - Droit Public
  - Histoire du Droit
- Science Politique

## **ED 184 MATHEMATIQUES ET INFORMATIQUE**

- Mathématiques
- Informatique
- Automatique

## **ED 250 SCIENCES CHIMIQUES DE MARSEILLE**

- Sciences Chimiques

## **ED 251 SCIENCES DE L'ENVIRONNEMENT**

- Sciences de l'Environnement
  - Anthropologie biologique
  - Ecologie
  - Géosciences
  - Génie des procédés
  - Océanographie
  - Chimie
  - Environnement et santé

## **ED 352 PHYSIQUE ET SCIENCES DE LA MATIERE**

- Physique et Sciences de la Matière
  - Astrophysique et Cosmologie
  - Biophysique
  - Energie, Rayonnement et Plasma
  - Instrumentation
  - Optique, Photonique et Traitement d'Image
  - Physique des Particules et Astroparticules
  - Physique Théorique et Mathématique
  - Matière Condensée et Nanosciences

## **ED 353 SCIENCES POUR L'INGENIEUR: MECANIQUE, PHYSIQUE, MICRO ET NANOELECTRONIQUE**

- Sciences pour l'Ingénieur
  - Energétique
  - Mécanique et physique des fluides
  - Acoustique
  - Mécanique des solides
  - Micro et Nanoélectronique
  - Génie civil et architecture
  - Nucléaire de fission
  - Fusion magnétique

## **ED 354 LANGUES, LETTRES ET ARTS**

- Etudes anglophones
- Etudes germaniques
- Etudes slaves
- Langues et littératures d'Asie
  - Chinois
  - Vietnamien
  - Coréen
- Arts
  - Arts plastiques
  - Sciences de l'art
  - Musique et musicologie
  - Etudes cinématographiques et audiovisuelles
  - Arts de la scène
  - Médiation culturelle des arts
- Pratique et théorie de la création artistique et littéraire
- Langue et Littératures françaises

*B. Intitulés des doctorats AMU –*

- Littérature générale et comparée
- Langues, littératures et civilisations romanes
  - Etudes hispaniques et latino-américaines
  - Etudes italiennes
  - Etudes roumaines

## **ED 355 ESPACES, CULTURES, SOCIETES**

- Géographie
- Démographie
- Urbanisme et Aménagement du territoire
- Préhistoire
- Archéologie
- Histoire de l'Art
- Histoire
- Sciences de l'Antiquité
- Mondes arabe, musulman et sémitique
- Etudes romanes
- Sociologie
- Anthropologie
- Architecture
- Cultures et Sociétés d'Asie

## **ED 356 COGNITION, LANGAGE, EDUCATION**

- Philosophie
- Psychologie
- Sciences du Langage
- Sciences de l'Information et de la Communication
- Sciences de l'Education
- Sciences Cognitives

*B. Intitulés des doctorats AMU –*

## **ED 372 SCIENCES ECONOMIQUES ET DE GESTION**

- Sciences de Gestion
- Sciences Economiques

## **ED 463 SCIENCES DU MOUVEMENT HUMAIN**

- Sciences du Mouvement Humain

## C. Consignes de présentation

Vous venez de télécharger la classe personnalisée LaTeX AMU pour les thèses de doctorat de l'université d'Aix-Marseille. Certains éléments doivent obligatoirement être utilisés:

The diagram shows the LaTeX AMU thesis title page template with various fields and their descriptions:

- Logo:** Aix-Marseille Université logo (Sociallement engagée) - Emplacement réservé exclusivement au logo de l'établissement en cotutelle, le cas échéant.
- Thesis Type:** THÈSE DE DOCTORAT
- Support Information:** Soutenue à Aix-Marseille Université dans le cadre d'une cotutelle avec le 10 janvier 2023 par
- Personal Information:** Prénom NOM, Titre de la thèse : sous-titre de la thèse
- Research Details:** Renseigner l'établissement en cotutelle, le cas échéant; Renseigner la discipline, la spécialité, le cas échéant, l'école doctorale, les partenaires de recherche.
- Jury Composition:** Composition du jury (multiple entries)

Prénom NOM Titre et affiliation	Rapporteur-e
Prénom NOM Titre et affiliation	Rapporteur-e
Prénom NOM Titre et affiliation	Examinateur-rice
Prénom NOM Titre et affiliation	Président-e du jury
Prénom NOM Titre et affiliation	Directeur-rice de thèse
Prénom NOM Titre et affiliation	Membre invité-e
- Partners:** Emplacements réservés aux logos des partenaires de recherche.
- Logos:** A, B, C, C
- Other Fields:** NNT : 2023AIXM0001

1. La page de titre des thèses AMU: elle est rédigée en langue française avec la police Titillium, disponible avec le modèle LaTeX AMU aux formats TTF et TFM, selon la charte graphique AMU.
2. En cas de cotutelle internationale, le logo de l'établissement partenaire doit apparaître en haut à droite de la page de titre;
3. La composition du jury, l'école doctorale, la discipline et la spécialité (le cas échéant) doivent être conformes au formulaire ADUM de demande de soutenance de thèse;
4. Le numéro national de thèse (NNT) doit être apposé sur la page de titre;

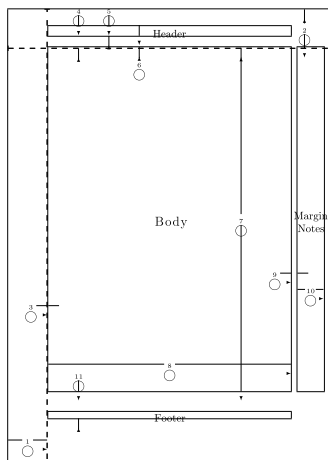
### C. Consignes de présentation

5. Le cas échéant, les logos d'institutions ou d'unité de recherche partenaires peuvent être ajoutés en bas de la page de titre;
6. La page **Affidavit**: selon la langue utilisée pour la rédaction de votre thèse, opter pour la version en français ou en anglais, puis la compléter, la dater et la signer;
7. La page **Liste de publications et participation aux conférences** réalisées au cours de votre projet de thèse ;
8. Les pages **Résumé et mots clés** en français et **Abstract and keywords** en anglais: chaque résumé ne doit pas dépasser 4000 caractères;

Selon vos besoins, vous pouvez ajouter les éléments suivants: sommaire et/ou table des matières, liste des figures, liste des tableaux, liste des acronymes, glossaire, index, nomenclature...

Pour le corps de votre thèse, si votre école doctorale ne vous donne pas de consignes plus précises, vous pouvez utiliser les styles établis dans ce modèle ou vos propres styles en suivant ces recommandations:

- Police neutre : Il est conseillé d'utiliser une police serif standard pour le texte et une police sans-serif standard pour les titres;
- Géométrie : paper=a4, fontsize=12pt, DIV=12;
- Interligne simple;
- Texte justifié.

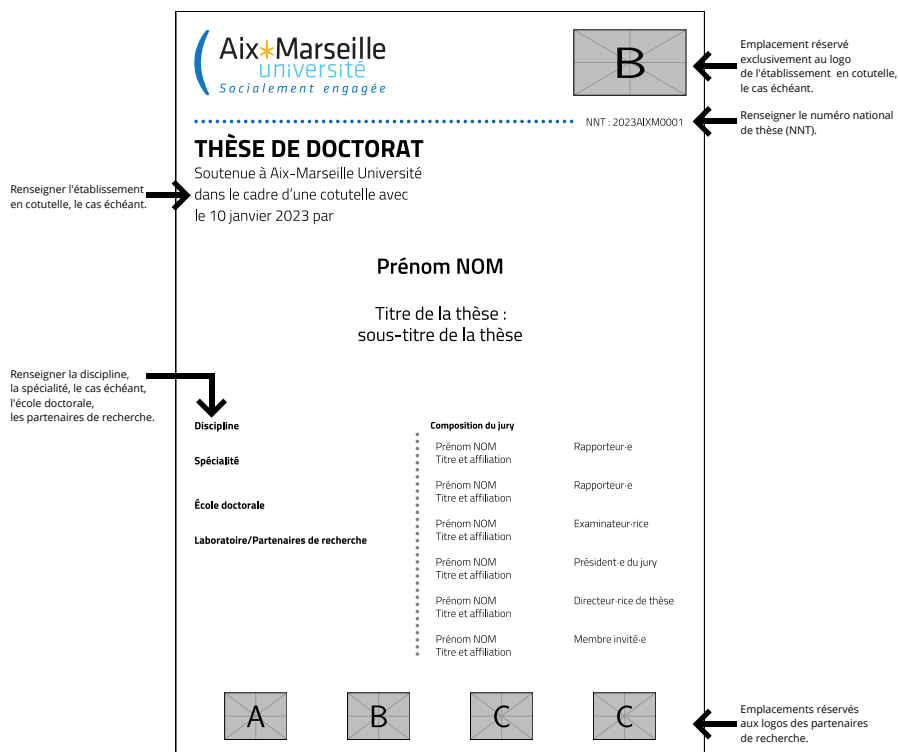


```
1 one inch + \hoffset  2 one inch + \voffset
3 \oddsidemargin = 2pt 4 \topmargin = -41pt
5 \headheight = 18pt   6 \headsep = 21pt
7 \textheight = 635pt   8 \textwidth = 448pt
9 \marginparsep = 12pt 10 \marginparwidth = 49pt
11 \footskip = 50pt    \marginparpush = 6pt (not shown)
\hoffset = 0pt          \voffset = 0pt
\paperwidth = 597pt     \paperheight = 845pt
```

Votre thèse devra être déposée en ligne en format PDF version 1.5 minimum sur [adum.fr](http://adum.fr).

## D. Presentation guidelines

You have downloaded the LaTeX AMU custom class for Aix-Marseille University doctoral theses. Some elements must be used:

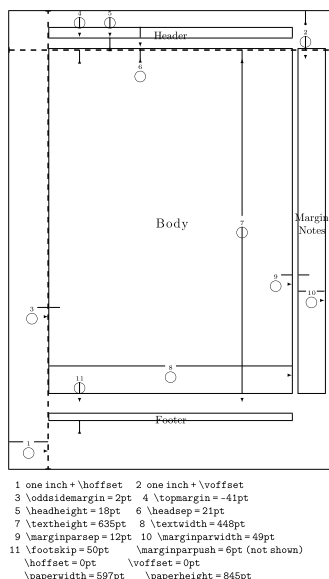


1. The title page of AMU's thesis: it is written in French with the Titillium font, provided with the LaTeX AMU template in TTF and TFM formats, according to AMU's graphic charter.
2. In the case of international cotutelle, the logo of the partner institution must appear at the top right of the title page;
3. The composition of the jury, the doctoral school, the discipline and the specialty (if applicable) must be in accordance with the ADUM application form for the thesis defense;
4. The national thesis number (NNT) must be displayed on the title page;

5. Where appropriate, logos of partner institutions or research units can be added to the bottom of the title page;
6. The **Affidavit** page: according to the language used for writing your thesis, choose the French or English version, then complete, date and sign it;
7. The **Liste de publications et participation aux conférences** page made during the course of your thesis project ;
8. **Résumé et mots clés** in French and **Abstract and keywords** in English pages: each summary must not exceed 4,000 characters.

Depending on your needs, you can add the following elements: summary and/or table of contents, list of figures, list of tables, list of acronyms, glossary, index, nomenclature... For the body of your thesis, if your doctoral school does not give you more specific instructions, you can use the styles established in this template or your own styles following these recommendations:

- Neutral font : It is recommended to use a standard serif font for text and a standard sans-serif font for titles;
- Geometry : paper=a4, fontsize=12pt, DIV=12;
- Single-line spacing;
- Justified text.



Your thesis must be submitted online in PDF 1.5 minimum version format on [adum.fr](http://adum.fr).